

Evidence for New Relations between Gamma Ray Burst Prompt and X-ray Afterglow Emission from 9 Years of *Swift*

Dirk Grupe^{1,2},

dgrupe007@gmail.com

John A. Nousek^{1,2}, Péter Veres², Bin-Bin Zhang^{2,3}, Neil Gehrels⁴

ABSTRACT

When a massive star explodes as a Gamma Ray Burst information about this explosion is retained in the properties of the prompt and afterglow emission. We report on new relationships between the prompt and X-ray afterglow emission of *Swift*-detected Gamma Ray Bursts found from BAT and XRT data between 2004 December and 2013 August (754 GRBs). These relations suggest that the prompt and afterglow emission are closely linked. In particular, we find very strong correlations between the BAT 15-150keV T_{90} and the break times before and after the plateau phase in the X-ray 0.3-10keV afterglow light curves. We also find a strong anti-correlation between the photon index of the GRB prompt emission and the X-ray spectral slope of the afterglow. Further, anti-correlations exist between the rest frame peak energy in the prompt emission, $E_{\text{peak,z}}$, and the X-ray afterglow decay slope during the plateau phase and the break times after the plateau phase. The rest-frame break times before and after the plateau phase are also anti-correlated with the rest-frame 15-150keV luminosity and isotropic energy during the prompt emission. A Principal Component Analysis suggests that GRB properties are primarily driven by the luminosity/energy release in the 15-150 keV band. Luminosity functions derived at various redshifts from logN-logS analysis, indicate that the density of bright bursts is significantly lower in the local Universe compared with the Universe at $z \approx 3$, where the density of bright GRBs peaks. Using cluster analysis, we find that the duration of *Swift* BAT-detected short-duration GRBs is less than 1s. We also present the catalogue of all *Swift*-onboard detected bursts.

Subject headings: GRBs: general

1. Introduction

The *Swift* mission (Gehrels et al. 2004) has revolutionized the study of Gamma-Ray Burst (GRB) afterglows. With *Swift* it was possible for the first time to access the earliest phase

of X-ray afterglows. In the pre-*Swift* era observations of the X-ray afterglow were limited to the 'normal' decay phase, typically starting roughly a day after detecting the burst. During the BATSE era only a relatively small number of bursts were actually followed up by X-ray observatories such as BeppoSAX (Costa et al. 1999; De Pasquale et al. 2006). All this changed when *Swift* was launched in November 2004. *Swift* is an autonomous robot making it possible to observe the X-ray afterglow starting typically 1 or 2 minutes after the trigger by the *Swift* Burst Alert telescope (BAT, Barthelmy 2005). Over almost 9 years in orbit (August 2013), *Swift* has discovered more than 800 GRBs, providing the largest sample of GRBs with prompt and after-

¹*Swift* Mission Operation Center, 2582 Gateway Dr., State College, PA 16801

²Department of Astronomy and Astrophysics, Pennsylvania State University, 525 Davey Lab, University Park, PA 16802

³Center for Space Plasma and Aeronautic Research (CSPAR), University of Alabama in Huntsville, Huntsville, AL 35899

⁴Astrophysics Science Division, Astroparticle Physics Laboratory, Code 661, NASA Goddard Space Flight Center, Greenbelt, MD 20771

glow emission observations. The prompt emission is likely the result of internal shocks produced in the newly formed jet (e.g. Mészáros 2006). Further models include photospheric emission including either baryon- (Pe’er et al. 2006; Beloborodov 2010) or magnetic field (Drenkhahn & Spruit 2002; McKinney & Uzdensky 2012) dominated ejecta. Additionally magnetic reconnection irrespective of the photospheric emission can be responsible for the prompt emission (Thompson 1994; Zhang & Yan 2011).

For the afterglow, the external shock scenario (Mészáros & Rees 1997) is observationally the most supported mechanism with modifications involving jet opening angle effects (Rhoads 1999), the nature of the interstellar medium (wind or constant density profile Panaitescu & Kumar (2000)) or possible late energy injection (Rees & Mészáros 1998).

As shown by Nousek et al. (2006) and Zhang et al. (2006), X-ray afterglows typically display a canonical light curve which is described by a very steep initial decay slope followed by a much shallower slope - usually referred to as the ‘plateau phase’. After this plateau phase we see the ‘normal’ decay phase. The initial decay slope in the X-ray light curve always regards as the tail of the prompt emission phase (Zhang et al. 2007; Zhang et al. 2009). The plateau phase marks the beginning of the afterglow phase which is generally caused by external shocks when the jet starts interacting with the interstellar medium. *Swift*’s ability to observe GRBs in soft X-rays within minutes after the explosion has lead to the discovery of flares in roughly 1/3 of all GRBs (e.g. Falcone et al. 2007; Margutti et al. 2011b). *Swift* not only revolutionized GRB studies, but the large number of bursts covered with multi-wavelengths observation and redshift measurements allows for the first time a very detailed statistical analysis of GRBs including cosmological studies of GRBs (e.g. Wanderman & Piran 2010)

Although a connection between the prompt and the afterglow emission of a GRB is expected according to the standard fireball model (e.g., Mészáros 2006), in the early days of *Swift* there was no evidence for such a connection (Willingale et al. 2007) except for the fluences in the prompt and afterglow emission. As shown by Gehrels et al. (2008) based on the observations

of the GRBs detected during the first two and half years of *Swift*, there is a strong correlation between the fluence in the 15-150 keV band and the flux density of the X-ray afterglow emission. O’Brien et al. (2006) showed that the *Swift* BAT and XRT light curves of the prompt and afterglow emission can be typically consistently connected. Recently Margutti et al. (2013) performed a statistical analysis of all *Swift*-detected GRBs until December 2010 and found clear correlations between the energetics of the prompt and the afterglow emission which also seem to suggest a universal scaling relation between short and long duration GRBs (Bernardini et al. 2012b; Nava et al. 2012). D’Avanzo et al. (2012) showed that X-ray afterglow luminosities at various times after the trigger correlate strongly with prompt emission properties, such as the isotropic energy E_{iso} and the peak energy in the high energy spectrum E_{peak} . Previously, statistical analysis of the X-ray afterglow light curves were also performed by Evans et al. (2009) and Racusin et al. (2009). While Evans et al. (2009) focused on the automated analysis of *Swift* XRT light curves and found that about 40% of *Swift* bursts with X-ray observations are GRBs with canonical light curves, Racusin et al. (2009) did an analysis of the spectral and temporal parameters of the *Swift* X-ray data. They found that different phases of the light curves are all consistent with closure relations that explain the various states of GRB afterglow light curves due to the jet geometry and physics, the environment around the GRB, and the election density and cooling (e.g. Zhang & Meszaros 2004, and references therein).

One of the best-known relations between GRB properties is the relation of the peak energy in the γ -ray spectrum E_{peak} with the isotropic energy E_{iso} or the collimation-corrected energy E_{γ} , the Amati and Ghirlanda relations, respectively (Amati et al. 2002; Ghirlanda et al. 2004). Similar to these are the relations found by Yonetoku et al. (2004) and Schaefer (2007) between E_{peak} and the burst luminosity.

Although various efforts have been made to link the energetic properties of the prompt and afterglow emission of GRBs (e.g., Margutti et al. 2013), what is still missing is to find correlations between prompt and afterglow properties, such as T_{90} , break times, or spectral slopes. While

this effort was hampered at the beginning of the *Swift* mission due to the small number of bursts (Willingale et al. 2007), with more than 800 bursts that *Swift* has detected in almost 9 years in orbit (August 2013), the GRB sample has grown allowing to find new relations among prompt and afterglow emission parameters.

One motivation for this study comes from the relation we found between redshift and excess absorption seen in the observed X-ray spectra of GRB afterglows (Grupe et al. 2007). However, this method is rather limited in the sense that it can only say if a burst has a large amount of excess absorption then it is a low-redshift burst. Our goal has been to find other means to distinguish between high and low redshift bursts more precisely and finally to estimate the redshift based on early available *Swift* data. Hydrogen column density derived from X-ray observations was found to correlate using canonical correlation analysis (Balázs & Veres 2011) with the properties of the prompt emission. The most sophisticated statistical analysis on *Swift* GRBs to date has been performed by Morgan et al. (2012) who applied a Random Forest algorithm in order to predict high redshift bursts. By looking through the data of *Swift*-detected GRBs we noticed several relations between prompt and afterglow properties which are not necessarily expected. In particular we noticed a strong relation of the BAT T_{90} and the 15-150 keV luminosity with the break times in the X-ray afterglow light curve (Grupe 2012).

Here we present a detailed analysis of the whole *Swift*-detected GRB dataset and will show that indeed there are many correlations that establish a tight relation between the prompt and afterglow emission in GRBs. This paper is organized as follows: In Section 2 we describe the sample selection and the data analysis, in Section 3 we show the distributions and correlation analysis of the *Swift*-detected GRBs prompt and afterglow properties, followed by a discussion in Section 4. Throughout the paper spectral indices β and light curve decay indices α are defined as $F_\nu(\nu) \propto \nu^{-\beta} t^{-\alpha}$. All errors are 1σ unless stated otherwise. Cosmological parameters like the luminosity distance or the comoving volume were derived from the cosmology calculator by Wright (2006). For all of these values we assumed the standard cosmology with $H_0=71 \text{ km s}^{-1} \text{ Mpc}^{-1}$, $\Omega_M=0.27$, and $\Omega_\Lambda=0.73$.

2. GRB Sample and Observations

2.1. Sample Selection

By the end of August 2013 *Swift* has discovered 804 bursts¹. Of these, 40 GRBs were discovered through ground processing and 9 burst through the *Swift* BAT slew survey. There is also one burst with no data available. Excluding these 50 bursts from the initial sample leaves a total of 754 *Swift*-discovered onboard triggered bursts. In Appendix A we present the whole catalog of these 754 GRBs as a machine readable file that is available online. This file contains the GRB name, *Swift* BAT trigger number, redshift, and BAT and XRT measured observed parameters. A full list of these parameters is given in Appendix A in Table 9.

Figure 1 displays the number of onboard detected GRBs per year (blue triangles). The red circles display the number of GRBs per year with spectroscopic redshift measurements. In 663 cases XRT observed the field of the GRBs and 607 X-ray afterglows were detected (91%) In 30 cases no X-ray afterglow was found although *Swift* was on the target with the XRT and UVOT within 300 seconds after the trigger. XRT did not observe the remaining 97 bursts due to observing constraints by the Sun, the Moon, or the Earth. The *Swift* UVOT detected a total of 251 GRB afterglows out of 655 UVOT observations performed. In this paper, however, we focus on the high energy properties of the bursts and leave the UVOT analysis for a later publication. Crucial to the analysis of physical parameters of GRBs are redshift measurements. Up to 2013 August, 232 GRBs out for the 754 GRBs in our sample or their host galaxies have spectroscopic redshift measurements (about 31%). Burst redshifts were taken from GCN circulars and the GRB redshift catalogues by Fynbo et al. (2009); Jakobsson et al. (2012) and Krühler et al. (2012). Note that in the pre-*Swift* era there were redshift measurements for only 43 bursts (Gehrels & Cannizzo 2012).

Of the 754 GRBs in our sample 63 are short duration and 689 are long duration GRBs (one early GRB did not had a T_{90} measurement) following the standard division at $T_{90}=2\text{s}$ as defined by Kouveliotou et al. (1993). This is a significantly

¹ A full interactive table of all *Swift* bursts can be found at: http://swift.gsfc.nasa.gov/docs/swift/archive/grb_table/.

lower percentage compared with the 25% found in the BATSE GRB sample. The reason is purely a selection effect due to the lower energy range of the *Swift* BAT compared with BATSE. As we will see later, the 2s deviation line is too long for *Swift* BAT-discovered bursts (see also Bromberg et al. 2013).

2.2. Observations and data reduction

The 0.3-10 keV X-ray count rate light curves and spectra were derived from the GRB repository website at the University of Leicester (Evans et al. 2007)². The light curves were fitted using multi-segment power law models (e.g. Evans et al. 2009) in which period of flares, in particular at early times after the explosion, were excluded from the analysis. In almost all cases (90-90%) we made use of the Leicester online light curve fitting routine which is used by the *Swift* team to make predictions on the XRT count rate of an X-ray afterglow. In the remaining cases we fitted the light curves in XSPEC manually. For these light curves we converted the light curve file into pha and an rmf that can be read into XSPEC by applying the FTOOL command *flu2xsp* to the light curve ASCII file.

For most spectra, we used the photon counting mode data (pc, Hill et al. 2004) that primarily cover the afterglow phase. We extracted source and background spectra and auxiliary response files provided by the GRB catalogue website at Leicester. These data typically cover the entire afterglow phase. The Windowed Timing mode data at the beginning of the light curves are often contaminated by emission from flares which tend to be much harder than the afterglow emission (Falcone et al. 2007; Margutti et al. 2011a,b). We did not rely on the automated fitting results on the GRB catalogue website in Leicester. In the majority of cases the automated routine uses a free fit ‘intrinsic’ absorber which results in excess absorption with large uncertainties even though the spectrum is consistent with just the Galactic absorption column density. Therefore all spectra were analyzed manually. In September 2007 the substrate voltage on the *Swift* XRT detector was increased from 0 to 6V (Godet et al., 2009). Accordingly, for all spectra we used the most current response

files. For spectra before August 2007 we used the response file *swxpc0to12s0_20070901v011.rmf* and after the end of August 2007 the response file *swxpc0to12s6_20010101v013.rmf*. All data were fit to absorbed power law models in XSPEC (Arnaud 1996). First we fit the data with the absorption parameter fixed to the Galactic value derived from the HI maps by Kalberla et al. (2005). If this model does not result in an acceptable fit, we thaw the absorption parameter to search for excess absorption above the Galactic value as described in Grupe et al. (2007). For afterglows with spectroscopic redshifts we determine the intrinsic absorption column density at the redshift of the GRB.

The parameters measured from the BAT data were derived from the BAT GRB analysis pages³ and BAT refined circulars and GCN burst reports. Whenever possible we also made use of the peak energy E_{peak} in the high energy spectrum of a burst given by primarily Konus-Wind (Aptekar et al. 1995) and the *Fermi* Gamma-Ray Burst Monitor (GBM; Meegan et al. 2009). Before the launch of *Fermi* (Atwood et al. 2009), we primarily used the E_{peak} measurements by Konus-Wind and the Suzaku WAM published in GCN Circulars. After the *Fermi* launch, we used the *Fermi* GBM measurements when available, which now exist for roughly 50% of all bursts after the *Fermi* launch.

In the end we derive T_{90} , the 15-150 keV photon spectral slope Γ , and the 15-150 keV fluence from the BAT, and the 0.3-10 keV X-ray spectral slope β_X , the break times at the beginning and the end of the plateau phase T_{break1} and T_{break2} , the slope during the plateau phase α_{X2} and the ‘normal’ decay slope α_{X3} . For bursts with spectroscopic redshift measurements the fluence was k-corrected (e.g. Humason et al. 1956; Oke & Sandage 1968) and T_{90} , T_{break1} , and T_{break2} were transferred into the rest frame. The rest-frame 15-150 keV luminosity is the mean isotropic luminosity during the time $T_{90,z} = T_{90}/(1+z)$ determined from the k-corrected fluence. A complete description of each parameter is given in Appendix B.

³<http://swift.gsfc.nasa.gov/docs/swift/results/BATbursts/>

²http://www.swift.ac.uk/xrt_curves/

3. Results

One of the goals of this paper is to establish new connections between GRB prompt and afterglow emission properties. Therefore we need to examine the dataset by means of statistics. In this section we will first present the distributions of the observed and rest-frame parameters of *Swift*-detected GRBs. In particular we will look at differences between short and long-duration GRBs. We will then look at bi-variate correlations among these parameters with the goal of finding evidence for connections between GRB prompt and afterglow phases. This is then followed by a principal component analysis in order to search for underlying properties that drive the observed parameters in GRBs. The section closes with a discussion of the GRB luminosity functions and looking into estimating the redshift of a burst including an update on the redshift - excess absorption relation (Grupe et al. 2007).

3.1. Distributions

The mean, standard deviation and median of all *Swift*-discovered GRBs, as well as for long and short-duration GRBs, and high redshift GRB ($z > 4.0$) are listed in Table 1. We included high-redshift bursts to this table in order to examine if these bursts appear to be somewhat special and have different properties than bursts at lower redshifts or bursts without redshift measurements. In this section we show the distributions of T_{90} , the break times in the X-ray light curves, decay slopes, and redshifts. All other distributions are shown in Appendix C. In Figures 2 through 6 the statistical analysis of the property distributions are visualized through three standard tools in data mining (e.g. Feigelson & Babu 2012; Torgo 2011; Crawley 2007):

- Histogram and kernel density estimator
- Box plot
- q-q plot

We explain the purpose of these statistical tools in Appendix C.

Figures 2 and 3 display the distributions of the BAT T_{90} and the break times T_{break1} and T_{break2} before and after the plateau phase in the

X-ray light curve. The observed times are displayed in Figure 2 and the plots in Figure 3 show the values shifted into the rest-frame. The median T_{90} value for all *Swift*-discovered GRBs is 38s and for long GRBs only, 46s. The density estimate of the T_{90} distribution suggests that for *Swift*-detected GRBs we see a bimodal distribution, separating the bursts into short and long bursts, as had been suggested based on the BATSE results (Kouveliotou et al. 1993). The division between the two groups, however, appears to be at a shorter T_{90} than with the BASTE detected bursts, in agreement with the results by Bromberg et al. (2013): the observed T_{90} distribution suggests that the division line between short and long bursts detected by BAT is on the order of 1s. These short bursts also appear clearly as outliers in the T_{90} box diagram for all GRBs. In the rest-frame (as shown in Figure 3) the median T_{90} of all bursts (with redshifts) is 13.4s, 16.0s for long, and 0.27s for short bursts.

Although break times before the plateau phase of short and long bursts are all of the order of roughly 500s, there are significant differences in the break times after the plateau phase. While long GRBs show breaks after the plateau phase in the observed frame at about 8400s after the trigger, short GRBs show a median break time after the plateau of 300s. In the rest frame the break times are 150s and 3360s for the long bursts. These break times before and after the plateau phase are comparable to the values published by Evans et al. (2009) and Margutti et al. (2013). It is interesting to note that from the relation between redshift and the length of the plateau phase as reported by Stratta et al. (2009) one would naively expect short GRBs to have longer plateau phases than long GRBs as they occur (as we will show later) at lower redshifts. Note, however, that for the short bursts we do not have enough bursts with redshift and break time measurements that will allow to state reliable numbers.

Figure 4 displays distributions of the X-ray light curve decay slopes during and after the plateau phase α_{X2} and α_{X3} (upper and lower panels, respectively). The distribution of decay slope during the plateau phase α_{X2} is almost Gaussian with an extended wing towards the very flat end of the distribution (see the Q-Q plot in Figure 4) Note, although this phase is commonly called the ‘plateau

phase’, the median decay slope of all bursts is of the order of $\alpha_{X2}=0.6$ and that there is a large scatter in the distribution of decay slopes ($\sigma=0.44$). Some plateau decay slopes can be relatively steep with $\alpha_{X2}>1.0$. Our mean and median values of α_{X2} are slightly steeper than what has been found by Evans et al. (2009) and Margutti et al. (2013), 0.27 and 0.32, respectively. One reason why we found a slightly steeper decay slope during the plateau phase can be that we accept even slopes with $\alpha_{X2}>1.2$ (see Figure 4) which is not the case in the Margutti et al. (e.g. 2013) sample.

The distribution of the ‘normal’ decay slopes after the plateau is shown in the lower panel of Figure 4. Note again that the distribution of α_{X3} is quite broad and a significant number of bursts have decay slopes that exceed $\alpha_{X3}>2.0$ which is typically assumed to be a decay slope after a jet break, particularly for short-duration GRBs. The mean and standard deviation of all GRBs of α_{X3} is 1.55 and 0.73 and the median value is 1.38, suggesting a non-Gaussian distribution. The median decay slope during the ‘normal’ decay phase for long GRBs is 1.37. Note that there are three outliers in the α_{X3} distribution, which are all short GRBs (GRBs 051210, 120305A, and 120521A). All these decay slopes are extreme of the order of 7 or 8. With the median values as discussed above and listed in Table 1 we can construct a median GRB X-ray afterglow light curve. Figure 5 displays the observed median 0.3-10 keV X-ray flux and the rest-frame luminosity light curves (left and right panel, respectively). The light curves were constructed by using the median values for the break times before and after the plateau phase and the decay slope α_{X2} and α_{X3} . We used the median values for the fluxes and luminosities at the break time after the plateau phase ($F(T_{\text{break},2}) = 5 \times 10^{-12} \text{ erg s}^{-1} \text{ cm}^{-2}$ and $L(T_{\text{break},2}) = 1.7 \times 10^{47} \text{ erg s}^{-1}$) as the normalization points of the light curve.

The redshift distribution of the 232 *Swift*-detected bursts with spectroscopic redshift measurements is shown in Figure 6. The mean redshift of all *Swift* bursts is $z=2.03$ and the median $z=1.76$ which is lower than for the bursts detected during the first two years of *Swift* operation ($z=2.30$; Grupe et al. 2007). Recently Coward et al. (2013) have studied the evolution of the mean redshifts of *Swift*-detected GRBs since

2005 and shown that the mean redshift of *Swift*-discovered bursts has decreased over the course of the mission. There is a significant difference in the redshift distributions of short and long GRBs, with short GRBs being detected only at the lower end of the redshift distribution. This is a selection effect. As shown by e.g. Bernardini et al. (2012b) and Margutti et al. (2013), short bursts are less energetic than long bursts (see also below) which results in a lower fluence. The cause of the different energetics of short and long GRBs is most likely the result of their different progenitors (e.g. Salvaterra et al. 2008; Fong et al. 2013; Rowlinson et al. 2013) which then results in different redshift distributions. As a consequence, short bursts which have lower energy appear to be undetectable at high redshifts.

3.2. Selection Effects

Before we start any discussion on results of the correlation analysis from our sample we need to be aware of any selection biases in the sample that may lead to non-physical results. One of these selection biases is displayed in Figure 28 which shows the observed 15-150 keV fluence in the *Swift* BAT and T_{90} which seem to be very strongly correlated ($r_s=0.667$, $T_s=22.85$). However, this is purely a selection effect driven by the detector properties. We only detect low-fluence bursts when their energy is released in a relatively short amount of time. If the energy is spread over a longer time span the signal will be dominated by noise and the BAT will not be able to trigger on this event. This selection effect means that low fluence bursts have to be short in order to be detected, explaining the upper left part of the diagram. On the other hand the void at the lower right part of Figure 28 may be of physical nature. There are two effects here:

1. a highly energetic burst (and high fluence burst) requires a certain amount of time to release the energy and
 2. related to this, short bursts generally speaking have lower luminosities/energies than long GRBs (e.g. Margutti et al. 2013).
- 1) The reason why high fluence bursts are seen with longer T_{90} may be that there is only some maximum amount of flux (or luminosity) that can

be generated by the burst. Therefore a high fluence burst would need a longer time span to release its energy than a low fluence burst.

2) In order to detect a short burst with a high fluence requires that this burst occurs at close distances. For example the short GRB with the highest fluence (1.16×10^{-6} erg cm $^{-2}$) is GRB 051221A (Burrows et al. 2006) with a redshift of $z=0.547$, resulting in a luminosity distance of 3150 Mpc. To detect this GRB with a fluence of the order of 10^{-4} erg cm $^{-2}$ it needs to occur within 390 Mpc equivalent to a redshift of $z=0.085$. Although this is not impossible and *Swift* has detected a few bursts with redshifts lower than 0.085 (4 to be precise) the probability of detecting a relatively luminous short burst like GRB 051212A at such a low distance is low. This is mostly due to the general space density of GRBs and their luminosity functions (see also Section 3.5) and the much lower comoving volume at a redshift of 0.085 than at higher cosmological redshifts. Having a less luminous burst explode and detect it with a fluence in the 10^{-4} range requires an even closer distance.

How does the T_{90} - fluence selection effect affect other correlations? We found a mild correlation between T_{90} and the isotropic energy in the 15-150 keV BAT band. However, this correlation may mostly been driven by this selection effect.

Another question that may raises concerns is whether T_{90} really is a good parameter to describe a burst. As pointed out by e.g. Zhang (2012) and Qin et al. (2013), T_{90} is strongly detector dependent. This is similar to a hardness ratio which does not allow a direct comparison between different missions. However, as long as we use both parameters from samples using only data from the same detector it may not be a problem. Still, for *Swift*-BAT GRBs we typically use the 2s division line between short and long duration GRBs as it was defined by Kouveliotou et al. (1993) for Gamma-Ray Observatory BATSE-detected GRBs which was operating at much higher energies than the *Swift* BAT. However, as we have pointed out in Section 3.1 the division between *Swift* BAT-detected short and long duration GRBs occurs at earlier times. It has been recently shown also by Bromberg et al. (2013) that the cutoff line at 2s between short and long duration GRBs detected by the *Swift*-BAT is not a good choice and it is more appropriate for *Swift* discovered bursts to

have the cutoff at around 0.8s. We will discuss this in more detail in Section 4.4.

There is another problem that has recently been pointed out by several authors: high-redshift bursts tend to have rather short T_{90} (Littlejohns et al. 2013; Tanvir et al. 2012; Kovecski 2012). Bursts like GRB 090423 or GRB 080913 (e.g. Zhang 2009) which are the GRBs with the highest spectroscopically measured redshifts (8.2 and 6.7), had T_{90} of 8.0 and 10.3s, respectively, which in the rest-frame suggests that these maybe short bursts. However, the reason for these short T_{90} may not be a physical property of the bursts, rather a consequence of the detector threshold. Because the flux light curve of the prompt emission observed from a high-redshift burst appears to be fainter than that of a low-redshift burst on average, a detector triggers on the prompt emission later than for a low-redshift burst because the main part of the prompt emission light curve is below the detector threshold (Littlejohns et al. 2013). We basically observe the tip of the iceberg of the prompt emission of high-redshift bursts where most of the prompt emission is lost in the noise. Nevertheless, the short duration of the observed prompt emission is not a general property of high-redshift bursts (E.g. GRB 050904 which is a burst at the redshift of $z=6.2$ had a $T_{90}=181.7$ s). The concern is how much does this threshold effect influence the results we found for our *Swift* GRB sample? If there is a significant effect on the sample we would expect to see a decrease of T_{90} with increasing redshift. This relation is plotted for the observed and rest-frame T_{90} in Figure 27. However, we do not observe such an effect. Therefore we conclude that although some high-redshift bursts appear to have rather short duration prompt emission due to the detector threshold this effect is not significant for the whole sample.

Nevertheless there is another concern regarding high-redshift bursts (Coward et al. 2013) As we mentioned at the beginning of this subsection, the fluence and T_{90} are strongly correlated because of how the BAT triggers on bursts. Although the mean and median fluences and T_{90} of all GRBs and high-redshift bursts are essentially the same (Table 1) this picture changes when looking at the rest-frame parameters: We do not find very long T_{90} GRBs at high redshifts and high-redshift bursts

are significantly more luminous and energetic than compared with the total GRB sample. The same selection bias that there are long GRBs with low fluence also excludes long high-redshift GRBs from detection. The problem here is that due to time-dilation ($T' = (1+z) \times T$) a rest-frame long burst becomes even dramatically longer in the observed frame. This means that the fluence of these bursts will be smeared out over a longer time span with the consequence that due to the detector noise the burst remains undetected. In other words, in order to detect a GRB with the *Swift* BAT at high redshifts, its rest-frame T_{90} needs to be relatively short and it has to be a highly energetic burst. Consequently this means that the majority of high-redshift bursts are missed by the BAT. As pointed out by Wanderman & Piran (2010) this prediction, however, also strongly depends on the star formation rate at high redshifts.

3.3. Correlation Analysis

Throughout this subsection we look at correlations between observed and rest-frame GRB prompt and afterglow emission parameters. In particular we are interested in strong relations between prompt and afterglow properties. One of the goals is to be able to make predictions of the behavior of the X-ray afterglow based on prompt emission properties. The correlations between these parameters are listed in Tables 2 and 3 using Spearman rank order correlation coefficients and Student's T-tests. While Table 2 lists the correlation results of the observed parameters of all 754 GRBs in our sample, Table 3 lists the correlations between the rest-frame parameters of 232 GRBs with spectroscopic redshifts only. In this subsection we will only discuss those correlations which are statistically significant, meaning that the probability of the correlation being just random is $P < 10^{-3}$. Correlations quoted in this subsection apply to the whole GRB sample if not noted otherwise. We will primarily focus on those relations which clearly connect the prompt and the afterglow phase. Other relations are shown in Appendix D. In addition to the Spearman rank order correlation coefficient, we also determined Kendall's τ value and the Pearson correlation coefficient. In Tables 10 and 11 in Appendix D the Kendall τ value and the Pearson correlation coefficients for all GRBs and those GRBs with spectro-

scopic redshift measurements are shown, respectively.

We have already mentioned in section 3.1 that the photon spectral index in the 15-150 keV BAT energy band is flatter for short-duration GRBs than for long-duration GRBs (Figure 31). Figure 7 shows the relation between T_{90} in the observed and rest-frame and the 15-150 keV photon index Γ . In the observed frame clearly there are two groups of GRBs. This effect, however, becomes smeared out in the rest-frame. The reason that the percentage of short-duration GRBs with spectroscopic redshift is significantly lower than in long-duration GRBs, is simply because they are much more difficult to follow up due to their lower flux/fluence and faster decay slopes compared with long-duration GRBs.

Early studies of *Swift*-detected GRBs noticed a close connection of the energetics of the prompt and the afterglow emission (e.g. O'Brien et al. 2006; Willingale et al. 2007; Gehrels et al. 2008) and more recent studies by e.g. Margutti et al. (2013) confirm these findings. The left panel of Figure 8 shows the correlations between the fluence in the 15-150 eV band during the prompt emission and the 0.3-10 keV fluence in the afterglow emission. The right panel displays the luminosities in the 15-150 keV band of the prompt and the 0.3-10 keV luminosity in the X-ray afterglow emission. Clearly, as expected, the energetics of the prompt and afterglow emission are very strongly correlated: bursts with high 15-150 keV fluence in their prompt emission will have high X-ray luminosities/fluxes in the afterglows and vice versa.

In our paper we go a step beyond the energetics and ask what other prompt and afterglow properties are correlated. One of our main results is that there are clear correlations between the BAT 15-150 keV T_{90} and the break times in the X-ray afterglow light curves before and after the plateau phase. These findings apply to observed as well as to rest-frame parameters. The left panel in Figures 9 and 10 show the observed values, while the right panel display the values in the rest-frame of the burst. Although there is a large scatter in all these relations, there are clearly correlations: GRBs with long T_{90} start their X-ray afterglow plateau phase at later times and end the plateau phase later than GRBs with shorter T_{90} .

In correlations between T_{90} and break time before the plateau phase $T_{\text{break},1}$ we found a Spearman rank order correlation $r_s=0.328$, $T_s=6.776$ (N=384 GRBs) which implies a probability of $P < 10^{-8}$ of a random result for the observed values, and $r_s=0.371$, $T_s=4.767$ (N=144 GRBs) which $P = 4.5 \times 10^{-6}$ for the values in the rest-frame. This relationship between the prompt and afterglow emission is especially strong between T_{90} and the break times after the plateau phase $T_{\text{break},2}$. For the observed values we found $r_s=0.495$, $T_s=11.615$ (N= 417 GRBs) with $P < 10^{-8}$, and $r_s=0.439$, $T_s=6.421$ (N= 175 GRBs) with $P < 10^{-8}$ for the times in the rest-frame. What the relations between T_{90} and the break times in the X-ray light curves suggest is that there seems to be a strong connection between the prompt and the afterglow emission. What these relations - long T_{90} - later afterglow break times allow is in principle to make predictions of the behavior of the X-ray afterglow light curve based on prompt emission properties. If this is true then we would also expect to see a correlation between the spectral slopes in the BAT 15-150 keV and the X-ray 0.3-10 keV band.

The correlation between the BAT 15-150 keV hard X-ray photon index Γ and the X-ray energy spectral slope β_X is displayed in Figure 11. Again, although there is a large scatter in this relation, the two properties are clearly correlated and is another hint that prompt and afterglow phases are clearly linked. GRBs with steep spectral in the 15-150 keV band also show steeper X-ray spectra. The Spearman rank order correlation coefficient is $r_s=0.179$ with $T_s=4.560$ (632 GRBs) and a probability $P = 6.32 \times 10^{-6}$ of a random result. We also checked if there is any (anti-)correlation between spectral indices and the rest-frame break times before and after the plateau phase. We could not find any significant correlation between these properties (Table,2). There is only a weak trend between the X-ray spectral slope and $T_{\text{break}2,z}$ that bursts with later break times have steeper X-ray spectra, but the probability is 1.5% that this is just a random result.

The BAT 15-150 keV photon index Γ also strongly anti-correlates with the decay slopes during the plateau and normal decay phases α_{X2} and α_{X3} . The decay slope during the plateau phase anti-correlates with Γ with a Spearman rank or-

der coefficient $r_s = -0.260$ with a Student's T-test $T_s = -6.232$ and a probability of a random distribution of $P < 10^{-8}$ (539 GRBs), and $r_s = -0.313$, $T_s = -7.154$ and $P < 10^{-8}$ (475 GRBs) for the 'normal decay slope α_{X3} . These relations are displayed in Figure 12. Again, these are relations clearly link the prompt with the afterglow emission: bursts with steeper 15-150 keV spectra have flatter decay slopes during the plateau and normal decay phases. These relations can be used to estimate the behavior of the X-ray light curve.

We noticed strong correlations between the fluence in the 15-150 keV BAT energy band and the decay slopes in the X-ray light curve α_{X2} and α_{X3} , as shown in Figure 13. We find Spearman rank order correlation coefficients of $r_s=0.270$ and 0.225 , Student's T-test values $T_s=6.482$ (for 538 GRBs) and 5.043 (475 GRBs) with probabilities of a random result of $P < 10^{-8}$ and 5.6×10^{-7} for the fluence vs. α_{X2} and α_{X3} correlations, respectively. These relations become apparent in our *Swift* GRB sample due to the large number of bursts. Although this is purely a phenomenological relation which is most likely due to selection effect, we can still take advantage of these relations to predict the behavior of the X-ray light curve. Note that for the relations of luminosity and isotropic energy with α_{X2} and α_{X3} there are only trends that bursts with higher fluence in the BAT energy band decay faster in X-rays (see Table 3)

The next step is to see if the luminosity in the prompt emission also anti-correlates with the break times in the X-ray light curve. As shown in Figure 14, this is indeed the case for both the break times before and after the plateau phase $T_{\text{break}1,z}$ and $T_{\text{break}2,z}$, respectively. In the first case, the Spearman correlation coefficient and Student T-test values are $r_s = -0.587$, $T_s = -8.614$, with $P < 10^{-8}$ (143 GRBs), and for the break time after the plateau phase $r_s = -0.413$, $T_s = -5.956$ with $P = 1 \times 10^{-8}$ for all GRBs (175 GRBs) and $r_s = -0.433$, $T_s = -6.187$ with $P < 10^{-8}$ for the long GRBs (168 GRBs) for all long GRBs. This is a real anti-correlation between the prompt luminosity and the afterglow emission light curve break times. This is not necessarily true, however, for the connection found by e.g. Dainotti et al. (2008) between the break time after the plateau phase $T_{\text{break}2,z}$ and the luminosity at $T_{\text{break}2,z}$, which are strongly anti-correlated. The prob-

lem is that $T_{\text{break}-2}$ and $L_{0.3-10\text{keV}}(T_{\text{break}-2})$ are not independent parameters. Because the decay slope of the ‘plateau’ phase is not 0⁴, a later break time will automatically result in a lower flux/luminosity. Although there is a strong correlation between $T_{\text{break}2,z}$ and the luminosity at $T_{\text{break}2,z}$ as reported by Dainotti et al. (2008) also in our sample ($r_s = -0.559, T_s = -8.785, P < 10^{-8}$) there is also a strong anti-correlation with the flux at that time. As a consequence, any possible physical cause for this relation can not be disentangled from the fact that at a later time a burst will automatically appear to be fainter than at earlier times.

Note that the anti-correlations between prompt emission luminosity and isotropic energy and break times in the X-ray afterglow light curve can be used as a diagnostic to determine if a redshift measured of a galaxy in the direction of the burst is actually associated with the burst or just a random galaxy in the line of sight. A good example here is GRB 051109B (Tagliaferri et al. 2005). This burst has an observed $T_{90} = 15 \pm 1\text{s}$ and a fluence of $(2.7 \pm 0.4) \times 10^{-7} \text{ erg cm}^{-2}$ (Hullinger et al. 2005) and break times in the X-ray light curve at $T_{\text{break}1}=200\text{s}$ and $T_{\text{break}2}=1430\text{s}$. Perley et al. (2005) reported of a galaxy in the direction of this burst and measured a redshift of $z=0.080$. Is this galaxy associated with the burst or not? The answer is that this association is most unlikely. At the redshift of the galaxy the luminosity distance is $D_L=360 \text{ Mpc}$ which results in a 15-150 keV luminosity $L_{15-150\text{keV}} = 3 \times 10^{47} \text{ erg s}^{-1} \text{ cm}^{-2}$ and an isotropic energy $E_{\text{iso}} = 4 \times 10^{48} \text{ erg}$. These values are far off the relations shown in Figures 41 and 14. We can therefore conclude that the galaxy found by Perley et al. (2005) at a redshift of $z=0.08$ is not associated with GRB 051109B and just a random foreground galaxy. As pointed out by Campisi & Li (2008) with increasing magnitude limits of newer telescopes the chance coincident of a GRB with a foreground galaxy at redshifts $z < 1.5$ is of the order of a several percent.

⁴In a matter of fact, the median decay slope during the plateau phase is 0.6.

3.4. Principal Component Analysis

So far we have only looked at bivariate correlations and we have found strong correlations between GRB prompt and afterglow properties. One step further is the statistical analysis in a multi-dimensional parameter space. The goal here is to search for any underlying fundamental property that is driving these relation. One of the standard tools in multivariate analysis that may answer this question is the Principal Component Analysis (PCA; Pearson 1901). The idea of a PCA is to reduce the number of significant sample parameters to a small number of parameters that capture most of the variance in the data. For example, in AGN, the measured parameters are primarily driven by the mass of the central black hole and the Eddington ratio L/L_{Edd} (e.g. Grupe 2004; Boroson 2002). In a mathematical sense, the PCA searches for the eigenvalues and eigenvectors in a correlation coefficient matrix. A good description for the application of a PCA in astronomy can be found in Francis & Wills (1999) and Boroson & Green (1992).

We applied a PCA to the bursts in our sample for which the following input parameters were available: $\log T_{90,z}$, $\log T_{\text{break}2,z}$, α_{X2} , β_X , Γ , and the rest-frame 15-150 keV luminosity (175 GRBs in total). The reason why we do not include all properties as listed in Table 3 is because some of these have obvious correlations, such as $T_{\text{break},1}$ and $T_{\text{break},2}$. We want the input properties as independent as possible. We applied the PCA in the statistical package **R** (e.g. Crawley 2007; The R-Team 2009). All input parameters were normalized by the standard normalization $x_{\text{norm}} = \frac{x - x_{\text{mean}}}{sd(x)}$ where $sd(x)$ is the standard deviation of the parameter x . The results of this PCA are summarized in Table 4. The first two Eigenvectors from the PCA account for 60% of the variance of the sample. The most dominant of these, Eigenvector 1, accounts for almost 40% of the variance. It strongly correlates with the 15-150 keV rest-frame luminosity and anti-correlates with all other parameters, except for the decay slope during the plateau phase, α_{X2} . This may suggest that Eigenvector 1 in our sample presents the 15-150 keV luminosity. In order to test this hypothesis we excluded the 15-150 keV luminosity from the input parameters and ran another PCA

on the sample. The results of this PCA are listed in Table 5. This analysis agrees with the first PCA that included the 15-150 keV luminosity.

Using the later analysis, we calculated the first eigenvector for each GRB and plotted the eigenvector 1s vs. the 15-150 keV luminosity and isotropic energy as shown in Figure 16. If the conclusion, that GRBs are primarily driven by their energetics is correct, then the eigenvector 1 - energy relation has to hold also for energies determined independently by other missions. We used the bolometric energies listed in Nava et al. (2012) for about 30 GRBs. This relation is displayed in the right panel of Figure 16. Although the number of GRBs is small, they still follow the trend expected from our PCA. We can conclude that eigenvector 1 in our GRB sample represents the rest-frame 15-150 keV luminosity and/or the isotropic energy which seem to be the strongest drivers for the prompt and afterglow emission properties in our sample. Note, that Margutti et al. (2013) came to a similar conclusion using $E_{\gamma,iso}$, E_{peak} , L_{peak} , $T_{90,z}$, and the isotropic energy in the X-ray band as input parameters of their PCA of their GRB sample (R. Margutti, priv. communications). Although one has to be very careful comparing PCAs from different samples with different input parameters, it seem to suggest that the energetics is the most important underlying property of a GRB.

The second most relevant component, eigenvector 2, strongly correlates with T_{90} and the slope of the plateau phase α_{X2} , and anti-correlates with the spectral slope in the 15-150 keV and 0.3-10 keV energy bands Γ and β_X . There is, however, only a light correlation with the break time after the plateau phase T_{break2} .

3.5. GRB in a cosmological context

While Log N - Log S tests and luminosity functions are standard tools in quasar cosmology studies (e.g. Richards et al 2006; Ross et al 2012) they have only been applied to GRBs in a few studies recently. The luminosity function is usually defined as

$$\Phi(L, z) = \frac{\Phi^*(L_{break}(z))}{(L/L_{break}(z))^a + (L/L_{break}(z))^b} \quad (1)$$

where Φ^* is the number density at the break

luminosity $L_{break}(z)$, and a and b are the slopes of the luminosity function before and after the break.

The problem with GRBs in the pre-*Swift* era has been that only for a handful of bursts redshift measurements existed. At the time it was only possible to discuss GRB luminosity function in a theoretical context (e.g. Kumar & Piran 2000). This has changed since *Swift* and luminosity functions have been derived from *Swift* bursts (e.g. Schmidt 2009; Wanderman & Piran 2010; Cao et al. 2011; Salvaterra et al. 2008, 2012).

The log N - log S diagram using the 15-150 keV fluence in the BAT band is shown in Figure 17. This diagram contains the observed 15-150 keV fluence (754 bursts) as well as the rest-frame k-corrected fluence (232 bursts). The parameters of the log N - log s function are $N^* = (1.733 \pm 0.018) \times 10^{-2}$, $a = (7.41 \pm 2.06) \times 10^{-3}$, $b = 1.185 \pm 0.018$, and the break fluence $S_{break} = (1.339 \pm -0.031) \times 10^{-6}$.

We constructed luminosity functions in 6 redshift intervals as displayed in Figure 18. The parameters for fits to the GRB luminosity functions as displayed in that figure are listed in Table 6.

We noticed that the slope of the high luminosity end of the luminosity functions with $L > L_{break}$ becomes steeper with increasing redshift as displayed in Figure 19. This is the opposite to what has been reported by Richards et al (2006) for quasars in the SDSS for which the high-luminosity end of the luminosity function becomes flatter with increasing redshift. As expected, the luminosity where the luminosity function breaks L_{break} shifts to higher luminosities with increasing redshift. The GRB number per Gpc $^{-3}$ however, decreases with increasing redshift.

Now one step further is to look at the rates GRBs occur in a space volume per year as shown in Figure 20. This rate contains long as well as short bursts. The way we estimated these numbers is to take the number of *Swift*-discovered bursts with spectroscopic redshift measurement per redshift interval and assume the same underlying redshift distribution for the remaining *Swift* bursts. This number was then multiplied by the ratio of the whole sky in square degrees compared with the BAT sky coverage. This plot suggests that the GRB rate is significantly higher in the current Universe than at early times. This however, is a very

naïve picture. The number of bursts with spectroscopic redshifts measurements is biased against high redshift bursts. Therefore we can not necessarily assume that the redshift distribution of the *Swift* bursts without redshift measurements is the same as for those with redshift measurement.

Another attempt to tackle this problem is to have a look only at the space density of the most luminous bursts. This is shown in Figure 21. Here we consider only those bursts who have a luminosity of $L_{15-150\text{keV}} > 10^{52}$ erg s⁻¹. What we see is that the number of *Swift*-detected bursts per Gpc³ decreases significantly in the local Universe. This is similar to the “cosmic downsizing” that is known for bright quasars (e.g. Richards et al 2006). If this is true, then we should see this effect of “cosmic downsizing” also in a luminosity - redshift plot. The 15-150 keV luminosity vs. redshift is shown in Figure 22 and indeed there are no bursts with $L_{15-150\text{keV}} > 3 \times 10^{52}$ erg s⁻¹ at redshifts less than 1.5. Note, that the peak the quasar density is roughly at a redshift of $z=2.75$ (e.g. Richards et al 2006), similar to that of our GRB sample. This result is consistent with what has been found by Wanderman & Piran (2010). The space density of GRBs, thus decreases with increasing redshift. However, keep in mind that this may also be a selection effect. Because high redshift bursts are those which are not detected in the UVOT, often no one wants to take the risk of sacrificing valuable observing time on a burst that is simply too faint and not necessarily highly redshifted. As we see later in this discussion, bursts with redshift measurements tend to be brighter than those without redshift measurements. Nevertheless, the result shown in Figure 21 agrees with the cosmic star formation history (e.g. Hopkins & Beacom 2006).

3.6. Redshift Predictions

Spectroscopic redshift measurements exist for 232 *Swift*-onboard-discovered bursts. The problem with obtaining GRB redshifts is that a) the afterglows are faint to begin with, often fainter than 20th mag in R and b) they decay fast. So an optical observer has to decide quickly if it is worth spending valuable telescope time on a newly discovered burst. The capacity of detecting GRB afterglows in the optical and near infrared either by spectroscopic or photoscopic measurements has significantly increased in recent years especially

with the arrival of X-shooter at the ESO VLT and GROND at the ESO/MPI 2.2m telescope in La Silla (Greiner et al. 2008; Krühler et al. 2011).

In order to predict GRB redshifts ideally one would look for a relation between a redshift dependent (or distant-dependent) parameter and a redshift-independent parameter. This can be based purely of selection effects. In the past it has been suggested (Grupe et al. 2007) that bursts with significant excess absorption column densities above the Galactic value are low redshifts bursts. Ukwatta et al. (2010) found an anti-correlation between the spectral lag times in the BAT data and the isotropic luminosity. Recently Morgan et al. (2012) suggested a statistical method that applied a Random Forest technique to predict high redshift GRBs. To date this is the most advanced method to predict if a burst is at high redshift based on *Swift* data.

Let us start with an update on the redshift - excess absorption relation presented in Grupe et al. (2007). At that time the *Swift*-GRB sample only contained about 50 GRBs. Our new sample presented here contains more than 4 times as many bursts with spectroscopic redshifts measurements. Figure 23 displays the relation between $\log(1+z)$ and $\log(1+\Delta N_H)$, showing that in principle this method still holds. The only exception is the burst with the highest redshift, GRB 090423 for which we obtained an excess absorption column density of 5.8×10^{20} cm⁻². Equation 1 in Grupe et al. (2007) would have predicted a redshift of $z < 6.6$, which, however, would have been still a high redshift burst. Note also that the errors on the absorption column density for this burst are rather large and within the errors, GRB 090423 is still within the prediction.

In order to obtain a better discriminator for high redshift bursts we have to extend our simple redshift - ΔN_H relation. One discriminator here is a detection in the *Swift* UVOT. If the excess absorption is consistent with zero this means it is either a high redshift burst or a low redshift burst with no significant X-ray absorption. In the latter case this means that the burst will most-likely not be reddened significantly on the Optical/UV so it should be detectable in the UVOT. If UVOT does not detect this burst this makes it a high redshift candidate.

The next discriminators come from the BAT

data. Figure 24 displays the relation between redshift and the photon index Γ in the BAT band and the observed 15-150 keV fluence. As we can see from this plot, steep BAT spectra only occur in bursts with a redshift of less than 4. This is a simple selection effect. As shown in Figure 26 there is as strong anti-correlation between the BAT photon index Γ_{BAT} and the fluence in the 15-150 eV band. As shown in the right panel of Figure 24, bursts with a fluence larger than 10^{-5} erg cm $^{-2}$ are only seen in GRBs with redshifts lower than 4. Because of this and the anti-correlation between Γ_{BAT} and the 15-150 keV fluence, we can observe GRBs with steep 15-150 keV spectra only in bursts with relatively low redshifts.

The question is can we find a combination of observed parameters that can be correlated with a redshift (distance) dependent property. To explore this question, we performed a PCA on the three prompt emission parameters - T_{90} , fluence, and Γ . We then determined eigenvector 1 for each long-duration GRB and plotted this against the isotropic energy E_{iso} . This relation is shown in Figure 25. For the 216 long GRBs with spectroscopic redshifts in the sample, this is a strong anti-correlation with a Spearman rank order correlation coefficient $r_s = -0.572$ and $T_s = -10.15$ with a probability of $P < 10^{-8}$ that this is just a random distribution. This means that if we calculate eigenvector 1 for a newly discovered burst based on the BAT input parameters, we should be able to predict the isotropic energy in the BAT band. Nevertheless there is a lot of scatter in this relation which prevents a clear statement of the redshift of the burst. We examined this plot a bit further on selected high and low redshift bursts. These are shown as red circles and blue triangles, respectively. Clearly they form distinct groups in this diagram. For a given eigenvector 1, high redshift burst show larger isotropic energies than low redshift bursts.

If we can find another discriminator between low and high redshift bursts then we know in which group the newly discovered GRB belongs and we can use the eigenvector 1 of this burst in order to get an estimate of the isotropic energy. With this estimate and the knowledge of the 15-150 keV fluence, we can then estimate the distance to the burst and its redshift. Discriminators for high and low redshift bursts are: a) does the X-

ray spectrum show strong excess absorption? and b) is the afterglow detected in the UVOT or not?. Table 8 lists the mean, standard deviation, and median of observed prompt and afterglow properties of low ($z < 1.0$), intermediate ($1.0 < z < 3.5$) and high redshift bursts ($z > 3.5$). Besides that, low redshift bursts show enhanced excess absorption column densities, we also find that high redshift bursts tend to have flatter 15-150 keV photon indexes, steeper later time afterglow decay slopes, and lower fluence than low redshift bursts.

As an example, we can estimate the redshift of GRB 051109B, the GRB that was suggested to be associated with a nearby galaxy (Perley et al. 2005), however, as we showed in Section 3.3, this is most likely not the case and the redshift is probably much larger. Applying the method described above, we calculated an eigenvector 1 of $+1.9^5$ for this burst. From Figure 25 we can place the burst at a vicinity of $E_{\text{iso}} \approx 3 \times 10^{51}$ erg. The fluence of this burst was 2.7×10^{-7} erg cm $^{-2}$. Therefore the luminosity distance is roughly $D_L = 10$ Gpc, which using the cosmology calculator by Wright (2006) corresponds to a redshift of $z \approx 1.5$.

4. Discussion

The main motivation for our project is to search for relationships between GRB prompt and afterglow properties that suggest a close connection between these two phases. With *Swift* it is now possible for the first time to perform statistics on the rest-frame physical parameters of GRBs. Only since the launch of *Swift* have optical/NIR observatories been able to obtain spectroscopic redshifts for a significant number of GRBs. About 30% of all *Swift*-discovered bursts have spectroscopic redshifts. As recent papers by Margutti et al. (2013); Bernardini et al. (2012b); Nava et al. (2012), and Lü et al. (2010) show there is a close link between the energetics of the prompt and afterglow emission which seem to be driven by energetics. Our study presented here found new relations that support the connection between the prompt and afterglow phases.

⁵See Appendix E for how to calculate eigenvector 1.

4.1. Correlation analysis

As shown in the analysis section, there are several correlations between the prompt and afterglow properties of GRBs. We found that:

- The length of the prompt emission (a.k.a T_{90}) correlates strongly with the break time after the plateau phase, which is essentially the length of the X-ray afterglow plateau phase.
- The spectral slopes of the 15-150 keV prompt emission and the 0.3-10 keV X-ray afterglow emission are closely correlated.
- The X-ray afterglow decay slopes anticorrelate with the 15-150 keV spectral slope of the prompt emission.
- The X-ray afterglow decay slopes correlate with the rest-frame peak energy E_{peak} at high energies in the prompt emission.
- The X-ray afterglow decay slopes also depend strongly on the energy/luminosity of the burst.

The underlying mechanism of the shallow decay phase is poorly understood. In X-ray afterglow observations, there is no change in the spectral slopes from the plateau phase to the normal decay phase, and in most of the cases the plateau flux joins smoothly with the normal afterglow (Liang et al. 2007). On the other hand the correlation between T_{90} and $T_{\text{break},2}$ points to the fact that the plateau is of internal origin, related to the central engine of the bursts. The fact that the spectrum does not change during $T_{\text{break},2}$, points to it either being determined by a geometric or a hydrodynamic effect. A similar correlation for a much smaller number of GRBs was found by Liang et al. (2007). The correlation suggests an approximate relation $T_{90} \propto T_{\text{break},2}$. Since there is significant scatter in the data, we only resort to qualitative interpretation.

There are many theories in the literature addressing the origin of the plateau phase (for a review, see Zhang 2007). The timescale of the plateau can be constrained by these. However, in most of these models it is difficult to link the prompt duration T_{90} to the plateau duration. One of the most discussed models

is the refreshed shocks (Rees & Mészáros 1998; Zhang et al. 2006): at the forward shock either by a smoothly decaying central engine luminosity ($L \propto t^{-q}$) or by a distribution of instantaneously ejected masses with a distribution of Lorentz factors down to few tens (Granot & Kumar 2006; Ghisellini et al. 2007). Models for the plateau phase include change in microphysical parameters with time (Ioka et al. 2006), emission by a distribution of ejected Lorentz factors (Granot & Kumar 2006), a strong reverse shock contribution (Genet et al. 2007; Uhm & Beloborodov 2007) or anisotropic jet structure (Eichler & Granot 2006; Toma et al. 2006),

A class of models explaining the plateau phase invokes energy injection from magnetars (Dai & Lu 1998; Zhang & Mészáros 2001) into the forward shock, similar to the refreshed shocks. These can reproduce the flattening in the X-ray light curve (Dall’Osso et al. 2011; Bernardini et al. 2012). The supply of energy is provided by the spin down energy of a newly born magnetar. In these scenarios the collapse to a black hole is delayed by the magnetar phase (Lyons et al. 2010). In relation to short GRBs, the injection of spin down energy by a magnetar and thus the plateau phase, can be linked to gravitational wave emission (Rowlinson et al. 2013; Corsi & Mészáros 2009). In these models the prompt emission is tentatively produced by local processes to the outflow (e.g. magnetic dissipation or shocks close to the magnetar wind photosphere Metzger et al. (2011)), which cannot be readily related to the length of the plateau phase in the afterglow.

- The most straightforward way of interpreting the $T_{90} - T_{\text{break}}$ correlation is the model by Kumar et al. (2008) which addresses both the prompt emission and the plateau phase. In this model the X-ray luminosity is driven by the mass accretion rate. They envisage a massive star with a core and an envelope. The part of the core collapses to form a black hole. Accreting the remainder of the core produces the prompt phase. From the outermost parts of the core until the inner part of the envelope the density drops suddenly, producing the steep decay part. The envelope is accreted subsequently.

The duration of accretion is roughly the fallback time, $t_{fb} \propto M(< r)^{-1/2} \times r^{3/2}$, $M(< r)$ is the mass within radius r , generally dominated by the black hole mass. Thus T_{90} corresponds to the core accretion time and $T_{\text{break},2}$ to the envelope accretion in this model. The correlation results in $r_{\text{core}} \propto r_{\text{envelope}}$. The drawback of this scenario is that it predicts a steep decay at the end of the shallow decay phase corresponding to the outer radius of the star. This is only observed in a few cases.

- A natural explanation can be given to the correlation if the reverse shock is at the origin of the plateau. The details of such an interpretation are described, for example in Genet et al. (2007); Uhm & Beloborodov (2007). The prompt duration (T_{90}) is defined as the active phase of the central engine (e.g. in a photospheric model) and this also defines the width of the ejecta. The plateau duration in this scenario corresponds to the ejecta crossing time by the reverse shock which is then proportional to T_{90} .

The gamma-ray luminosity L anti-correlates with the plateau break time $T_{\text{break},2}$. This can be understood in terms of an approximate energy conservation. For a universal ratio between the prompt and plateau luminosity, the increase in energy emission in the prompt phase will result in a smaller emitted energy in the plateau, similar if we had a constant energy reservoir.

There is a similar observed anti-correlation between the luminosity at the end time of the plateau (Dainotti et al. 2008; Bernardini et al. 2012) which can be explained in the magnetar model. We can tentatively understand this anti-correlation within the framework of the magnetar model as follows: both the prompt and afterglow luminosity depend on some positive power of the magnetic field (e.g. $L_{\text{plateau}} \propto B^2$) while the spin-down timescale, which is related to $T_{\text{break},2}$ is proportional to B^{-2} . This would qualitatively explain the anti-correlation. Other properties such as the neutron star radius or the rotation period would act to strengthen the anti-correlation.

As we will see below (Section 4.3), it seems that these (anti)-correlations are primarily driven by the luminosity/energy of the burst. What is inter-

esting among these relations are those between the decay slopes of the X-ray afterglow emission with the rest-frame E_{peak} and the energy and luminosity of the burst. While the energy, luminosity and rest-frame E_{peak} are all redshift (or distance) dependent, the decay slopes are not. In principle we do have a redshift indicator. However, at this point we can not use the slopes α_{X2} and α_{X3} as redshift indicators due to the large scatter in these relations (see Figure 15). As we will discuss later, machine learning techniques may be the solution to take advantage of these redshift indication relations.

4.2. Multi-variate Analysis

Using the $\log T_{90,z}$, $\log T_{\text{break},2,z}$, α_{X2} , Γ , and β_X as representatives of the prompt and afterglow emission of a subsample of 175 GRBs with canonical X-ray light curves, the results from the PCA show that the first two eigenvectors account for more than 60% of the variance in the sample. We can see directly that Eigenvector 1 represents the luminosity and/or the isotropic energy of the GRB in the rest frame 15-150 keV band (Figure 16). This is somewhat expected. What is interesting to note is that although using different input parameters (see Section 3.4), Margutti et al. (2013) came to a similar conclusion. The question that remains is what actually determines the luminosity and energy release of a burst?

Are GRBs with spectroscopic redshifts, in particular those used in the PCA, representative of the whole sample? In other words can conclusions that we draw from the statistical analysis on this sub-sample of bursts, including PCA, be applied to the rest of the sample which does not have redshift measurements? This is an important question, because as we have discussed earlier, the entire sample is driven by selection biases. In order to test this, we need to look at the statistics between the GRB samples with and without spectroscopic measurements.

We have mentioned already in section 3.2, *Swift* GRBs are affected by selection effects, primarily by the BAT properties. As pointed out by Coward et al. (2013) selection biases become even more important when dealing with high-redshift bursts. In order to answer this question we looked at the observed parameters of the samples for GRBs with and without spectroscopic redshift

measurements and those used in the PCA. The mean, standard deviations, and median of each sample are listed in Table 7. All parameters like T_{90} or α_{X2} have very similar means, standard deviations, and medians and suggest that these are all drawn from the same underlying distribution. However, this is not true for the observed 15-150 keV fluence and the peak energy E_{peak} . Here the distributions seem to be different: GRBs with spectroscopic redshifts have on average a fluence twice as high when compared with GRBs with no redshift measurements. We performed Kolmogorov-Smirnov tests on the samples with GRBs with and without spectroscopic redshift measurements and found that indeed the distributions in the fluence and E_{peak} of these two samples are drawn from different populations. For the fluence we found $D=0.2166$ with a probability $P < 10^{-4}$ of a random result and for E_{peak} $D=0.30$ and $P = 0.002$. Clearly, the bursts with redshift measurements are biased towards brighter GRBs. As shown in Table 8, this is really a selection effect between burst with and without redshift and not driven by different redshift intervals. What this means is that these GRBs also more likely to have optical counterpart and as a result will be observed preferentially by ground-based observers. This becomes apparent when looking at the UVOT detections in both samples: while 2/3 of all GRBs with spectroscopic redshift measurements have UVOT detections, this is only true for 17% of the GRBs without spectroscopic redshift measurements. Nevertheless, the fact that otherwise the observed parameters of the bursts are very similar suggests that they are drawn from the same population. If this is true then the correlations found among the rest-frame parameters in bursts with redshifts also apply to those bursts without redshift measurements. In particular, the conclusion of our PCA that the energetics is the main driver in GRB properties does therefore apply to all GRBs.

4.3. What is driving the prompt and afterglow properties?

As we have seen from the PCA, properties of the prompt and afterglow phases seem to be driven primarily by energetics. This means the largest relative scatter in the multidimensional data cloud can be accounted for by luminosity. In other

words, if we know the luminosity, we have accounted for a high percentage of the information otherwise attainable. Also the luminosity changes by 5 orders of magnitude, more than any other parameter. There are two viable mechanisms for extracting luminosity from the black hole - accretion disk system

If the luminosity is extracted from the central engine by the Blandford Znajek (Blandford & Znajek 1977) mechanism, this means $L \propto a^2 B^2 M^2$, where a is the dimensionless spin parameter, B is the magnetic field threading the central engine, and M is its mass. In current models the mass can have a spread of one order of magnitude, the rotational parameter is ideally around 1/2 for maximum efficiency, and it cannot introduce a large amount of variance. Thus the magnetic field has to account to the bulk of the variance. If the jet is launched by neutrino emission from the disk, the luminosity scales as: $L \propto \dot{M}^{9/4} M^{-3/2}$ (Zalamea & Beloborodov 2011). In this scenario the large variance in luminosity can be accounted by variation in the accretion rate by two orders of magnitude.

However, what is really behind all those properties, or in other words, what determines the energetics of a burst? Part of the problem is that for all correlations mentioned here we measured isotropic energies and luminosities. We know, however, that in a GRB the outflow is collimated. This may explain the anti-correlation we have found between the luminosity and energy of the prompt emission with (rest-frame) T_{90} and break times before and after the plateau phase. Naïvely one would assume that the more energetic a burst is the longer its T_{90} and the plateau phase start and end times. However, as we have shown this seem to be not the case. We do, however, for all of our correlations assume isotropic energies/luminosities. What may be the case is that bursts which short T_{90} and break times before and after the plateau phase are those bursts which outflows are highly collimated. Correcting for collimation means that the total energy release of these bursts is significantly lower than in burst which are less collimated. This means that if calibrated T_{90} and the break times can be used as a measure of the jet opening angle. This relation then would be somewhat similar to the jet opening angle - jet break times relation found by Frail et al. (2001) for optical and radio

afterglows. What this means is that bursts which large opening angles are the bursts which are intrinsically less energetic and show the shorter T_{90} and break times. This is exactly what we see in the second eigenvector in our PCA. The second Eigenvector may be the jet opening angle.

A connection between the X-ray spectral slope and the decay slopes in the light curve is expected from for example the closure relations (Racusin et al. 2009; Zhang & Meszaros 2004; Zhang et al. 2006). The big question remaining is, can we predict the behavior of the X-ray afterglow, assuming a canonical behavior, based on properties measured from the prompt emission. If this is possible then it gives us a handle on how to plan future observations of the X-ray afterglow. We have already seen that T_{90} and the break times before and after the plateau in the X-ray afterglow light curves are strongly correlated. So one prediction we can do is that bursts with a short T_{90} will show early breaks in the X-ray light curves. Although this correlation is statistically very strong ($P < 10^{-8}$), the scatter in the relation is large, making it impossible to derive a precise prediction of the break times based on T_{90} . We have also found that the photon spectrum measured in the prompt emission in the BAT 15-150 keV band is strongly anti correlated with the X-ray afterglow decay slopes. So, if for example the 15-150 KeV hard X-ray photon index Γ is flat, the the X-ray afterglow light curve decay slopes are most likely to be steep and vice versa. Again, this seem to be linked to the energetics of the burst. More luminous/energetic bursts have flatter hard X-ray spectra (see Figure 40). Nevertheless, we do not find a clear correlation between the luminosity and energy and the decay slopes in the X-ray light curves. The correlation between E_{iso} and the decay slope in the plateau phase α_{X2} is mild ($r_s=0.240$, $P = 5 \times 10^{-4}$) and the ‘normal’ decay slope α_{X3} with $r_s=0.306$ and $P = 3.1 \times 10^{-3}$ (see Table 3). So, the X-ray afterglows of more energetic bursts decay faster than those of less energetic bursts. This is somewhat the opposite than what one would normally expect. The reason here again may be the opening angle of the burst. because we do all our correlations based on E_{iso} we do not know, however, what the opening angle is and what the real energy release is.

The question is: do the properties of the

prompt emission of a burst determine the fate of the afterglow emission (assuming that the afterglow follows a canonical light curve). Or in other words, can we use the properties measured from the prompt emission to make predictions of the behavior of the X-ray afterglow. How will the light curve evolve?

One of the strongest correlations has been found between the 15-150 keV T_{90} and the break times at the beginning and end of the plateau phase in the X-ray light curve. This correlation gives us a rough estimate when these breaks happen based on T_{90} . A burst with a short T_{90} will have breaks in the X-ray light curve earlier than a burst with the long T_{90} . We have also found an anti-correlation between the 15-150 keV spectral slope Γ and the decay slopes in the X-ray light curve: a burst with a soft 15-150 keV spectrum will show flatter decay slopes than a burst with a harder 15-150 keV spectrum. Last but not least there are strong correlations between the fluence in the 15-150 keV BAT energy band and the decay slopes in the X-ray light curves. This results in that GRBs with high fluence decay faster in X-rays than GRBs with lower fluence.

4.4. *Swift* BAT short and long duration GRBs

The distribution of T_{90} shown in Figure 2 from BAT discovered GRBs suggests a bimodal distribution such has been found from BATSE bursts (Kouveliotou et al. 1993). However, due to the lower energy window of the *Swift* BAT, the detection rate of short GRBs is significantly lower and the deviation line between short and long-duration GRBs appears to be at shorter times compared with BATSE bursts. As pointed out by Bromberg et al. (2013) the deviation between collapsar (long GRBs) and non-collapsar (short GRBs) is driven by the different physical processes involved in these types. Bromberg et al. (2013) suggested that a deviation between short and long bursts at about 0.8s is more suitable for *Swift*-detected bursts. The observed T_{90} distribution (Figure 2) seem to support this time. As already found from BASTE bursts, short GRB tend to show harder spectra than long GRBs allowing another parameter to distinguish between the two classes. As shown in the distributions of the 15-150 keV photon indices Γ shown for long

and short GRBs in Figure 31 we do see the same effect in *Swift*-detected short and long GRBs as well. Figure 7 displays the relations between observed T_{90} and Γ , suggesting that there are two distinct groups in that diagram. As pointed out by Margutti et al. (2013), short GRBs appear to be less energetic compared with long GRBs. The consequence is that the fluence of short GRBs is significantly lower than that of long GRBs (Figure 32).

To find out if a burst belongs to one class of the other, one method that has been suggested in spectral lag analysis ([e.g. Ukwatta et al. 2012; Gehrels et al. 2006; Norris et al. 2000]). Another method is to apply statistical tools to the n-dimensional dataset and classify a GRB as a short or a long-duration GRB using cluster analysis (e.g. Everitt et al. 2011). We use the observed T_{90} , 15-150 keV fluence, and γ (all normalized) to span a three-dimensional space. We then run a hierarchical cluster analysis with centroid linkage on this dataset. Besides outliers which consist of GRB 060202B which has an extremely soft 15-150 keV X-ray spectrum (Aharonian et al. 2009), and GRB 060218 which is the low-luminosity GRB associated with supernova SN 2006aj (Soderberg et al. 2006), we see two main groups: Group 1 which consists of 685 members, and Group 2 consisting of 55 members - all short GRBs. There is a small third group which consists of GRBs 050416A, 050819, 050824, 060428B 061218, 080520, and 130608A. All these bursts are X-ray flashes (e.g. Sakamoto et al. 2008). This group has previously being suggested to be an intermediate duration GRB group by e.g. Mukherjee et al., (1998) and Veres et al. (2010). Figure 29 displays where these GRB groups appear in $T_{90} - \Gamma$, $T_{90} - \text{fluence}$, and $\Gamma - \text{fluence}$ diagrams. In these diagrams we displays group 1 as black crosses, group 2 as blue triangles and group 3 as red circles. These diagrams suggest that there is still some overlap between the groups, although the XRFs (group 3) are clearly distinct in the $T_{90} - \Gamma$ and Γ -Fluence diagrams. However, these diagrams are just two-dimensional projection of the three-dimensional space that is spanned by T_{90} , Γ and the 15-150 keV fluence. In order to really see if the three groups are disjoint we need to perform an axis transformation in the same way as it was done for the PCA. There-

fore we performed a PCA in the three parameter space and calculated the first two Eigenvectors for each burst. This diagram is shown in Figure 30. Clearly short and long GRBs and XRFs occupy different areas in this diagram: short GRBs have low eigenvector 1 and high eigenvector 2. XRFs on the other hand have very high eigenvector 2s. We can use this diagram in order to determine if a burst with a border line T_{90} is a short or a long duration GRB. In Appendix F we give the equations to determine where on the eigenvector 1 - eigenvector 2 diagram (Figure 30) a burst lies based on its observed BAT properties.

What this analysis also shows is that the previously considered short bursts GRB 050724 and GRB 051221A (e.g. Grupe et al. 2006; Burrows et al. 2006, respectively) are long GRBs. Other GRBs that were considered short burst in our previous analysis using the 2s cutoff line are: GRBs 070809, 071227, 080426, 080905, 081024, 090426, 100724A, 120403A, and 121226A. These bursts however, need to be classified as long GRBs. On the other hand, what our analysis also found were short GRBs with an observed T_{90} of 2.6 and 5.2s, GRBs 081016B and 110726A, respectively. Although their T_{90} is significantly longer than the 0.8s that we suggest from our analysis consistent with the results by Bromberg et al. (2013). These burst can be classified as short bursts due to their low fluence of the order of 10^{-7} erg cm^{-2} and hard X-ray spectra with $\Gamma=0.79$ and 0.64, respectively.

4.5. Luminosity Function

As for the luminosity functions we noticed a steepening of the slope for the higher luminosity part of the luminosity function with increasing redshift. However, one has to be very careful with drawing conclusions from these findings. The redshift distribution of GRBs is strongly biased against high redshift bursts, due to selection effects. As mentioned above, bursts without redshift measurements are drawn from a fainter population than bursts with redshift measurements. As also pointed out by Salvaterra et al. (2012), the *Swift* redshift sample is far from being complete. In order to obtain a complete sample, Salvaterra et al. (2012) proposed to use only bursts with high peak photon flux in the BAT band. This is not true for all *Swift* bursts with redshift measurements. Because we do have a bias against GRBs with low

fluence, the sample of bursts with redshift measurements is biased against high redshift bursts due to their typically lower fluence.

While the selection effect of GRBs with redshift measurements can explain the steep decay in the GRB rate at higher redshifts as shown in Figure 20, it does not explain the lower rate of bright GRBs in the low redshift Universe. While the smaller comoving volume for the Universe with $z < 1$ may explain part of this effect, it does not explain the whole picture. The comoving volume of the Universe with $z < 1$ is 153 Gpc^3 , it is 453 Gpc^3 in the redshift interval between $z=1$ and 2 , and about 250 Gpc^3 in the redshift intervals between $z=2$ and 4 in $z=0.5$ intervals. Another effect maybe metallicity and the evolution of the star formation rate. As shown by Grieco et al. (2012), the star formation rate in spiral galaxies peaks at a redshift of about 3 , which is consistent with the GRB rate shown in Figure 20. The conclusion here is that in the local universe only a smaller number of very massive stars is formed that will then end as a GRB, while at earlier epochs the rate of very massive stars has been higher.

4.6. Redshift predictions for *Swift*-detected GRBs

Last but not least we raise the question whether we can make rough predictions on the X-ray light curve behavior based on prompt emission properties? Can we use any relation between observed burst properties with redshift to make predictions on the possible redshift of the burst? We initially did this with the relation we found between the excess absorption in the X-ray afterglow X-ray spectrum (Grupe et al. 2007): GRBs with high excess absorption column density above the Galactic value are low redshift bursts. We found similar relations between the BAT photon index Γ_{BAT} and the observed 15-150 keV fluence and redshift: GRBs with steep Γ_{BAT} (> 2.0) and high fluence ($> 10^{-5} \text{ erg s}^{-1} \text{ cm}^{-2}$) are only seen in bursts with redshifts $z < 4$. Again, we can only discriminate low-redshift GRBs by their observed properties. One step further is the method we described at the end of Section 3.6, where we use a PCA to determine an eigenvector1 of a burst (see also Appendix E) based on the observed BAT parameters T_{90} , fluence and Γ . There is still strong scatter in this relation which still needs independent redshift

discriminators.

As we have shown in the discussion about the correlation analysis, most promising are the relations between the energy/luminosity of the GRB's prompt emission and the decay slopes in the X-ray afterglow light curves. This, however, requires that the burst has to be observed until the decay slopes can be measured, which typically means at least several hours after the burst for plateau phase as a minimum. So far no secure discriminator has been found for high-redshift bursts. Our plan is to apply machine learning techniques to the data set in order to obtain better redshift predictions based on observed GRB properties measured from *Swift* data, similar to what has been shown by Morgan et al. (2012). What is really needed is a relation between a redshift-independent parameter such as Γ and redshift-dependent parameters such as energy or luminosity.

5. Conclusions

The main result of our statistical study of *Swift*-discovered GRBs is that we found new evidence that the GRB prompt and afterglow emission are linked. This result is supported by the following findings:

- The BAT T_{90} and the break times in the X-ray light curve before and after the plateau phase are strongly correlated (Sections 3.3). Bursts with longer T_{90} tend to show later breaks in their X-ray afterglow light curves. This is a statistically highly significant result, suggesting a physical relationship between the high energy prompt and soft X-ray afterglow emission. These correlations appear to be strong in the observed as well as in the rest-frame.
- The hard X-ray photon index Γ of the prompt emission strongly anti-correlates with the decay slopes in the X-ray afterglow light curves. The observed fluence in the 15-150 keV BAT energy range anti-correlates with the decay slopes in X-rays. Together with the $T_{90} - T_{\text{break}}$ correlations these relations can be used to predict the behavior of the X-ray afterglow with a canonical light curve based on prompt emission parameter measurements.

- The Principal Component Analysis shows that the prompt and afterglow emission are driven primarily by the luminosity and/or isotropic energy release of the burst (sections 3.4, 4.3).
- A cluster analysis on the observed *Swift*-BAT parameters shows that short and long GRBs can be well-separated and that the division between short and long-duration GRBs detected by the BAT is less than 1s.
- In addition we identified a third group in the cluster analysis: XRFs
- The large number of *Swift*-detected bursts with redshift measurements allows to do preform GRB cosmology (sections 3.5, 4.5). The analysis of the GRB luminosity functions at different redshift intervals shows that the slope of the high-luminosity end of the luminosity function becomes steeper with increasing redshift. The density of high luminous GRBs $L > 10^{52}$ erg s⁻¹ rate peaks at a redshift of about $z=3$ and the results suggest a 'cosmic downsizing' of GRBs at lower redshifts, similar to what has been observed for quasars. The peak of this GRB density is at a redshift of 2.7 which agrees with the peak of the cosmic quasar density and the star formations rate history, suggesting a close connection GRBs - star formation and quasar evolution.
- The detection of a GRB is strongly depends on the BAT detection characteristics (Section 3.2). This is primarily a mixture of the length of the burst and the fluence. We can not detect very long bursts with low fluence.
- Observed BAT parameters can be used to get a rough estimate of a burst redshift.
- The statistical analysis presented in the paper can only be the beginning of data mining the rich *Swift* GRB data set. In the future we need to look into the analysis of the datasets including survival statistics to take upper and lower limits, e.g. for the break times in the X-ray light curves into account. Another important task in the future will be to develop a support vector machine analysis that will allow to make pre-

dictions on the X-ray afterglow light curve and its behavior based on prompt emission properties. Last but not least we need to examine the possibility of estimating redshift predictions similar to what has been done by Morgan et al. (2012). Ultimately it is important that ground-based observes increase the number of afterglows for which they obtain spectroscopic data to measure redshifts. Only with redshifts and therefore distance measurements we are able to derive the intrinsic physical properties of the bursts.

We would like to thank all observers at ground-based optical telescopes for their effort to obtain redshifts of the *Swift* afterglows. We would also like to thank the anonymous referee for detailed and supportive reports. We thank Raffaella Margutti for discussions on the PCA in her 2013 paper. This research has made use of the XRT Data Analysis Software (XRTDAS) developed under the responsibility of the ASI Science Data Center (ASDC), Italy. This research has made use of data obtained through the High Energy Astrophysics Science Archive Research Center Online Service, provided by the NASA/Goddard Space Flight Center. This work made use of data supplied by the UK Swift Science Data Centre at the University of Leicester. PV thanks NASA NNX13AH50G and OTKA K077795, and Peter Mészáros for discussions. At Penn State we acknowledge support from the NASA Swift program through contract NAS5-00136.

REFERENCES

- Abdo, A.A., et al., Nature, 462, 331
- Aharonian, F., et al., 2009, ApJ, 690, 1068
- Amati, L., et al., 2002, A&A, 390, 81
- Aptekar, R.L., et al., 1995, Space Sci. Rev., 71, 1, 265
- Arnaud, K. A., 1996, ASP Conf. Ser. 101: Astronomical Data Analysis Software and Systems V, 101, 17
- Atwood, W.B., et al., 2009, ApJ, 697, 1071
- Balázs, L. G., & Veres, P. 2011, Advances in Space Research, 47, 1404

- Band, D., et al., 1993, *ApJ*, 413, 281
- Barthelmy, S.D., Butterworth, P., Cline, T., Gehrels, N., Fishman, G.J., Kouveliotou, C., & Meegan, C.A., 1995, *Ap&SS*, 231, 235
- Barthelmy, S.D., 2005, *Space Science Reviews*, 120, 143
- Beloborodov, A. M. 2010, *MNRAS*, 407, 1033, 0907.0732
- Berger, E., Kulkarni, S.R., Fox, D.B., et al., 2005a, *ApJ*, 629, 328
- Berger, E., et al., 2005b, *GCN* 3368
- Berger, E., Price, P.A., & Fox, D.B., 2006a, *GCN* 4622
- Berger, E., Kulkarni, S.R., Rau, A., & Fox, D.B., 2006b, *GCN* 4815
- Berger, E., et al., 2007, *ApJ*, 664, 1000
- Berger, E., & Gladders, M., 2006, *GCN* 5170
- Berger, E., 2006, *GCN* 5962
- Bernardini, M. G., Margutti, R., Mao, J., Zaninoni, E., & Chincarini, G. 2012, *A&A*, 539, A3
- Bernardini, M.G., Margutti, R., Zaninoni, E., & Chincarini, G., 2012b, *MNRAS*, 425, 1199
- Blandford, R. D., & Znajek, R. L. 1977, *MNRAS*, 179, 433
- Bloom, J.S., Perley, D., Foley, R., Prochaska, J.X., Chen, H.W., & Starr, D., 2005, *GCN* 3758
- Bloom, J.S., Foley, R.J., Kocevski, D., & Perley, D., 2006a, *GCN* 5217
- Bloom, J.S., Perley, D., & Chen, H.W., 2006b, *GCN* 5826
- Boroson, T.A., 2002, *ApJ*, 565, 78
- Boroson, T.A., & Green, R.F., 1992, *ApJS*, 80, 109
- Bromberg, O., Nakar, E., Piran, T., & Sari, R, 2013, *ApJ*, 769, 179
- Burrows, D.N., et al., 2005, *Space Science Reviews*, 120, 165
- Burrows, D.N., et al., *ApJ*, 653, 458
- Campana, S., et al., 2006a, *A&A*, 449, 61
- Campana, S., et al., 2006b, *Nature*, 442, 1008
- Campisi, M.A., & Li, L-X., 2008, *MNRAS*, 391, 935
- Cao, X.-F., Yu, Y.-W., Cheng, K.S., & Zheng, X.-P, 2011, *MNRAS*, 416, 2174
- Castro-Tirado, A.J., Amado, P., Negueruela, I., Gorosabel, J., Jelínek, M., & A. de Ugarte Postigo, 2006, *GCN* 5218
- Cenko, S.B., et al., 2005, *GCN* 3542
- Cenko, S.B., Berger, E., Djorgovski, S.G., Mahabal, A.A., & Fox, D.B., 2006, *GCN* 5155
- Chen, H.-W., et al., 2005, *GCN* 3706
- Corsi, A., & Mészáros, P. 2009, *ApJ*, 702, 1171
- Costa, E., et al., 1999, *A&AS*, 138, 425
- Coward, D.M., Howell, E.J., Branchesi, M., Stratta, G, Guetta, D., Gendre, B., & Macpherson, D., 2013, *MNRAS*, 432, 2141
- Crawley, M.J., 2007, *The R Book*, Wiley & Sons
- Cucchiara, A., Fox, D.B., & Berger, E., 2006a, *GCN* 4729
- Cucchiara, A., Price, P.A., Fox, D.B., Cenko, S.B., & Schmidt, B.P., 2006b, *GCN* 5052
- Dai, Z. G., & Lu, T. 1998, *A&A*, 333, L87
- Dainotti, M.G., Cardone, V.F., & Capozziello, S, 2008, *MNRAS*, 391, 79
- Dall’Osso, S., Stratta, G., Guetta, D., Covino, S., De Cesare, G., & Stella, L. 2011, *A&A*, 526, A121
- D’Avanzo, P., et al., 2012, *MNRAS*, 425, 506
- De Pasquale, M., et al., 2006, *A&A*, 455, 813
- De Pasquale, M., et al., 2010, *ApJ*, 709, L146
- Dickey, J.M., & Lockman, F.J., 1990, *ARA&A*, 28, 215
- Drenkhahn, G., & Spruit, H. C. 2002, *A&A*, 391, 1141

- Eichler, D., & Granot, J. 2006, *ApJ*, 641, L5
- Evans, P.A., et al., 2007, *A&A*, 469, 379
- Evans, P.A., et al., 2009, *MNRAS*, 397, 1177
- Everitt, B.S., & Hothorn, T., 2010, “A Handbook of Statistical Analysis using R”, Chapman & Hall, Boca Raton, FL
- Everitt, B., Landau, S., Leese, M., & Stahl, D., 2011, “Cluster Analysis, 5th edition”, John Wiley & Sons, Ltd, Chichester, UK.
- Falcone, A.D., et al., 2007, *ApJ*, 671, 1921
- Feigelson, E.D., & Babu, G.j., 2012, “Modern Statistical Methods for Astronomy”, Cambridge University Press
- Fong W., et al., 2013, *ApJ*, 769, 56
- Frail, D.A., et al., 2001, *ApJ*, 562, L55
- Francis, P.J., & Wills, B.J., 1999, *ASP Conf. Series*, 162, 363
- Fynbo, J.P.U., et al., 2009, *ApJS*, 185, 526
- Gehrels, N., et al., 2004, *ApJ*, 611, 1005
- Gehrels, N., et al., *Nature*, 444, 1044
- Gehrels, N., et al., *ApJ*, 689, 1161
- Gehrels, N., & Cannizzo, J.K., 2012, proceedings of the “New windows on transients across the Universe issue” Discussion Meeting issue of *Philosophical Transactions A*, ed. P. O’Brien, S. Smartt, R. Wijers & K. Pounds
- Genet, F., Daigne, F., & Mochkovitch, R. 2007, *MNRAS*, 381, 732
- Ghirlanda, G., Ghisellini, G., & Lazzati, D., 2004, *ApJ*, 616, 331
- Ghisellini, G., Ghirlanda, G., Nava, L., & Firmani, C. 2007, *ApJ*, 658, L75
- Godet, O., et al., 2009, *A&A*, 494, 775
- Granot, J., & Kumar, P. 2006, *MNRAS*, 366, L13, arXiv:astro-ph/0511049
- Greiner, J., et al., *PASP*, 120, 405
- Grieco, V., Matteucci, F., Meynet, G., Longo, F., Della Valle, M., & Salvaterra, R., 2012, *MNRAS*, 432, 2141
- Grupe, D., 2004, *AJ*, 127, 1799
- Grupe, D., 2012, Proceedings of the Gamma-Ray Bursts 2012 Conference, Munich/Germany, PoS(GRB 2012)065
- Grupe, D., et al., 2006, *ApJ*, 645, 464
- Grupe, D., et al., 2007, *AJ*, 133, 2216
- Halpern, J.P., & Mirabal, N, 2006, *GCN* 5982
- Hill, J.E., et al., 2004, *SPIE*, 5165, 217
- Hopkins, A.M., & Beacom, J.F., 2006, *ApJ*, 651, 142
- Hullinger, D., et al., 2005, *GCN circ.* 4237
- Humason, M.L., Mayall, N.U., & Sandage, A., 1956, *AJ*, 61, 97
- Ioka, K., Toma, K., Yamazaki, R., & Nakamura, T. 2006, *A&A*, 458, 7
- Jakobsson, P., et al., 2012, *ApJ*, 752, 62
- Kalberla, P.M.W., et al., *A&A*, 440, 775
- Kovetski, D., 2012, *ApJ*, 747, 146
- Kouveliotou, C., Meegan, C.A., Fishman, G.J., Bhat, N.P., Briggs, M.S., Koshut, T.M., Paciesas, W.S., & Pendleton, G.N., 1993, *ApJ*, 413, L101
- Krühler, T., et al., 2011, *A&A*, 526, 153
- Krühler, T., et al., 2012, *ApJ*, 758, 46
- Kumar, P., & Piran, T., 2000, *ApJ*, 535, 152
- Kumar, P., Narayan, R., & Johnson, J. L. 2008, *Science*, 321, 376
- Liang, E.-W., Zhang, B.-B., & Zhang, B. 2007, *ApJ*, 670, 565
- Littlejohns, O., Tanvir, N., Willingale, R., O’Brien, P., Evans, P., & Levan, A., 2013, 7th Huntsville Gamma-Ray Burst Symposium, GRB 2013: paper 36 in eConf Proceedings C1304143

- Lü, H., Liang, E.-W., Zhang, B.B., & Zhang, B., 2010, *ApJ*, 725, 1965
- Lyons, N., O'Brien, P. T., Zhang, B., Willingale, R., Troja, E., & Starling, R. L. C. 2010, *MNRAS*, 402, 705
- Margutti, R., et al., 2011a, *MNRAS*, 410, 1064
- Margutti, R., et al., 2011b, *MNRAS*, 417, 2144
- Margutti, R., et al., 2013, *MNRAS*, 428, 729
- McKinney, J. C., & Uzdensky, D. A. 2012, *MNRAS*, 419, 573
- Meegan, C.A., et al., 2009, *ApJ*, 702, 791
- Mészáros, P., 2006, *Rep. Prog. Phys.* 69, 2259
- Mészáros, P., & Rees, M. J. 1997, *ApJ*, 476, 232,
- Metzger, B. D., Giannios, D., Thompson, T. A., Bucciantini, N., & Quataert, E. 2011, *MNRAS*, 413, 2031
- Morgan, A.N., Long, J., Richards, J.W., Broderick, T., Butler, N.R., & Bloom, J.S., 2012, *ApJ*, 746, 170
- Mukherjee, S., et al., 1998, *ApJ*, 508, 314
- Nava, L., et al., 2012, *MNRAS*, 421, 1256
- Norris, J.P./, Marani, G.F., & Bonnell, J.T., 2000, *ApJ*, 534, 248
- Nousek, J.A., et al., 2006, *ApJ*, 642, 389
- O'Brien, P.T., et al., 2006, *ApJ*, 647, 1213
- Oke, J.B., & Sandage, A., 1968, *ApJ*, 154, 21
- Palmer, D.M., et al., 2012, *GCN circ.* 13186
- Panaitescu, A., & Kumar, P. 2000, *ApJ*, 543, 66
- Pe'er, A., Mészáros, P., & Rees, M. J. 2006, *Astrophys.J.*, 642, 995
- Pearson, K., 1901, *Philosophical Magazine* 2 (6), 559
- Perley, D.A., Foley, R.J., Bloom, J.S., & Butler, N.R., 2005, *GCN circ.* 5387
- Qin, Y., et al., 2013, *ApJ*, 763, 15
- Racusin, J.L., et al., 2009, *ApJ*, 698, 43
- Racusin, J.L., et al., 2011, *ApJ*, 738, 138
- Rees, M. J., & Mészáros, P. 1998, *ApJ*, 496, L1
- Richards, G.T., et al., 2006, *AJ*, 131, 2766
- Rhoads, J. E. 1999, *ApJ*, 525, 737
- Roming, P.W.A., et al., 2005a, *Space Science Reviews*, 120, 95
- Roming, P.W.A., et al., 2006, *ApJ*, 652, 1416
- Ross, N.P., et al., 2012, *ApJ*, 773, 14
- Rowlinson, A., O'Brien, P. T., Metzger, B. D., Tanvir, N. R., & Levan, A. J. 2013, *MNRAS*, 430, 1061
- R Development Core Team (2009). *R: A language and environment for statistical computing*. R Foundation for Statistical Computing, Vienna, Austria. ISBN 3-900051-07-0, URL <http://www.R-project.org>.
- Sakamoto, T., et al., 2008, *ApJ*, 679, 570
- Sakamoto, T., et al., 2009, *ApJ*, 693, 922
- Salvaterra, R., Cerutti, A., Chincarini, G., Colpi, M., Guidorzi, C., & Romano, P., 2008, *MNRAS*, 388, L6
- Salvaterra, R., et al., 2012, *ApJ*, 749, 68
- Savaglio, S., Palazzi, E., Ferrero, P., & Klose, S., 2007, *GCN* 6166
- Schaefer, B.E., 2007, *ApJ*, 660, 16
- Schmidt, M., 2009, *ApJ*, 700, 633
- Soderberg, A.M., Berger, E., & Ofek, E., 2005, *GCN* 4186
- Soderberg, A.M., et al., 2006, *Nature*, 442, 1024.
- Still, M., et al., 2006, *GCN* 5226
- Stratta, G., Fiore, F., Antonelli, L.A., Piro, L., & De Pasquale, M., 2004, *ApJ*, 608, 846
- Stratta, G., Guetta, D., D'Elia, V.D., Perri, M., Corvino, S., & Stella, L., 2009, *A&A*, 494, L9
- Tagliaferri, G., et al., 2005, *GCN Circ.* 4222
- Tanvir, N.R., et al., 2012, *ApJ*, 754, 46

- Thoene, C.C., et al., 2006a, GCN 5373
- Thoene, C.C., Fynbo, J.P.U., Jakobsson, P., Vreeswijk, P.M., & Hjorth, J., 2006b, GCN 5812
- Thompson, C. 1994, MNRAS, 270, 480
- Toma, K., Ioka, K., Yamazaki, R., & Nakamura, T. 2006, ApJ, 640, L139
- Torgo, L., 2011, "Data Mining in R", Chapman & Hall/CRC
- Uhm, Z. L., & Beloborodov, A. M. 2007, ApJ, 665, L93
- Ukwitta, T., et al., 2010, ApJ, 711, 1073
- Ukwitta, T., et al., 2012, MNRAS, 419, 614
- Veres, P., Bagoly, Z., Horvath, I., Mészáros, A., & Balazs, L.G., 2010, ApJ, 725, 1955
- Wang, J.X., Malhatra, S., Rhoads, J.E., & Norman, C.A., 2004, ApJ, 612, L109
- Wanderman, D., & Piran, T., 2010, MNRAS, 406, 1944
- Watson, D., et al., ApJ, 652, 1011
- Willingale, R., et al., 2007, ApJ, 662, 1193
- Wright, E.L., 2006, PASP, 118, 1711
- Yonetoku, D., Murakami, T., Nakamura, T., Yamazaki, R., Inoue, A.K., & Ioka, K., 2004, ApJ, 609, 935
- Zalamea, I., & Beloborodov, A. M. 2011, MNRAS, 410, 2302
- Zhang, B., & Mészáros, P. 2001, ApJ, 552, L35
- Zhang, B., & Meszaros, P., 2004, Int. Jour. Mod. Phys. A, 19, 2385
- Zhang, B., et al., 2006, ApJ, 642, 354
- Zhang, B. 2007, Chinese Journal of Astronomy and Astrophysics, 7, 1
- Zhang, B., et al., 2009, ApJ, 703, 1696
- Zhang, B., 2012, Proceedings of the IAU Symposium 279, arXiv:1204.4919
- Zhang, B.-B., Liang, E.-W., & Zhang, B., 2007, ApJ, 666, 1002
- Zhang, B., & Yan, H. 2011, ApJ, 726, 90
- Zhang, B.-B., Zhang, B., Liang, E.-W., & Wang, X.-Y., 2009, ApJ, 690, L10

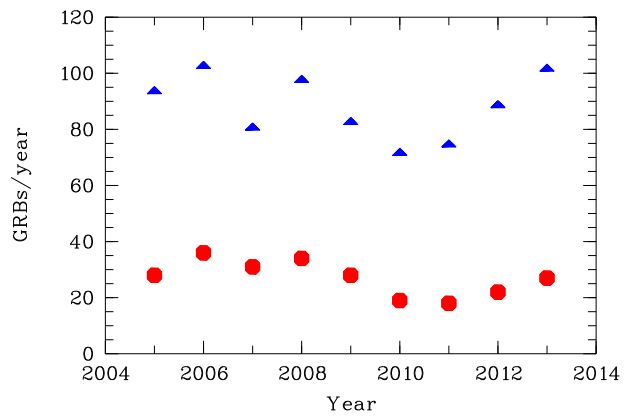


Fig. 1.— Onboard *Swift*-BAT-detected GRBs per year. The blue triangles displays all GRBs detected and the red circles those GRBs which had spectroscopic redshift measurements. Note that the 2013 numbers were projected based on the GRBs detected in the first 8 months of 2013.

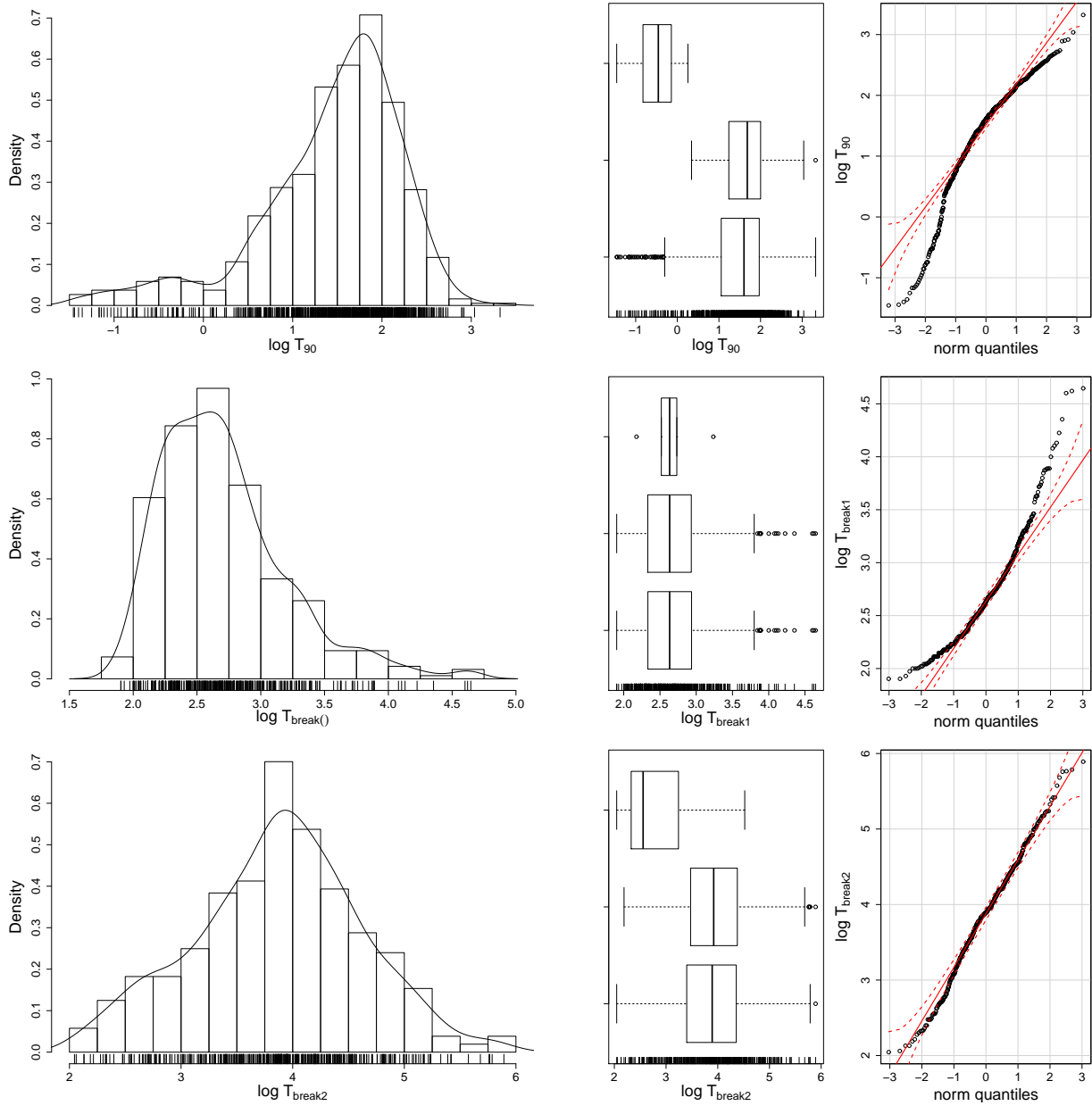


Fig. 2.— Histograms, box plots and qq plots of the distributions of the 15-150 keV BAT T_{90} (upper panels), the X-ray afterglow light curve break times T_{break1} (middle panel) and T_{break2} (lower panels) before and after the plateau phase, respectively in the observed frame. The solid line in the histogram displays the kernel density estimator (e.g. Everitt & Hothorn 2010; Feigelson & Babu 2012). In the box plots, short bursts are displayed on top, long bursts in the middle and all bursts on the bottom.

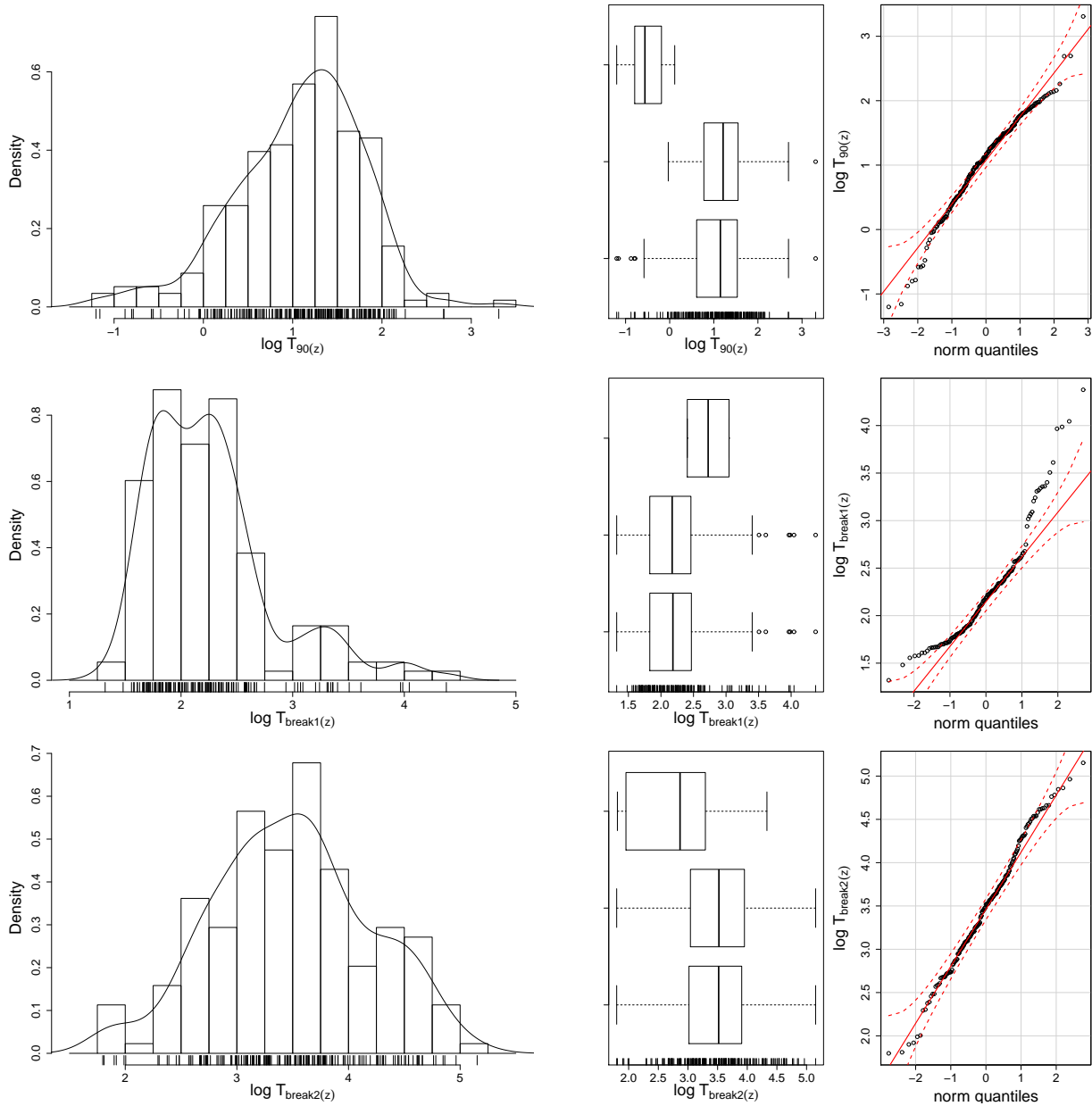


Fig. 3.— Same as Figure 2, but all times in the rest-frame.

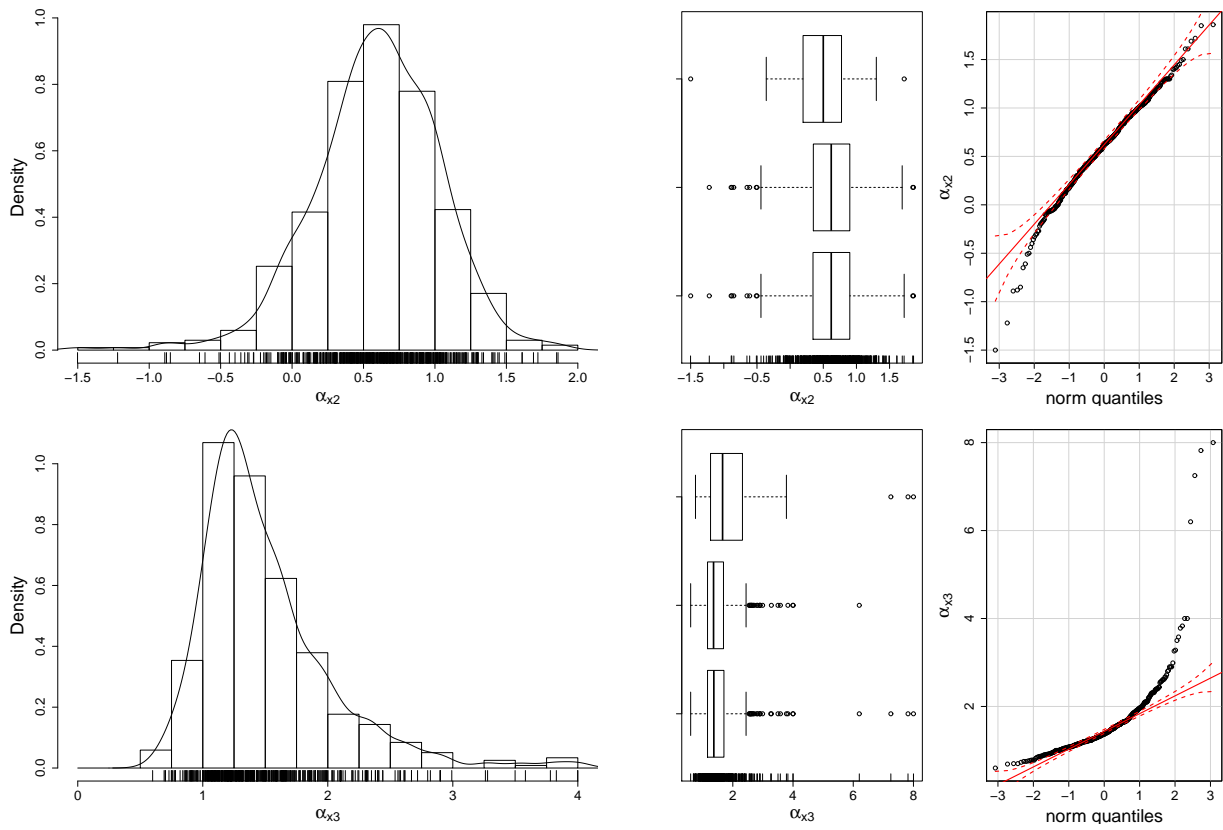


Fig. 4.— Distributions of the X-ray light curve decay slopes during the plateau and the normal decay phase (upper and panel panel, respectively). As in Figure 2, the histogram, box plot, and q-q plot are shown. In the box plots, short bursts are displayed on top, long bursts in the middle and all bursts on the bottom.

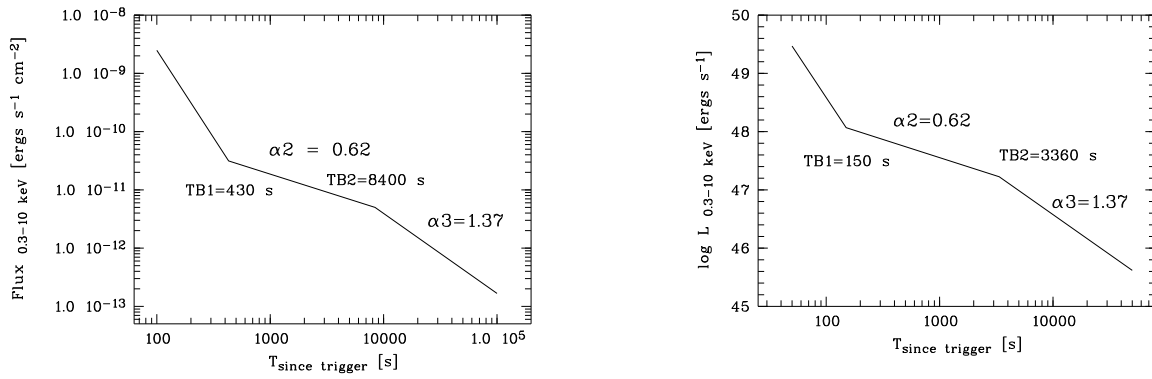


Fig. 5.— Median observed XRT flux light curve and rest-frame luminosity light curve of *Swift*-detected GRBs (left and right panel, respectively, see also Table 1).

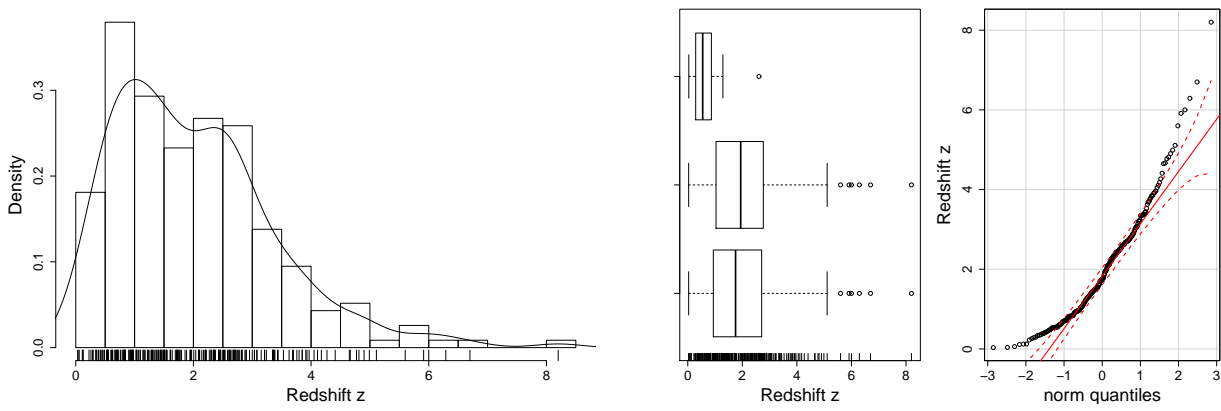


Fig. 6.— Redshift distribution of all *Swift*-detected GRBs with spectroscopic redshifts. As in Figure 2, the histogram, box plot, and q-q plot are shown. In the box plots, short bursts are displayed on top, long bursts in the middle and all bursts on the bottom.

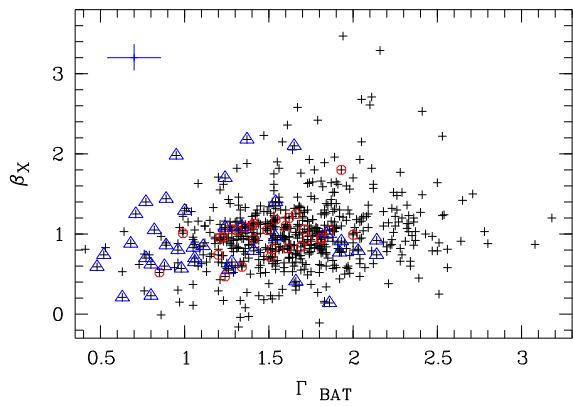


Fig. 11.— Correlation between 15-150 keV photon spectra slope Γ in the BAT and the 0.3-10 keV energy spectral index β_X . Of this plot is the extremely soft GRB 060602B (Aharonian et al. 2009) at $\Gamma = 4.97 \pm 0.49$ and $\beta_X = 3.30 \pm 0.91$. The blue cross in the upper left corner displays the median uncertainty of each property.

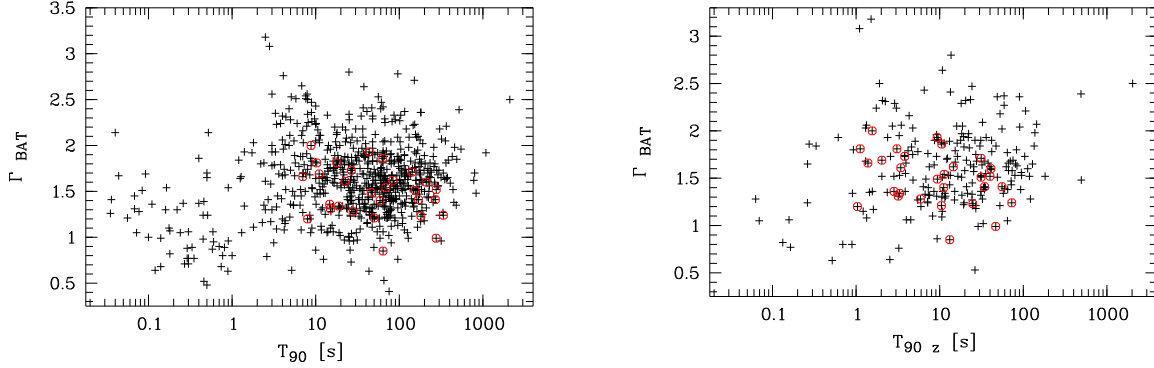


Fig. 7.— Correlations between the BAT 15-150 keV photon index Γ and the observed and rest-frame T_{90} . High redshift bursts ($z > 3.5$) are displayed as red circles.

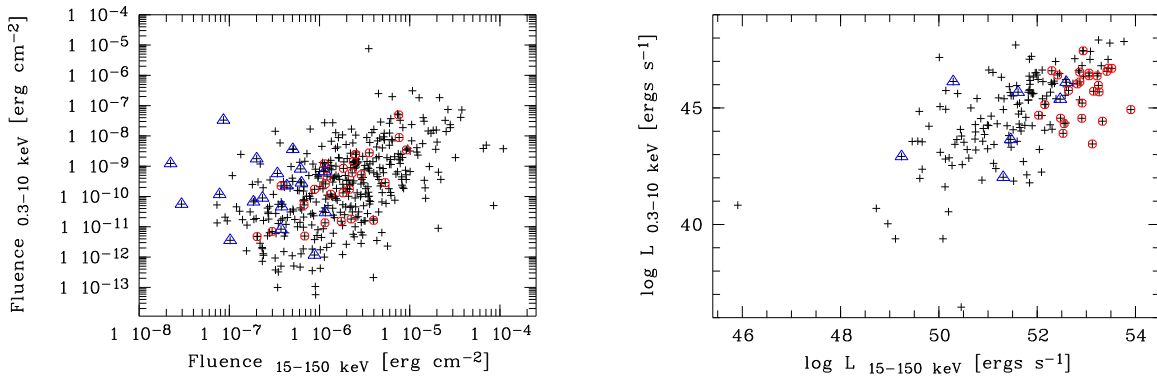


Fig. 8.— Correlations between the fluences and the luminosities in the 15-150 keV BAT band and the 0.3-10 keV XRT energy band (left and right panel, respectively). Short bursts are marked as blue triangles and high redshift bursts ($z > 3.5$) as red circles.

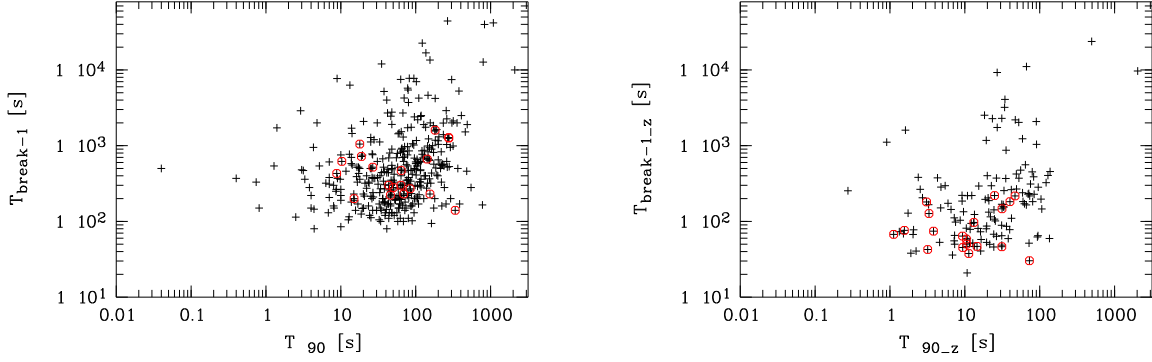


Fig. 9.— Correlation between the observed BAT 15-150 keV T_{90} and the break time $T_{\text{break}1}$ in the X-ray afterglow light curves before the plateau phase in the observed and rest-frame (left and right panel, respectively). GRBs with a redshift $z > 3.5$ are marked as red circles.

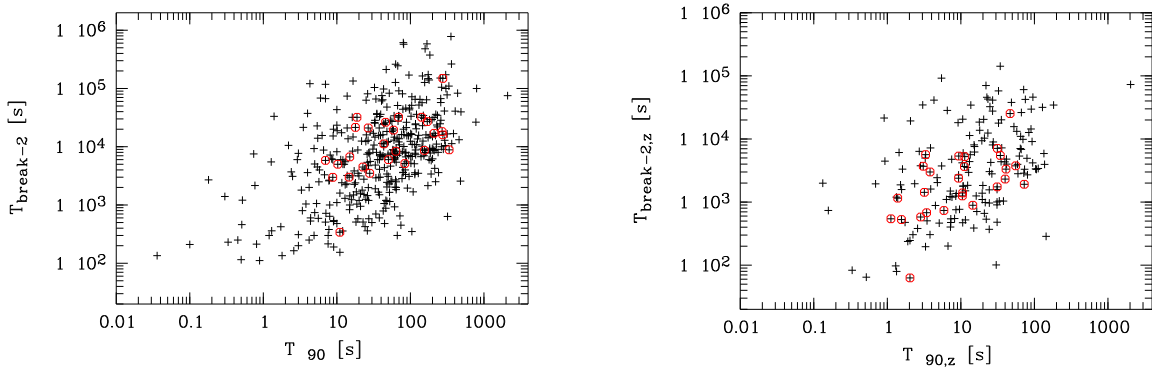


Fig. 10.— Correlation between the observed BAT 15-150 keV T_{90} and the break time $T_{\text{break}2}$ in the X-ray afterglow light curves after the plateau phase in the observed and rest-frame (left and right panel, respectively).

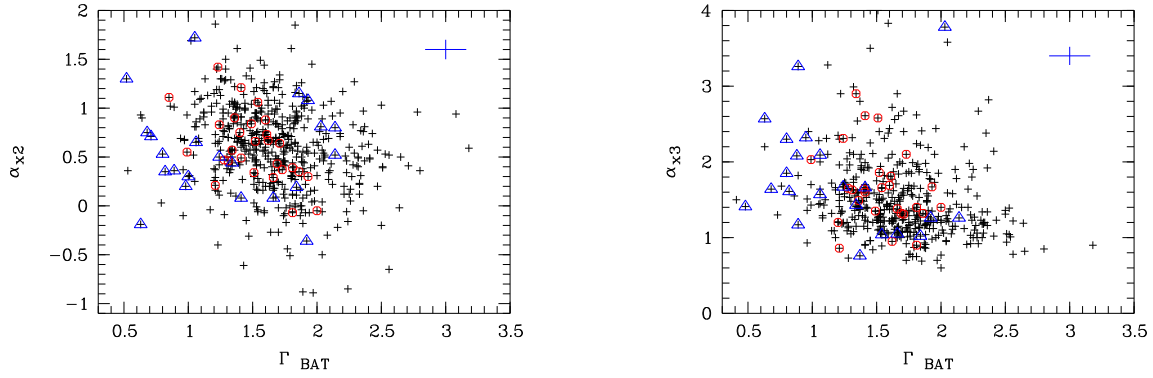


Fig. 12.— Correlation between the BAT 15-150 keV photon index Γ_{BAT} and the decay slopes during the plateau phase and the ‘normal’ decay phase. (left and right panel, respectively). Short duration GRBs are displayed as triangles. The blue cross in the upper right corner displays the median uncertainty of each property.

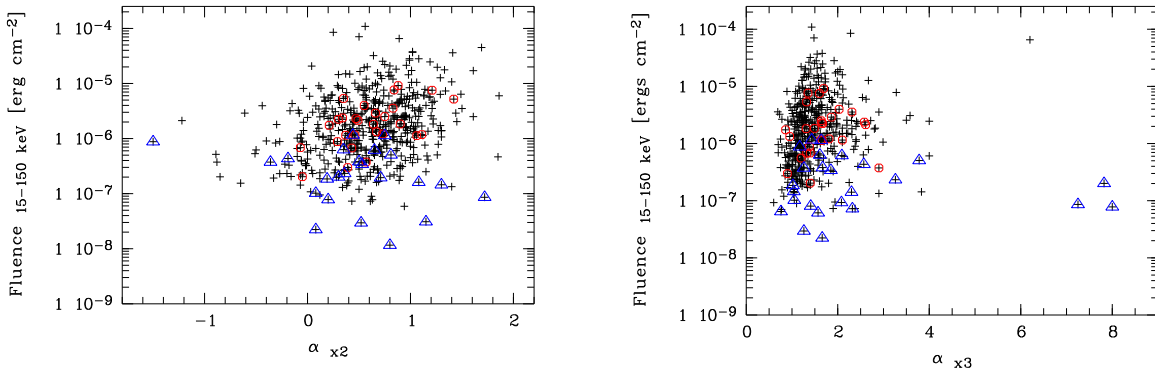


Fig. 13.— Correlation between the fluence in the 15-150 keV BAT and and the decay slopes during the plateau phase and the ‘normal’ decay phase. (left and right panel, respectively). Short duration GRBs are displayed as triangles.

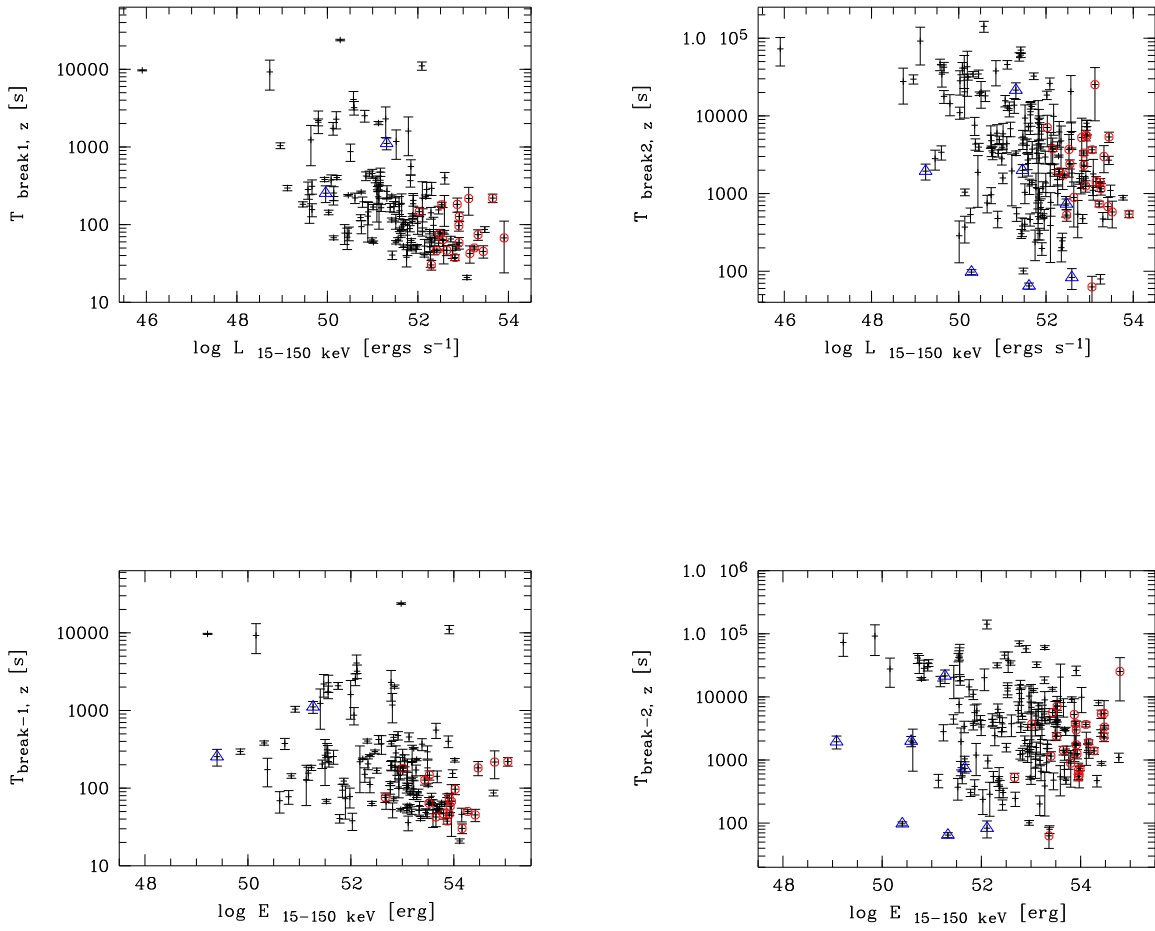


Fig. 14.— Relation between the k-corrected BAT luminosity and the BAT photon index Γ and the break times before and after the X-ray afterglow plateau phase (left and right panel, respectively). Short bursts in these plots are marked as triangles.

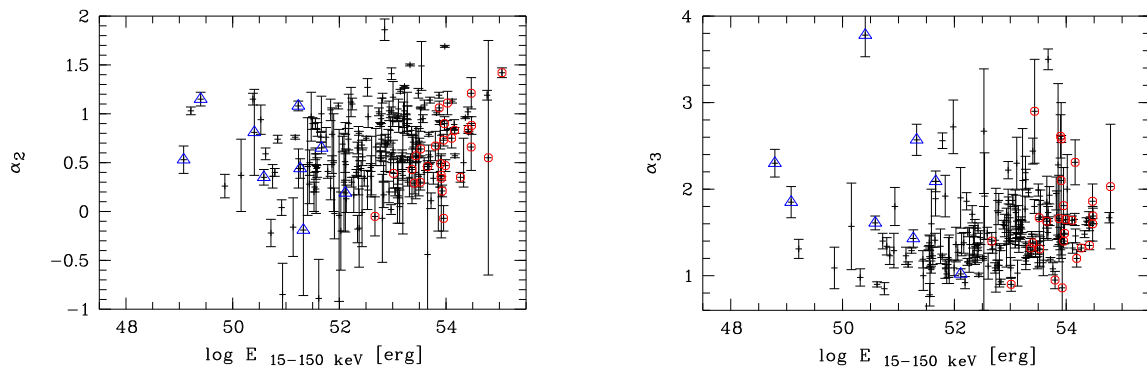


Fig. 15.— Correlation between the 15-150 keV isotropic energy and X-ray afterglow decay slopes during and after the plateau phase α_{X2} and α_{X3} . Short bursts in these plots are marked as triangles.

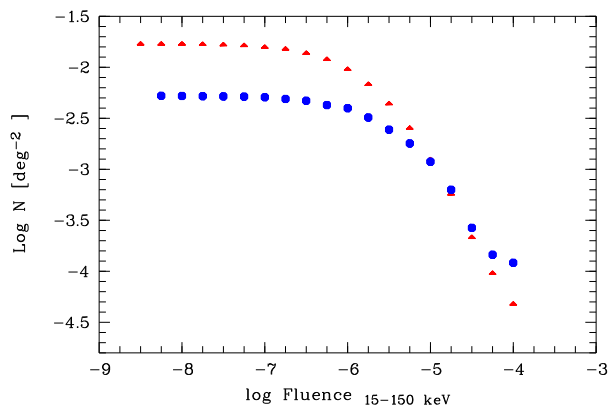


Fig. 17.— Log N - Log S Diagram of *Swift*-detected GRBs. The red triangles the observed fluence in the 15-150 keV BAT band and the blue squares the k-corrected 15-150 keV fluence.

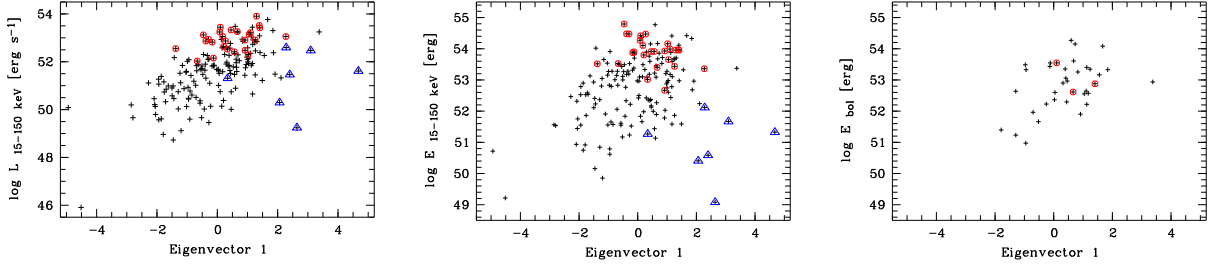


Fig. 16.— Eigenvector 1 vs. rest-frame 15-150 keV luminosity and isotropic energy in the 15-150 keV BAT band in our GRB sample (left and middle panel respectively). Eigenvector 1 was determined based on the 5 parameters used in the PCA listed in Table 5. The right panel displays eigenvector 1 vs. the bolometric energy derived by Nava et al. (2012) as a comparison.

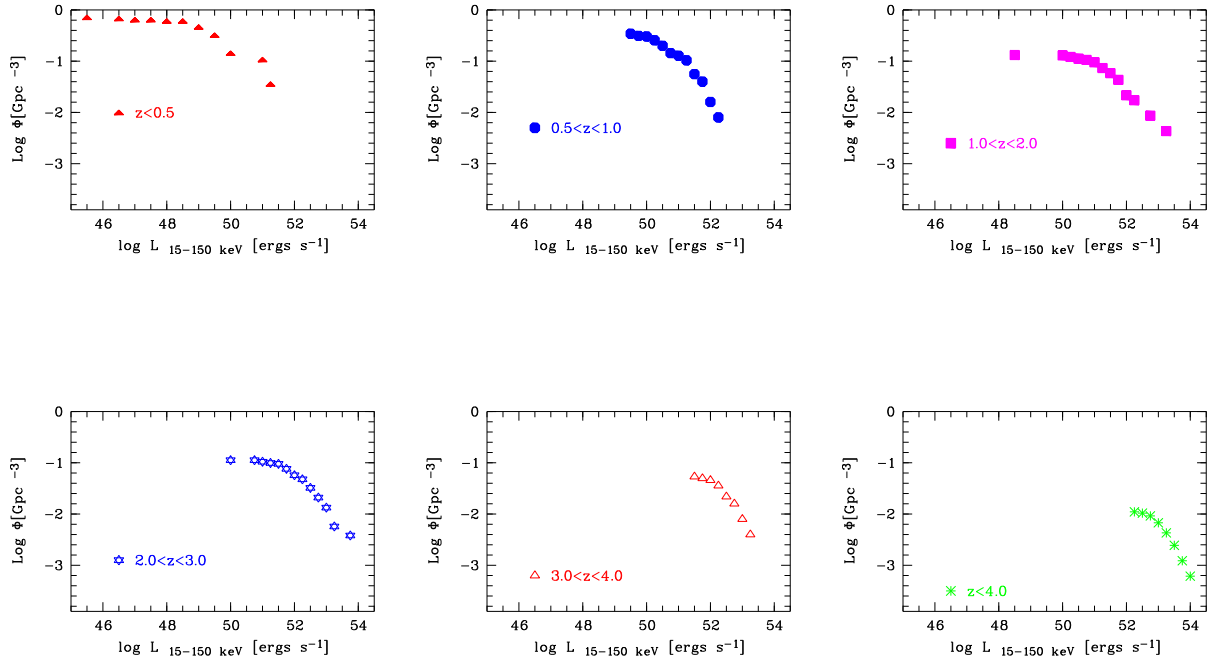


Fig. 18.— Luminosity function of *Swift*-discovered GRBs in various redshift intervals. The fit parameters to these luminosity functions and the number of GRBs in each function are listed in Table 6.

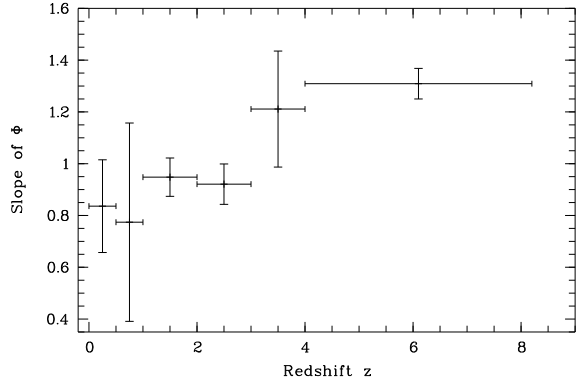


Fig. 19.— Slope b of the luminosity function (see Table 6) for bursts with $L > L_{\text{break}}$ vs. redshift.

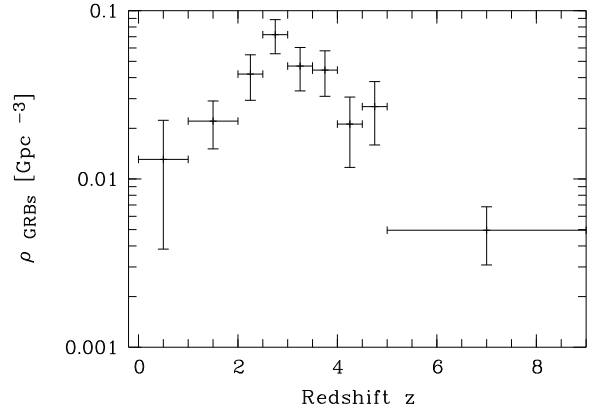


Fig. 21.— Density of bright ($L > 10^{52}$ erg s^{-1}) *Swift*-discovered bursts.

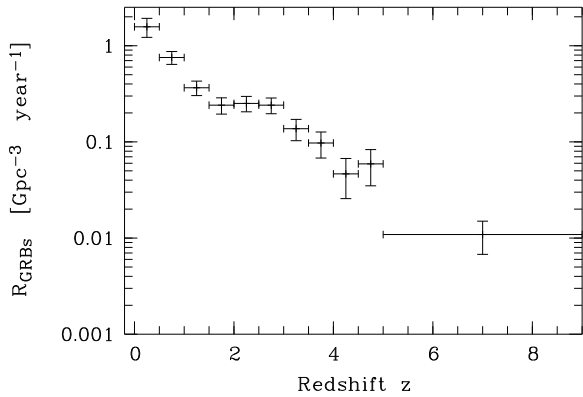


Fig. 20.— Total rate of GRBs per year and Gpc derived from the number of *Swift*-detected GRBs

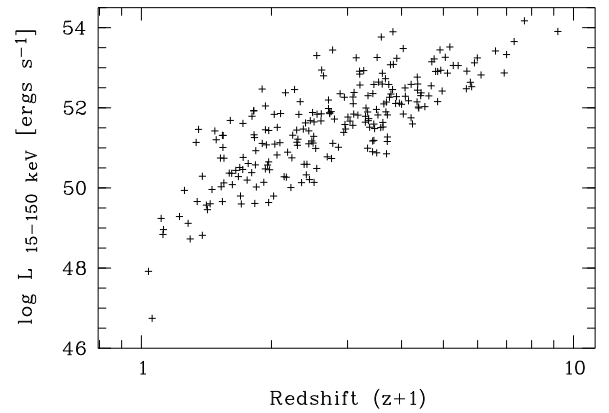


Fig. 22.— 15-150 keV luminosity vs. redshift

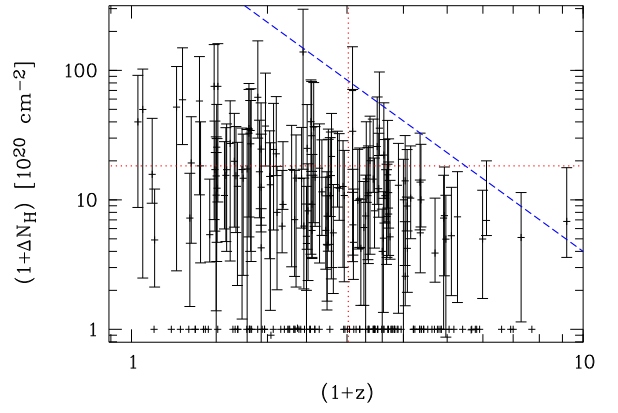


Fig. 23.— Excess absorption column density ($\Delta_{\text{NH}} + 1$) vs. redshift ($z+1$). The red lines mark the mean values as listed in Table 1 and the blue line the N_{H} - redshift relation from Grupe et al. (2007).

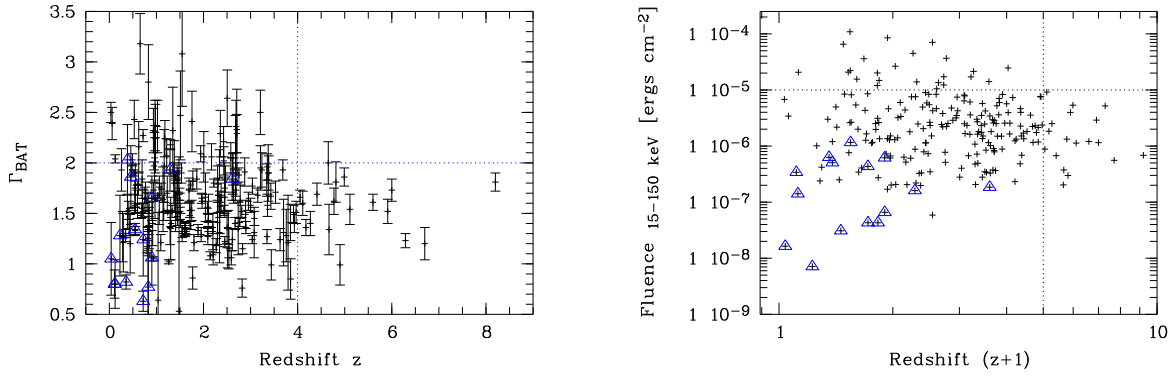


Fig. 24.— Relation between redshift and the photon index Γ in the BAT band and the observed 15-150 keV fluence. Again, short duration GRBs are marked as triangles.

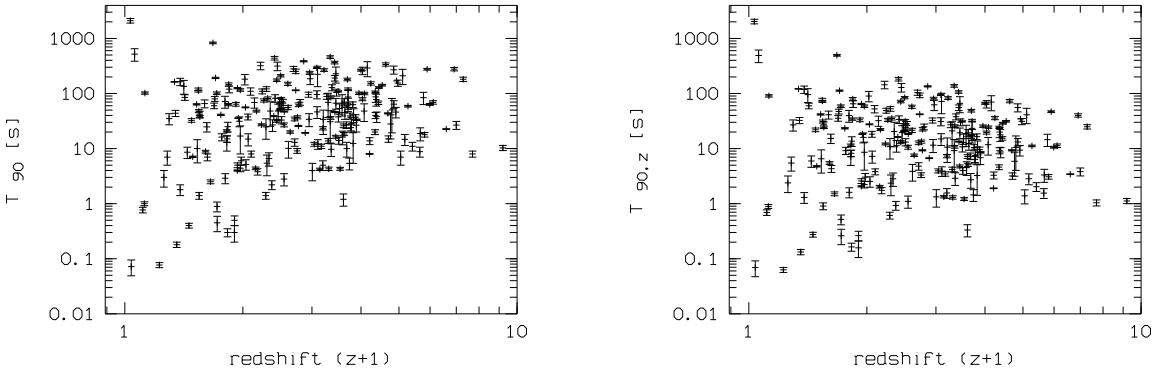


Fig. 27.— Relation between redshift and the observed and rest-frame BAT 15-150 keV T_{90} .

TABLE 1

MEAN, STANDARD DEVIATION, AND MEDIAN OF GRB PROPERTIES IN THE OBSERVED AND REST-FRAME FOR ALL GRBS, LONG AND SHORT DURATION GRBS, AND HIGH-REDSHIFT BURSTS ($z > 4.0$).

Property	All GRBS				Long GRBs				Short GRBs				z > 4 bursts			
	Mean	SD ¹	Median	# of GRBs	Mean	SD ¹	Median	# of GRBs	Mean	SD ¹	Median	# of GRBs				
Γ_{BAT}	1.614	0.420	1.600	751	1.651	0.400	1.620	687	1.205	0.418	1.100	63	1.554	0.260	1.600	18
β_{X}	1.002	0.432	0.970	632	1.007	0.429	0.970	592	0.934	0.478	0.830	39	0.974	0.171	0.960	18
$\log T_{90}$	1.435	0.798	1.601	753	1.612	0.550	1.681	690	-0.501	0.465	-0.456	63	1.557	0.554	1.354	18
$\log T_{90-z}$	1.074	0.706	1.129	232	1.184	0.580	1.208	217	-0.511	0.404	-0.561	15	0.770	0.561	0.535	18
$\log T_{\text{break}-1}$	2.706	0.493	2.638	384	2.705	0.494	2.633	377	2.655	0.347	2.568	6	2.792	0.294	2.000	11
$\log T_{\text{break}-1-z}$	2.258	0.564	2.190	146	2.252	0.564	2.178	144	2.725	0.453	2.725	2	1.984	0.285	1.881	11
$\log T_{\text{break}-2}$	3.866	0.748	3.897	417	3.917	0.712	3.924	389	2.802	0.704	2.556	19	3.987	0.597	4.080	16
$\log T_{\text{break}-2-z}$	3.484	0.697	3.365	177	3.512	0.674	3.522	170	2.786	0.935	2.867	7	3.201	0.615	3.255	16
$\alpha_{\text{X}2}$	0.592	0.439	0.620	539	0.597	0.427	0.630	515	0.455	0.639	0.500	23	0.582	0.375	0.660	17
$\alpha_{\text{X}3}$	1.550	0.748	1.380	475	1.499	0.555	1.370	450	2.475	2.088	1.660	25	1.591	0.476	1.490	17
$\log \text{fluence}^2$	-5.919	0.676	-5.907	752	-5.813	0.585	-5.848	689	-7.080	0.499	-7.134	63	-5.880	0.460	-5.930	18
$\log \text{fluence-k}^3$	-5.560	0.749	-5.536	232	-5.477	0.679	-5.491	217	-6.761	0.687	-6.768	15	-5.528	0.568	-5.586	18
$\log L_{15-150\text{keV}}^4$	51.540	1.240	51.678	231	51.603	1.210	51.759	216	50.637	1.350	51.111	15	53.158	0.459	53.090	18
$\log E_{\text{iso}}^5$	52.610	1.272	52.856	231	52.782	1.064	52.965	216	50.126	1.458	50.472	15	53.928	0.600	53.953	18
E_{peak}^6	254.1	376.0	148.0	206	225.3	246.4	143.0	193	686.4	1108	370	13	154.4	96.5	122.5	8
$E_{\text{peak},z}^6$	750.6	5	893.2	104	669.2	532.5	537.4	98	2008	2947	933	6	966.4	570.2	824.0	8
$\log (\Delta_{\text{NH}} + 1)^7$	0.606	0.715	0.000	618	0.626	0.715	0.000	578	0.377	0.698	0.000	39	0.259	0.380	0.000	18
z	2.018	1.373	1.763	232	2.111	1.363	1.950	217	0.681	0.640	0.547	15	5.201	1.080	4.860	18

¹Standard deviation SD

²Observer Fluence in the 15-150 keV BAT energy band in units of erg cm^{-2}

³K-corrected 15-150 keV Fluence in units of erg cm^{-2}

⁴rest frame 15-150 keV luminosity given in unites of erg s^{-1}

⁵k-corrected isotropic energy E_{iso} in the 15 - 150 keV BAT band

⁶Peak energy E_{peak} in units of keV

⁷The excess absorption column density Δ_{NH} above the galactic value (see Grupe et al. 2007) is given in units of 10^{20} cm^{-2}

TABLE 2
 SPEARMAN RANK ORDER CORRELATION AND STUDENT'S T-TEST FOR THE OBSERVED PARAMETERS OF
 ALL *Swift*-DETECTED GRBS. ¹

	Γ_{BAT}	β_{X}	α_{X2}	α_{X3}	T_{90}	T_{break1}	T_{break2}	15-150 keV fluence
Γ_{BAT}	—	632, 6.23×10^{-6}	$539, < 10^{-8}$	$475, < 10^{-8}$	750, 0.0231	384, 0.1638	417, 0.0162	$750, 1.85 \times 10^{-4}$
β_{X}	+0.186, +4.557	—	$539, 4.55 \times 10^{-4}$	$473, 2.71 \times 10^{-4}$	631, 0.4148	384, 0.1459	$417, 9.33 \times 10^{-4}$	631, 0.7742
α_{X2}	-0.259, -6.215	-0.150, -3.528	—	$413, < 10^{-8}$	$538, .7.2 \times 10^{-7}$	383, 0.4634	$414, 1.7 \times 10^{-7}$	$538, < 10^{-8}$
α_{X3}	-0.313, -7.181	-0.167, -3.669	+0.405, +8.980	—	$475, 1 \times 10^{-8}$	278, 0.0387	$414, 1.97 \times 10^{-6}$	$475, 5.6 \times 10^{-7}$
T_{90}	+0.083, +2.279	+0.033, +0.816	+0.212, +5.015	+0.262, +5.903	—	$383, < 10^{-8}$	$417, < 10^{-8}$	$752, < 10^{-8}$
T_{break1}	+0.071, +1.395	-0.074, -1.457	-0.038, -0.734	+0.124, +2.077	+0.328, +6.776	—	$277, < 10^{-8}$	383, 0.2121
T_{break2}	+0.118, +2.414	+0.161, +3.334	+0.254, +5.321	+0.231, +4.825	+0.495, 11.615	+0.516, +9.994	—	$417, 7.49 \times 10^{-5}$
15-150 keV fluence	-0.136, -3.758	+0.011, +0.286	+0.268, +6.450	+0.227, +5.075	+0.659, +23.99	-0.064, -1.253	+0.193, +3.999	—

¹The values below the diagonal list the Spearman rank order correlation coefficient r_s and the Student's T-test value T_s . The values above the diagonal list the number of GRBs in this correlation and the probability P that the result is drawn from a random distribution.

TABLE 3

SPEARMAN RANK ORDER CORRELATION AND STUDENT'S T-TEST FOR THE REST-FRAME PARAMETERS OF
Swift-DETECTED GRBs WITH SPECTROSCOPIC REDSHIFTS. ¹

	Γ_{BAT}	β_{X}	$\alpha_{\text{X}2}$	$\alpha_{\text{X}3}$	$T_{90,z}$	$T_{\text{break}1,z}$	$T_{\text{break}2,z}$	$L_{15-150\text{keV}}$	E_{iso}	$E_{\text{peak},z}$
Γ_{BAT}	—	$230, 1.68 \times 10^{-3}$	$208, 6.95 \times 10^{-5}$	$188, 1.68 \times 10^{-4}$	232, 0.1360	144, 0.1991	175, 0.047	$231, < 10^{-8}$	$231, 4 \times 10^{-8}$	$104, 1.12 \times 10^{-8}$
β_{X}	+0.206, +3.179	—	208, 0.011	$188, 2.75 \times 10^{-4}$	230, 0.2813	144, 0.2133	$175, 4.61 \times 10^{-4}$	229, 0.0500	229, 0.0701	103, 0.12
$\alpha_{\text{X}2}$	-0.272, -4.064	-0.175, -2.556	—	$175, 1.96 \times 10^{-5}$	208, 0.0197	143, 0.4256	175, 0.1557,	207, 0.0702	$207, 1.22 \times 10^{-3}$	$98, 4.12 \times 10^{-3}$
$\alpha_{\text{X}3}$	-0.271, -3.839	-0.262, -3.708	+0.317, +4.393	—	$188, 9.06 \times 10^{-3}$	115, 0.2404	174, 0.5166	188, 0.0225	$188, 2.98 \times 10^{-5}$	87, 0.01
$T_{90,z}$	+0.098, +1.496	+0.072, +1.082	+0.162, +2.351	+0.190, +2.637	—	$144, 4.53 \times 10^{-6}$	$175, < 10^{-8}$	$231, 7.64 \times 10^{-6}$	$231, 2.64 \times 10^{-3}$	104, 0.7
$T_{\text{break}1,z}$	+0.108, +1.291	+0.104, +1.246	-0.067, -0.799	-0.111, -1.183	+0.371, +4.767	—	$115, < 10^{-8}$	$143, < 10^{-8}$	$143, < 10^{-8}$	65, 0.28
$T_{\text{break}2,z}$	+0.151, +2.004	+0.262, +3.573	+0.108, +1.425	+0.050, +0.651	+0.439, +6.421	+0.628, +8.568	—	$175, 1 \times 10^{-8}$	175, 0.0110	82, 0.16
$L_{15-150\text{keV}}$	-0.370, -6.032	-0.130, -1.972	+0.126, +1.816	+0.166, +2.295	-0.290, -4.579	-0.587, -8.614	-0.413, -5.956	—	$231, < 10^{-8}$	$103, 6.88 \times 10^{-8}$
E_{iso}	-0.351, -5.678	-0.120, -1.815	+0.222, +3.264	+0.300, +4.284	+0.197, +3.048	-0.472, -6.357	-0.192, =2.570	+0.850, +24.415	—	$103, 1.06 \times 10^{-8}$
$E_{\text{peak},z}$	-0.416, -4.616	-0.141, -1.433	+0.287, +2.938	+0.268, +2.560	-0.031, -0.309	-0.136, -1.086	-0.155, -1.405	+0.426, +4.735	+0.459, +5.188	—

¹The values below the diagonal list the Spearman rank order correlation coefficient r_s and the Student's T-test value T_s . The values above the diagonal list the number of GRBs in this correlation and the probability that the result is drawn from a random distribution.

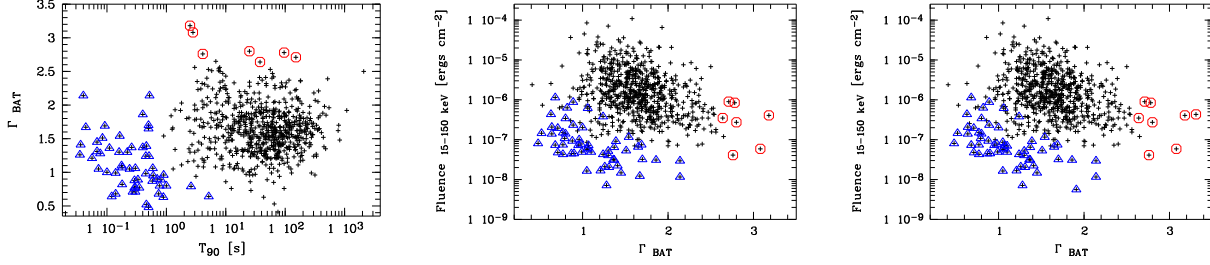


Fig. 29.— The correlations between the three parameters used in the cluster analysis as discussed in Section 4.4. The members of group 1 (long GRBs) from the cluster analysis are displayed as black crosses, group 2 (short GRBs) are displayed as (blue) triangles, and group 3 (XRFs) as red circles.

TABLE 4

RESULTS FROM THE PRINCIPAL COMPONENT ANALYSIS FOR 175 GRBs OF THE *Swift* SAMPLE¹.

Property	EV 1	EV 2	EV 3	EV 4	EV 5	EV 6
Proportion of Variance	0.3742	0.2366	0.1316	0.1007	0.08319	0.07377
Cumulative Proportion	0.3742	0.6108	0.7423	0.8430	0.92623	1.00000
$\log T_{90,z}$	-0.3959	0.4782	-0.2098	0.2080	0.7193	-0.0997
$\log T_{\text{break}2,z}$	-0.4859	0.2924	0.2970	0.1528	-0.4977	-0.5650
α_{X2}	0.1043	0.6931	-0.0393	-0.6379	-0.1961	0.2486
Γ_{BAT}	-0.3830	-0.3865	-0.5170	-0.5799	0.0193	-0.3163
β_X	-0.4105	-0.2349	0.7128	-0.3458	0.2755	0.2698
$\log L_{15-150\text{keV}}$	0.5303	0.0277	0.3016	-0.2658	0.3468	-0.6605

¹These are GRBs with canonical light curves and spectroscopic redshift measurements.

TABLE 5

SAME AS TABLE 4, BUT WITHOUT THE 15-150 KEV LUMINOSITY.

Property	EV 1	EV 2	EV 3	EV 4	EV 5
Proportion of Variance	0.3525	0.2836	0.1497	0.1172	0.09717
Cumulative Proportion	0.3525	0.6360	0.7857	0.9028	1.00000
$\log T_{90,z}$	-0.4680	0.4521	-0.3117	0.4303	-0.5424
$\log T_{\text{break}2,z}$	-0.5854	0.2565	0.2216	0.1604	0.7188
α_{X2}	0.0790	0.6985	-0.0738	-0.7073	-0.0044
Γ_{BAT}	-0.4048	-0.4096	-0.7159	-0.3758	0.1210
β_X	-0.5179	-0.2719	0.5795	-0.3842	-0.4176

TABLE 6
RESULTS OF THE FITS TO THE GRB LUMINOSITY FUNCTIONS SHOWN IN FIGURE 18

redshift interval	# of GRBs	a ¹	b ¹	Φ* ^{1,2}	L _{break} ^{1,3}
<0.5	21	+0.117±0.016	0.836±0.179	0.630±0.074	3.36 ± 1.27 × 10 ⁴⁹
0.5 - 1.0	44	-0.036±0.166	0.774±0.183	0.433±0.195	(2.81 ± 349) × 10 ⁵⁰
1.0 - 2.0	61	-0.001±0.011	0.948±0.074	0.133±0.008	(2.35 ± 0.36) × 10 ⁵¹
2.0 - 3.0	59	-0.024±0.023	0.921±0.078	0.127±0.011	(9.21 ± 2.13) × 10 ⁵¹
3.0 - 4.0	27	-0.090±0.149	1.211±0.224	0.068±0.019	(1.85 ± 0.95) × 10 ⁵²
>4.0	18	-0.107±0.040	1.309±0.059	0.014±0.001	(9.11 ± 1.07) × 10 ⁵²

¹The fit parameters are defined as $\Phi(L, z) = \frac{\Phi^*(L_{\text{break}})}{(L/L_{\text{break}})^a + (L/L_{\text{break}})^b}$

²The GRB density Φ* at the break luminosity L_{break} is given in units of GRBs per Gpc³.

³The break luminosity is given in units of erg s⁻¹

TABLE 7
MEAN, STANDARD DEVIATION, AND MEDIAN OF OBSERVED GRB PROPERTIES OF GRBs WITH SPECTROSCOPIC REDSHIFTS AND THOSE WITHOUT

Property	Mean	GRBs with redshift			Mean	GRBs without redshift			GRBs in PCA			
		SD ¹	Median	# of GRBs		SD ¹	Median	# of GRBs				
Γ _{BAT}	1.618	0.421	1.590	232	1.612	0.420	1.600	519	1.647	0.397	1.620	175
β _X	1.032	0.366	1.020	230	0.985	0.465	0.930	402	1.040	0.319	1.040	175
log T ₉₀	1.511	0.730	1.630	232	1.401	0.825	1.595	521	1.577	0.652	1.653	175
log T _{break-1}	2.710	0.507	2.607	145	2.703	0.485	2.645	239	2.658	0.471	2.568	115
log T _{break-2}	3.941	0.678	3.924	176	3.820	0.793	3.887	241	3.932	0.675	3.924	175
α _{X2}	0.620	0.419	0.590	208	0.575	0.451	0.620	331	0.556	0.392	0.550	175
α _{X3}	1.559	0.567	1.430	188	1.545	0.847	1.320	287	1.527	0.445	1.430	174
log fluence ²	-5.729	0.671	-5.716	232	-6.004	0.662	-5.975	520	-5.656	0.568	-5.636	175
E _{peak} ³	285.1	442.8	195.0	104	223.1	291.8	110.5	102	296.0	488.6	187.5	82
z	2.019	1.373	1.763	232	0	2.115	1.369	1.884	175
# of UVOT detections ⁴			155				91				123	

¹Standard deviation SD

²Observer Fluence in the 15-150 keV BAT energy band in units of erg s⁻¹ cm⁻²

³Peak energy E_{peak} in units of keV

⁴Of all GRBs, 218 had UVOT detections

TABLE 8
MEAN, STANDARD DEVIATION, AND MEDIAN OF GRB PROPERTIES IN THE OBSERVED FOR LOW ($z < 1.0$),
INTERMEDIATE ($1.0 < z < 3.5$), AND HIGH ($z > 3.5$) LONG-DURATION GRBs (GROUP 1 IN THE CLUSTER
ANALYSIS)

Property	Mean	SD ¹	z < 1.0		1.0 < z < 3.5			z > 3.5 bursts				
			Median	# of GRBs	Mean	SD ¹	Median	# of GRBs	Mean	SD ¹	Median	# of GRBs
Γ_{BAT}	1.693	0.425	1.630	50	1.635	0.401	1.620	136	1.494	0.274	1.510	29
β_{X}	1.105	0.483	1.035	50	1.023	0.307	1.020	136	0.974	0.250	0.990	29
$\log T_{90}$	1.455	0.662	1.552	50	1.652	0.530	1.681	136	1.689	0.531	1.702	29
$\log T_{\text{break}-1}$	2.867	0.638	2.681	31	2.667	0.471	2.565	90	2.646	0.310	2.633	19
$\log T_{\text{break}-2}$	4.017	0.761	3.959	39	3.923	0.645	3.924	103	4.018	0.513	4.002	26
$\alpha_{\text{X}2}$	0.579	0.421	0.570	44	0.639	0.431	0.630	125	0.600	0.352	0.560	28
$\alpha_{\text{X}3}$	1.469	0.528	1.340	41	1.517	0.394	1.440	112	1.652	0.509	1.630	27
$\log \text{fluence}^2$	-5.632	0.695	-5.703	50	-5.674	0.556	-5.632	136	-5.775	0.418	-5.740	29
E_{peak}^6	2.214	0.430	2.210	23	2.275	0.328	2.301	61	2.078	0.250	2.081	12
$\log (\Delta_{\text{NH}} + 1)^7$	0.931	0.711	1.167	49	0.585	0.574	0.709	136	0.265	0.377	0.000	29

¹Standard deviation SD

²Observer Fluence in the 15-150 keV BAT energy band in units of erg cm^{-2}

³K-corrected 15-150 keV Fluence in units of erg cm^{-2}

⁴rest frame 15-150 keV luminosity given in unites of erg s^{-1}

⁵k-corrected isotropic energy E_{iso} in the 15 - 150 keV BAT band

⁶Peak energy E_{peak} in units of keV

⁷The excess absorption column density Δ_{NH} above the galactic value (see Grupe et al. 2007) is given in units of 10^{20} cm^{-2}

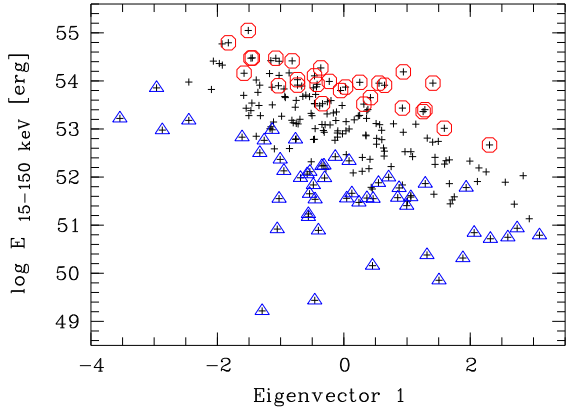


Fig. 25.— Eigenvector 1 from a PCA on long GRBs using T_{90} , Fluence, and Γ as input properties vs. isotropic energy E_{iso} in the 15-150 keV band. Bursts with redshifts $z > 3.5$ are marked as red circles and bursts with a redshift $z < 1.0$ are marked as blue triangles.

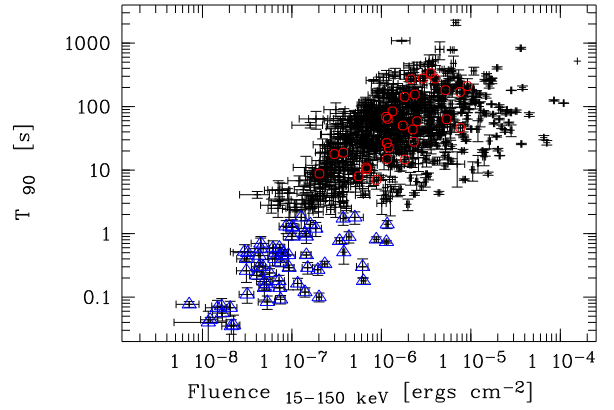


Fig. 28.— Fluence in the 15-150 keV *Swift* BAT band and T_{90}

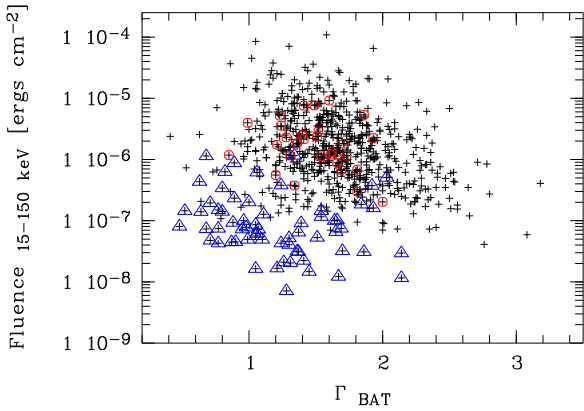


Fig. 26.— BAT photon index Γ_{BAT} vs. observed fluence in the 15-150 keV band. Short bursts are displayed as blue triangles.

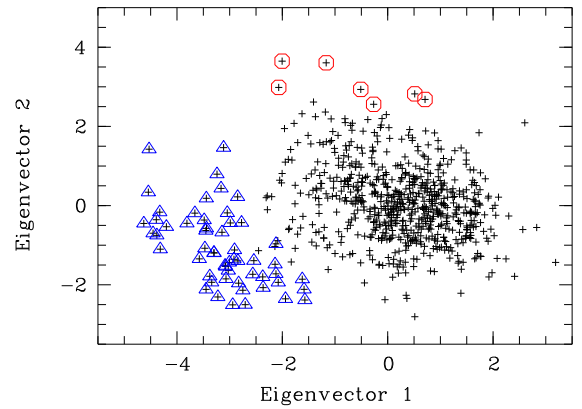


Fig. 30.— Eigenvector 1 vs. Eigenvector 2 plot of the GRBs of the cluster analysis using $\log T_{90}$, Γ , and \log 15-150 keV fluence. The different groups are marked as defined in Figure 29.

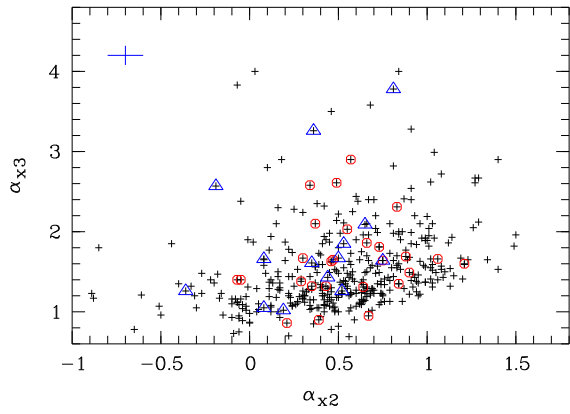


Fig. 36.— Correlation between decay slopes during the plateau phase α_{x2} and the ‘normal’ decay phase α_{x3} . The blue cross in the upper left corner displays the median uncertainty of each property.

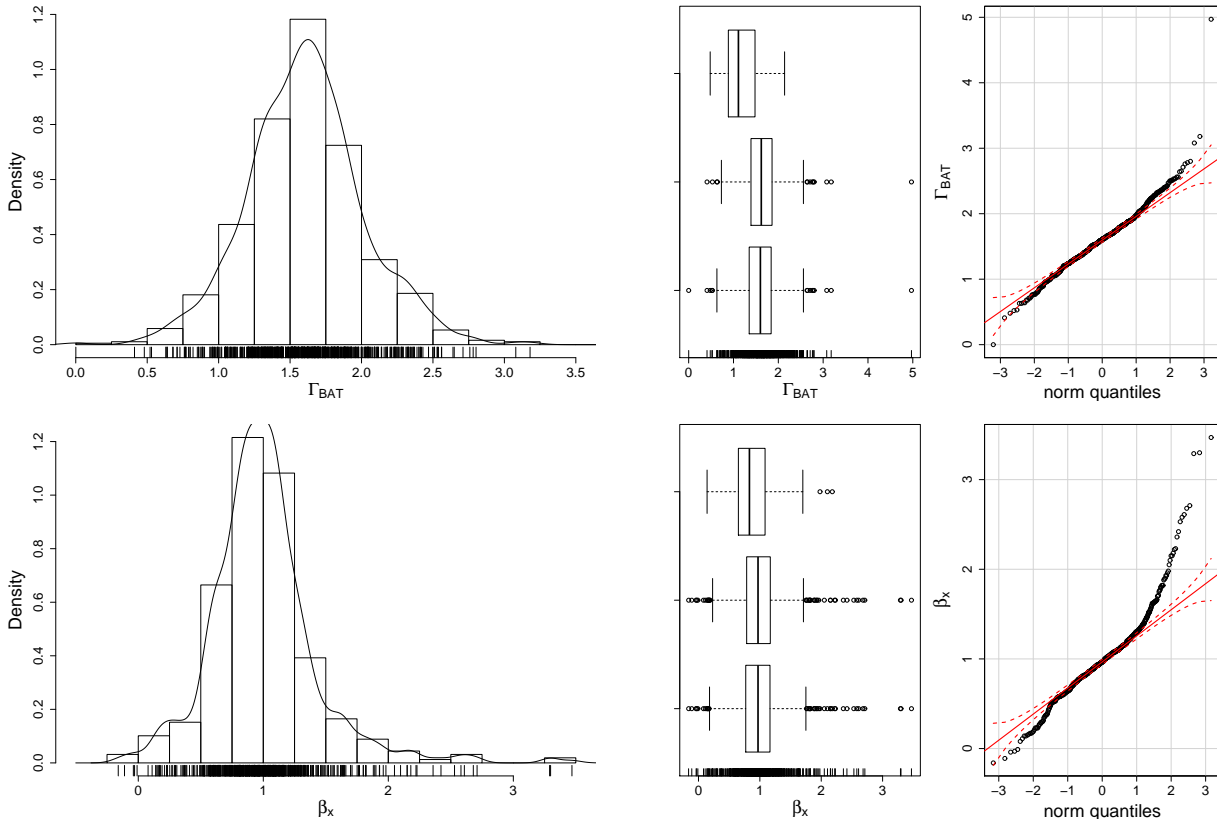


Fig. 31.— Distributions of the 15-150 keV BAT photon index and the 0.3-10 keV XRT energy spectral slope β_X , shown in the upper and lower panels, respectively. As in Figure 2, the histogram, box plot, and q-q plot are shown. In the box plots, short bursts are displayed on top, long bursts in the middle and all bursts on the bottom.

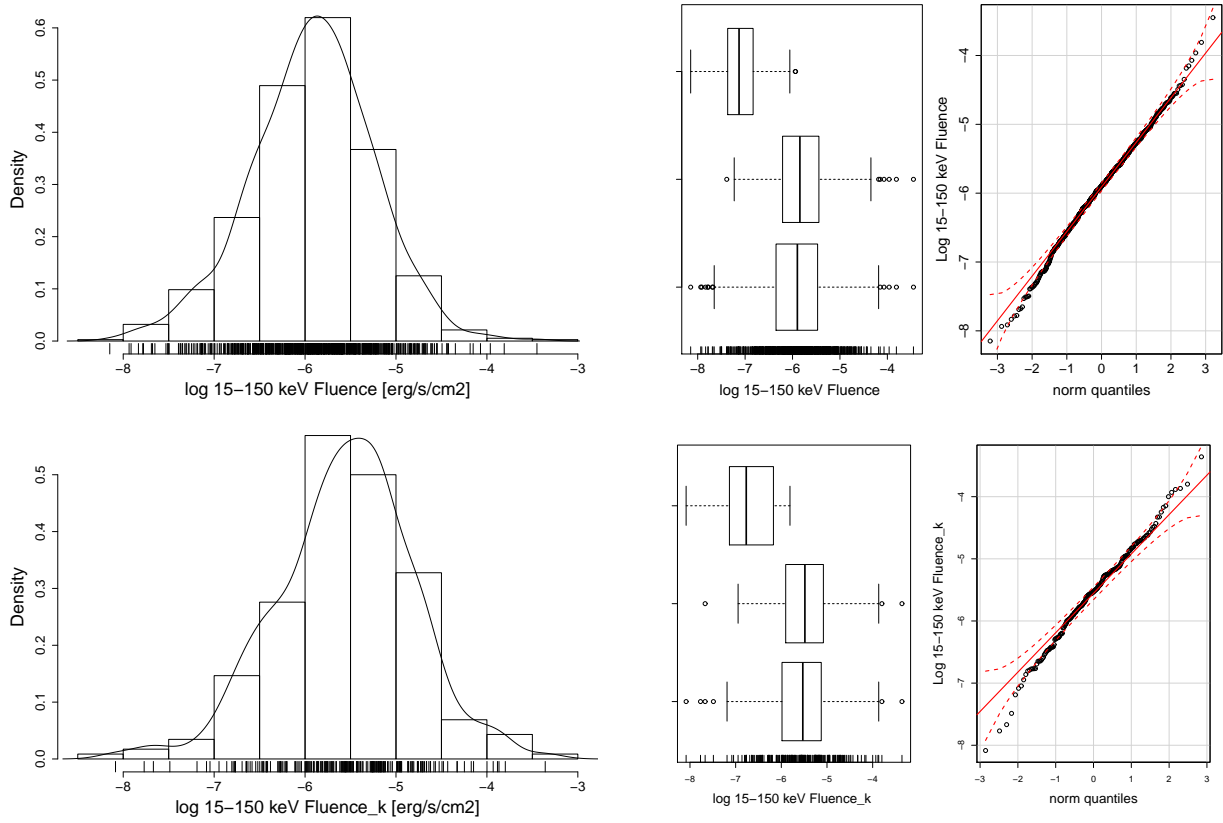


Fig. 32.— Distribution of the observed and k-corrected 15-150 keV fluence in the BAT band in units of erg cm^{-2} (upper and lower panel, respectively). As in Figure 2, the histogram, box plot, and q-q plot are shown. In the box plots, short bursts are displayed on top, long bursts in the middle and all bursts on the bottom.

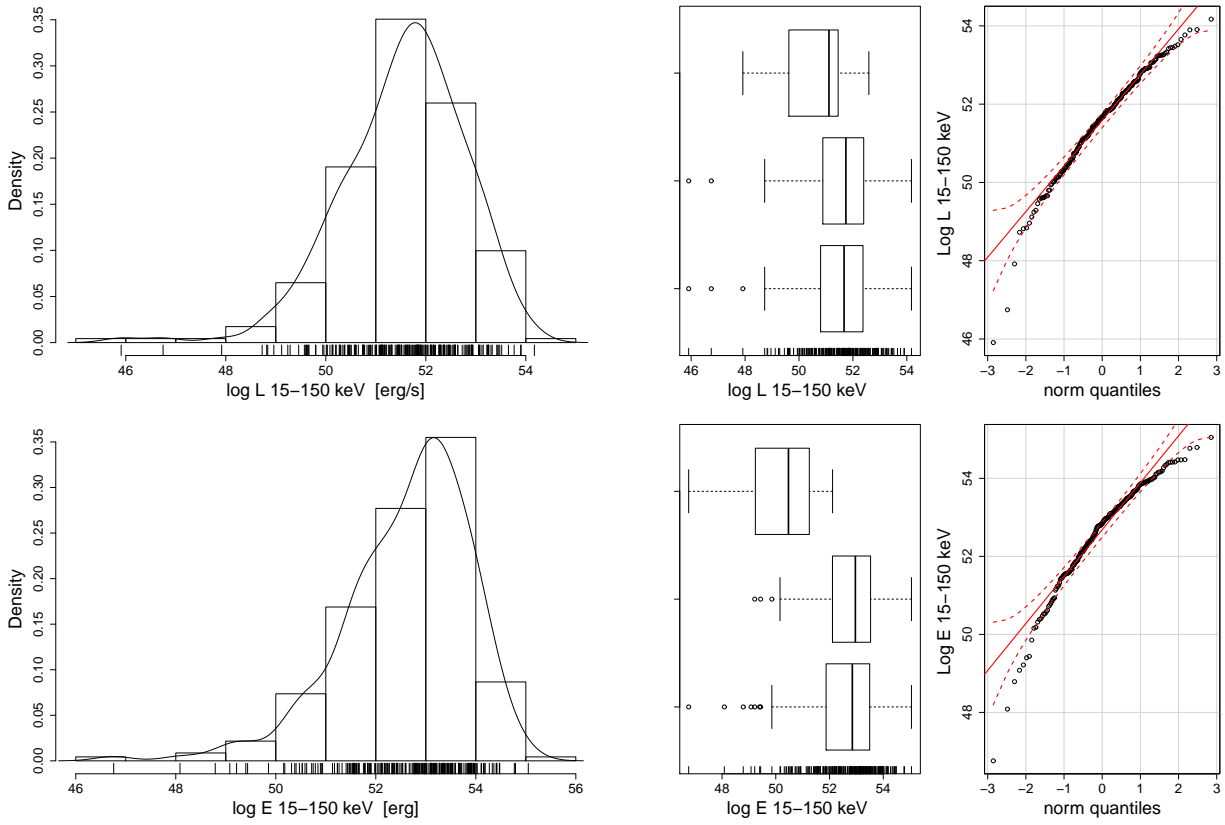


Fig. 33.— Distribution of the rest-frame 15-150 keV luminosity and isotropic energy E_{iso} of *Swift*-detected GRBs with spectroscopic redshifts (upper and lower panel, respectively). As in Figure 2, the histogram, box plot, and q-q plot are shown. In the box plots, short bursts are displayed on top, long bursts in the middle and all bursts on the bottom.

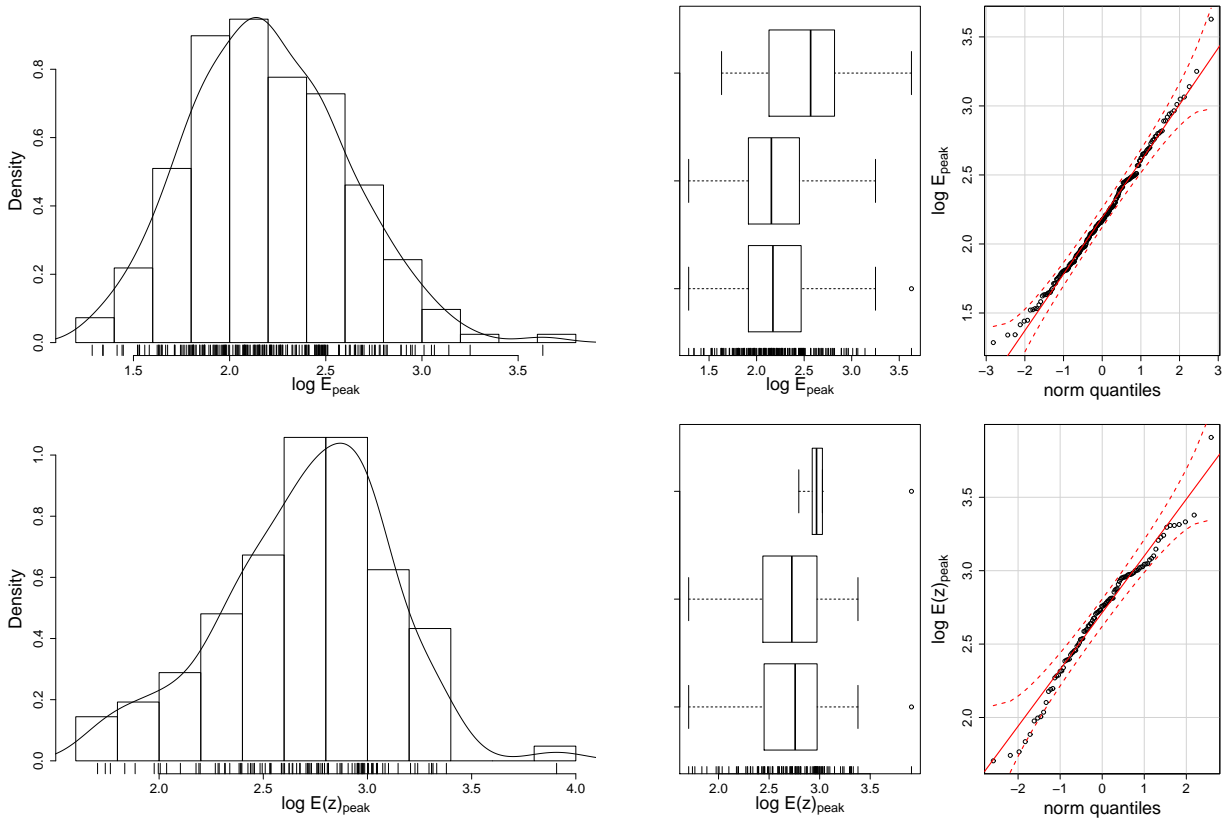


Fig. 34.— Distributions of the observed and rest-frame Peak energy $E_{\text{peak},z}$ of *Swift*-detected GRBs with spectroscopic redshifts (upper and lower panels, respectively). As in Figure 2, the histogram, box plot, and q-q plot are shown. In the box plots, short bursts are displayed on top, long bursts in the middle and all bursts on the bottom.

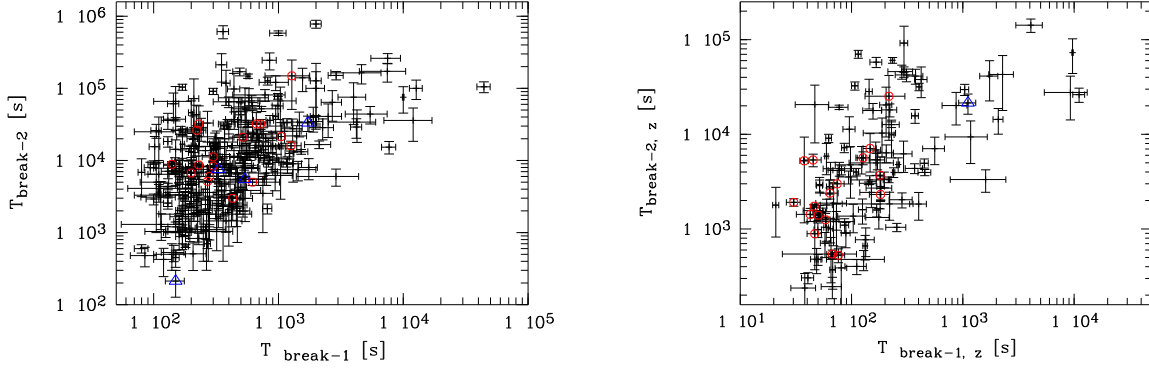


Fig. 35.— Correlation between the between the break times before and after the plateau phase $T_{\text{break}1}$ and $T_{\text{break}2}$ in the observed and rest-frame (left and right panel, respectively)..

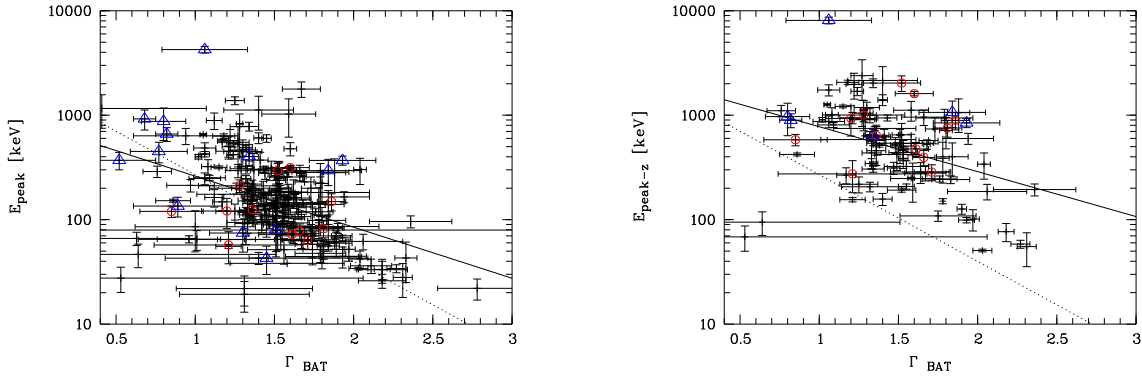


Fig. 37.— Correlation between the BAT 15-150 keV Γ and the peak energy E_{peak} in the observed and rest-frame (left and right panel, respectively). The dashed lines display the relation found by Sakamoto et al. (2009) and the solid line displays the relations found by us (see Appendix D)

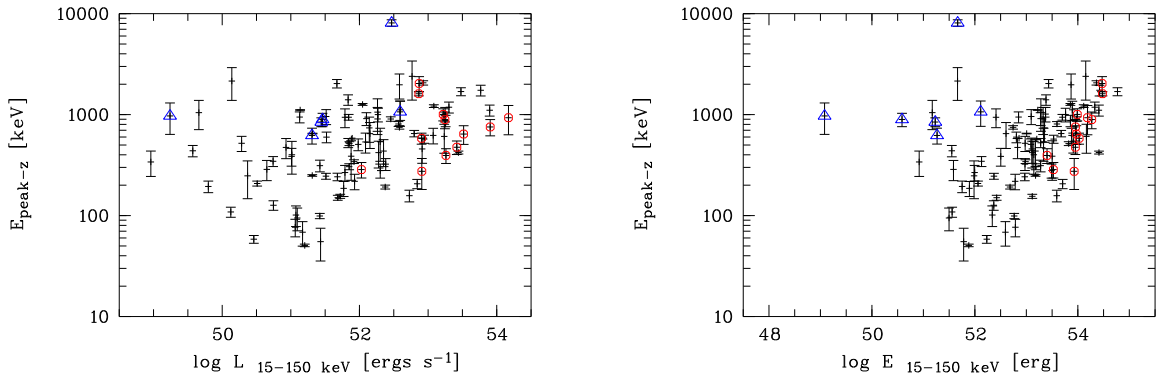


Fig. 38.— Correlation between the peak energy in the rest-frame $E_{\text{peak,z}}$ and the k-corrected luminosity in the 15-150 keV BAT band.

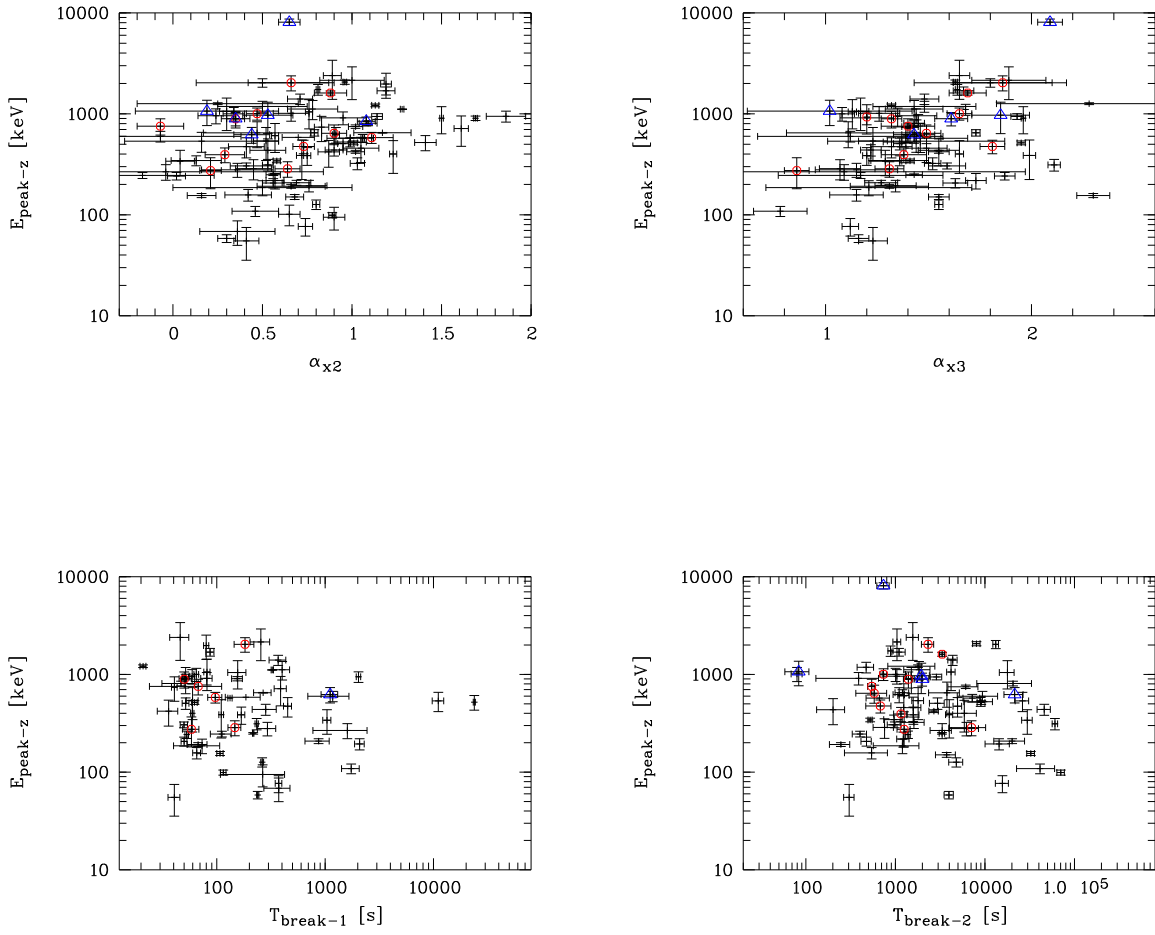


Fig. 39.— Correlation between the rest frame peak energy $E_{\text{peak},z}$ and the decay slope during and after the X-ray afterglow plateau phase α_{X2} and α_{X3} , and the rest-frame break times at the beginning and end of the plateau phase $T_{\text{break}1,z}$ and $T_{\text{break}2,z}$.

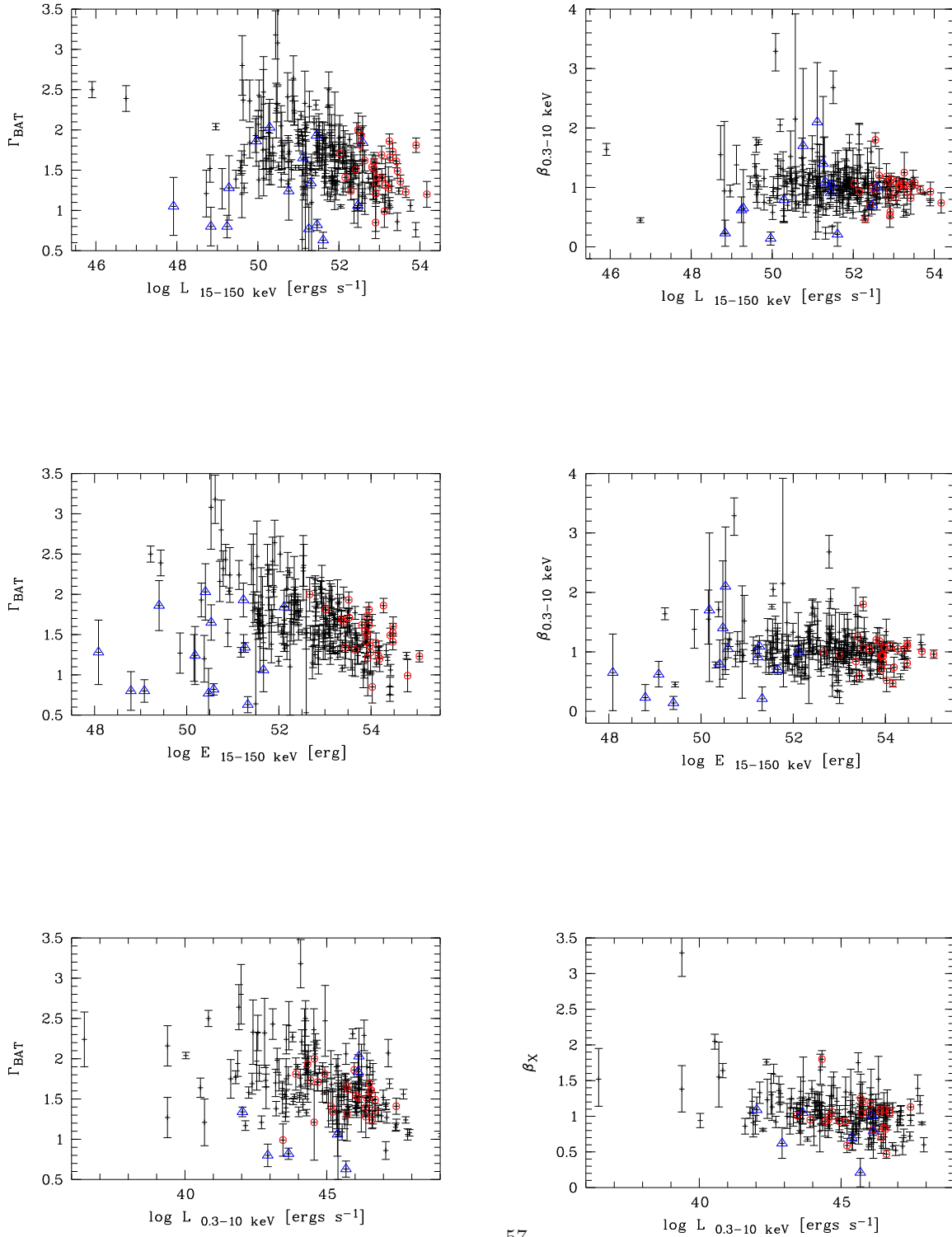


Fig. 40.— Relations of the k-corrected BAT luminosity and isotropic energy, and the luminosity in the 0.3-10 keV band with the BAT photon index Γ and the X-ray spectral slope β_X (left and right panel, respectively). Short bursts in these plots are marked as triangles.

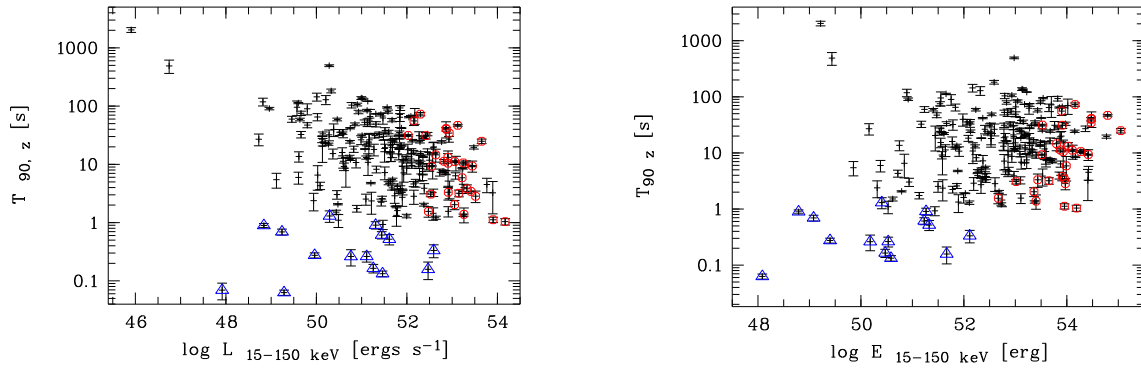


Fig. 41.— Anti-correlation between the 15-150 keV luminosity and the rest-frame T_{90} Short bursts in these plots are marked as triangles.

A. GRB Catalogue

Here we present the catalogue of our sample of 754 onboard *Swift*-BAT-detected GRBs. The ASCII file of the catalogue is available as a machine readable file on the Astrophysical Journal Supplement website linked to this paper. The explanation of the ASCII file is summarized in Table 9. The ASCII catalogue is prepared so it can be read directly into MIDAS. In order to read it into other data manipulations programs, the "*" has to be substituted with the appropriate symbol, like 'NA' in R for example. A more detailed explanation of all parameters used in this paper is listed in Appendix B.

B. Explanation of parameters

In this section we explain the parameters used in this paper and how they were derived. For this purpose we follow the order as listed in the GRB catalogue, Table 9.

- Redshift z : The redshifts prior 2012 were taken primarily from the GRB redshift catalogues by Fynbo et al. (2009); Jakobsson et al. (2012) and Krühler et al. (2012). All other redshift measurements were taken from GCN circulars.
- T_{90} : This time in which 90% of the energy is released in the prompt emission. The T_{90} used in this paper is the time measured in the observed 15-150 keV band in the *Swift* BAT.
- $T_{90,z}$: rest frame $T_{90,z} = T_{90}/(1+z)$
- *Fluence*: This is the fluence in the observed 15-150 keV BAT band.
- *Fluence_k*: k-corrected fluence with $Fluence_k = Fluence_{obs} \times (1+z)^{2-\Gamma}$.
- Γ : Photon index of the hard X-ray spectrum in the observed 15-150 keV band.
- E_{peak} : Peak energy of the hard energy spectrum derived from a Band function Band et al. (1993). We took the E_{peak} from GCN circulars. Before the launch of *Fermi* E_{peak} was primarily measured by Konus-Wind. After the *Fermi* launch we primarily relied on *Fermi* GBM measurements.
- $E_{peak,z}$: rest frame $E_{peak,z} = E_{peak} \times (1+z)$.
- $E_{15-150keV}$: k-corrected energy in the 15-150 keV BAT band assuming an isotropic energy release.
- $L_{15-150keV}$: k-corrected luminosity in the 15-150 keV BAT band assuming an isotropic energy release, with $L_{15-150keV} = E_{15-150keV}/T_{90,z}$
- $N_{H,gal}$: Galactic absorption column density derived from the HI maps by Kalberla et al. (2005). Throughout the paper the Galactic N_H is given in units of 10^{20} cm^{-2} .
- $N_{H,fit}$: Free-fit absorption column density. This was derived when the 0.3-10 keV X-ray spectrum can not be fit with just the Galactic value.
- Δ_{NH} : Excess absorption density as explained in Grupe et al. (2007) with $\Delta_{NH} = N_{H,fit} - N_{H,gal}$
- $N_{H,z}$: Absorption column density at the redshift of the burst. These column densities were derived by a power law fit to the 0.3-10 keV X-ray spectrum plus an absorption parameter fixed to the Galactic value.
- β_X : X-ray energy spectral index in the observed 0.3-10 keV band with $\nu F_\nu \propto \nu^{-\beta}$
- T_{break1} : Observed break time in the X-ray afterglow light curve before the plateau phase.

TABLE 9
GRB CATALOGUE ASCII FILE

Bytes	Format	Units	Label	Explanations
1 - 3	I3	—	Num	Running index number
5 - 11	A7	—	GRB	GRB Name
14 - 19	I6	—	Trigger#	BAT trigger number
22 - 28	F6.4	—	z	Redshift of the GRB
30 - 34	F8.3	s	T_{90}	observed BAT 15 - 150 keV T_{90}
36 - 41	F7.3	s	T_{90} err	T_{90} uncertainty
43 - 49	E7.2	erg cm ⁻²	Fluence	Fluence in the 15-150 keV BAT band
51 - 57	E7.2	erg cm ⁻²	Fluence err.	Uncertainty in the 15-150 keV BAT fluence
59 - 62	F4.2	—	Γ	BAT 15 - 150 keV photon index Γ
64 - 67	F4.2	—	Γ_{err}	Uncertainty of the BAT 15 - 150 keV photon index Γ
69 - 73	F7.2	keV	E_{peak}	Peak beak energy in keV at high energies
75 - 79	F7.2	keV	$E_{peak, err}$	Uncertainty in E_{peak}
81 - 88	F7.4	—	$\log E_{15-150keV}$	k-corrected energy in the 15-150 keV BAT band ¹ given in units of erg
90 - 96	F7.4	—	$\log L_{15-150keV}$	k-corrected luminosity in the 15-150 keV BAT band ¹ given in units of erg s ⁻¹ .
98 - 102	F6.2	10 ²⁰ cm ⁻²	$N_{H,gal}$	Galactic absorption column density (Kalberla et al. 2005)
104 - 109	F6.2	10 ²⁰ cm ⁻²	$N_{H,fit}$	free fit absorption column density ²
111 - 115	F6.2	10 ²⁰ cm ⁻²	$N_{H, err, -}$	negative uncertainty in the free fit N_H
117 - 122	F6.2	10 ²⁰ cm ⁻²	$N_{H, err, +}$	positive uncertainty in the free fit N_H
124 - 128	F7.3	10 ²² cm ⁻²	$N_{H,z}$	absorption column density at the redshift of the burst
130 - 134	F7.3	10 ²² cm ⁻²	$N_{H,z, err, -}$	negative uncertainty in absorption column density at the redshift of the burst.
136 - 140	F7.3	10 ²² cm ⁻²	$N_{H,z, err, +}$	positive uncertainty in absorption column density at the redshift of the burst.
142 - 146	F4.2	—	β_X	0.3-10 keV energy spectral index
148 - 152	F5.2	—	$\beta_{x, err, -}$	negative uncertainty in β_X
154 - 158	F5.2	—	$\beta_{x, err, +}$	positive uncertainty in β_X
160 - 164	I5	s	T_{break1}	X-ray light curve break time before the plateau phase
166 - 171	I5	s	$T_{break1, err}$	Uncertainty in T_{break1}
173 - 178	I6	s	T_{break2}	X-ray light curve break time after the plateau phase
180 - 185	I6	s	$T_{break2, err}$	Uncertainty in T_{break2}
187 - 191	F5.2	—	α_{X2}	X-ray light curve decay slope during the plateau phase
193 - 196	F4.2	—	$\alpha_{X2, err}$	Uncertainty in α_{X2}
198 - 201	F4.2	—	α_{X3}	X-ray light curve decay slope during the plateau phase
203 - 206	F4.2	—	$\alpha_{X3, err}$	Uncertainty in α_{X3}

¹The k-corrected energy and luminosity were based on the k-corrected fluence following the standard k-correction by Oke & Sandage (1968): $Fluence_k = Fluence_{obs} \times 1 + z^{2-\Gamma}$.

²The excess absorption above the Galactic value is then given by $\Delta_{NH} = N_{H,fit} - N_{H,gal}$.

- T_{break2} : Observed break time in the X-ray afterglow light curve after the plateau phase.
- $T_{\text{break1,z}}$: Break time in the rest frame in the X-ray afterglow light curve before the plateau phase, with $T_{\text{break1,z}} = T_{\text{break1}}/(1+z)$.
- $T_{\text{break2,z}}$: Break time in the rest frame in the X-ray afterglow light curve after the plateau phase, with $T_{\text{break2,z}} = T_{\text{break2}}/(1+z)$.
- α_{X2} : Decay slope of the plateau phase of the X-ray afterglow light curve in the 0.3-10 keV band with $\nu F_\nu \propto \nu^{-\alpha_2}$
- α_{X3} : Decay slope of the normal decay phase of the X-ray afterglow light curve in the 0.3-10 keV band with $\nu F_\nu \propto \nu^{-\alpha_3}$
- $Fluence_{0.3-10\text{keV}}$: Fluence in the observed 0.3-10 keV band during the plateau phase. This fluence was determined by integrating over the afterglow 0.3-10 keV flux light curve starting at the beginning of the plateau phase T_{break1} to the end of the plateau phase T_{break2} .

C. Additional Distributions

In this section we show additional distributions of GRB parameters observed by *Swift* that have not been shown in Section 3.1

As mentioned in Section 3.1, we applied the following statistical visualization tools to the data sets, which are common in data mining:

1. The left panel displays the histogram with the kernel density estimator (solid line) of the distribution. On the bottom of the plot the distribution of the real values of this property are shown.
2. The middle plot shows a box diagram for each property for short, long and all GRBs (top to bottom). The box displays the 1. (mean), 2. (median), and 3. quartile and the 'whiskers' which are defined as the minimum/maximum values of the distribution or the 1.5 times the interquartile range (so between the 1 and 3 quartile, so basically the 95% confidence level), whatever comes first. Values beyond the 'whiskers' are outliers and are displayed as circles.
3. The right panel displays the quartile-quartile plot (Q-Q-plot). This plot makes it easy to identify how well (or not) a distribution agrees with a Gaussian distribution which is shown as the solid line in these plots. The dashed lines mark the region of 95% confidence.

More information about these tools can be found in Feigelson & Babu (e.g. 2012); Torgo (e.g. 2011); Crawley (e.g. 2007).

Figure 31 displays the distributions of the observed 15-150 keV photon index in the BAT and the 0.3-10 keV X-ray energy spectral slope β_X . The distributions of Γ is close to a Gaussian distribution as shown in the Q-Q plot, with extended tails towards steep spectral slopes. In the distribution plot of the BAT photon index Γ , GRB 060202B (Aharonian et al. 2009) is off this plot with its $\Gamma = 4.97 \pm 0.49$. The box plot of the Γ distribution makes it apparent that short GRBs tend to have flatter hard X-ray spectra compared with long GRBs, as expected. Short GRBs have a median photon spectral index in the 15-150 keV range of $\Gamma=0.94$ while long GRBs have median of $\Gamma=1.56$. Note that although T_{90} and 15-150 keV fluence measurements exist for all the bursts, three early bursts (041219A, B, and C) did not have any spectral data available. In addition, GRB 120401 came into the BAT Field of view during a slew, therefore T_{90} and the fluence could not be measured (Palmer et al. 2012). In the 0.3-10 keV X-ray band, however, the spectral slopes of the X-ray afterglows of short and long GRBs are similar with median values of $\beta_X=0.82$ and 0.99 for short and long GRBs, respectively. As noticed by O'Brien et al. (2006) from a sample of 40 early *Swift* bursts,

the spectral slope of the afterglow data appears to be softer compared with the 15-150 keV slope during the prompt emission.

Figure 32 displays the distributions of the observed and k-corrected 15-150 keV fluence and the objects with the lowest fluence are short duration As we have discussed in Section 3.2, this is also the result of a selection effect: we can not detect long bursts with low fluence because their signal will be dominated by detector background. Bursts with low fluence therefore need to emit their energy in a short amount of time. Similar to these distributions is the distribution of the rest-frame 15-150 keV k-corrected luminosity and the isotropic energy shown in Figure 33.

The distributions of the peak energies E_{peak} in the observed and rest-frame are shown in Figure 34. As expected from the $E_{\text{peak}} - \Gamma$ anti-correlation found by Sakamoto et al. (2009), short GRBs which have flatter hard X-ray spectra than long-duration GRBs tend to have very high peak energies. As a matter of fact the burst with the highest $E_{\text{peak,z}}$ in our sample is the short GRB 090510, which has also been detected in the *Fermi* LAT (e.g., Abdo et al. 2009; De Pasquale et al. 2010). Note, however, that the number of short bursts with redshifts and E_{peak} measurements is only 6.

D. Additional Correlation analysis

In this Appendix we describe those correlations which have not been discussed in Section 3.3. We list also Kendall's and Pearson's correlation analysis to the data in addition to the Spearman rank order analysis discussed in Section 3.3. The number of correlation parameter pairs are the same as listed for the Spearman rank order correlations listed in Table 2 for the entire sample and Table 3 for the sample with GRBs with spectroscopic redshift measurements. Note the the number of parameter pairs for each correlation are listed in these tables. In the tables below, the Kendall's τ and the probability are listed above the diagonal and the Pearson correlation coefficient and probability are listed below. Table 10 lists the Kendall τ value and the Pearson correlation coefficients for all GRBs and Table 11 for those GRBs with spectroscopic redshift measurements.

Somewhat expected are correlations among afterglow parameters. As listed in Table 2 we find clear correlations between the break times before and after the plateau phase ($P < 10^{-8}$), and between the decay slopes during the plateau and the normal afterglow decay phase α_{X2} and α_{X3} ($P < 10^{-8}$). These two relations are displayed in Figures 35 and 36, respectively. The $T_{\text{break1}} - T_{\text{break,2}}$ relation is shown for the observed as well as for the rest-frame times. For the observed break times we found $r_s=0.517$ and $T_s=10.020$ (277 GRBs), and $r_s=0.620$, $T_s = 8.463$ (117 GRBs) for the observed and rest-frame times, respectively. In both cases the probability of a random result is $P < 10^{-8}$. Significant correlations exist between the decay slope during the plateau phase α_{X2} and the observed break time after the plateau phase $T_{\text{break,2}}$ with $r_s = +0.254$, $T_s = +5.320$ and $P=1.75 \times 10^{-7}$ (414 GRBs), and the decay slope of the 'normal' decay slope α_{X3} and the observed break time before the plateau phase with $r_s = +0.231$, $T_s = +4.825$ and $P=2.0 \times 10^{-6}$ (414 GRBs). Note that these correlations disappear in the rest-frame (Table 3).

As shown by Sakamoto et al. (2009) there is a clear anti-correlation between the photon index in the BAT spectrum and the peak energy in the spectrum E_{peak} by a relation $\log E_{\text{peak}} = 3.258 - 0.829 \times \Gamma$. Especially after the launch of *Fermi* with its all-sky monitor GBM, the number of GRBs with E_{peak} measurements has significantly increased. While the pre-*Fermi* sample in Sakamoto et al. (2009) contained 55 bursts with E_{peak} measurements, the sample in our paper has measurements of 201 bursts with E_{peak} measurements (including those presented in Sakamoto et al. (2009)) for which 188 are long GRBs. This relation is displayed in the left panel of Figure 37. Of these bursts, 103 had spectroscopic redshift measurements. As for the long GRBs we obtained a regression fit and found the following relations between the observed and rest-frame E_{peak} with Γ , respectively: $\log E_{\text{peak}} = (2.91 \pm 0.12) - (0.49 \pm 0.08) \times \Gamma$ and $\log E_{\text{peak,z}} = (3.32 \pm 0.16) - (0.43 \pm 0.11) \times \Gamma$. The relation of Γ with $E_{\text{peak,z}}$ in the rest-frame of the GRB is shown in the right panel of Figure 37. In both cases there is a clear anti-correlation between the two properties with $r_s = -0.462$, $T_s = -7.455$, $P < 10^{-8}$, and -0.416 , -4.625 , 1.10×10^{-5} for the observed and rest-frame E_{peak} respectively (206 and 104

TABLE 10

KENDALL'S τ AND PEARSON CORRELATION COEFFICIENTS AND PROBABILITIES OF FOR THE OBSERVED PARAMETERS OF ALL *Swift*-DETECTED GRBs¹ .

	Γ_{BAT}	β_{X}	$\alpha_{\text{X}2}$	$\alpha_{\text{X}3}$	T_{90}	$T_{\text{break}1}$	$T_{\text{break}2}$	15-150 keV fluence
Γ_{BAT}	—	$0.123, 4.76 \times 10^{-6}$	$-0.176, < 10^{-8}$	$-0.215, < 10^{-8}$	$+0.054, 0.0271$	$+0.048, 0.1676$	$+0.083, 0.0117$	$-0.1025, 2.89 \times 10^{-5}$
β_{X}	$+0.254, < 10^{-8}$	—	$-0.103, 4.17 \times 10^{-4}$	$-0.116, 1.88 \times 10^{-4}$	$+0.021, 0.4317$	$-0.049, 0.1504$	$+0.1106, 7.95 \times 10^{-4}$	$+0.006, 0.817$
$\alpha_{\text{X}2}$	$-0.228, 8.31 \times 10^{-8}$	$-0.161, 1.70 \times 10^{-4}$	—	$+0.279, < 10^{-8}$	$+0.144, .6.49 \times 10^{-7}$	$-0.023, 0.5075$	$+0.1725, 1.79 \times 10^{-7}$	$+0.1831, < 10^{-8}$
$\alpha_{\text{X}3}$	$-0.229, 4.62 \times 10^{-7}$	$-0.128, 0.0052$	$+0.234, 1.48 \times 10^{-6}$	—	$+0.1841, < 10^{-8}$	$+0.086, 0.0339$	$+0.163, 8.46 \times 10^{-7}$	$+0.1547, 5.18 \times 10^{-7}$
T_{90}	$+0.162, 8.16 \times 10^{-6}$	$-0.005, 0.905$	$+0.212, 7.33 \times 10^{-7}$	$-0.045, 0.325$	—	$+0.223, < 10^{-8}$	$+0.348, < 10^{-8}$	$+0.481, < 10^{-8}$
$T_{\text{break}1}$	$+0.033, 0.5218$	$-0.059, 0.2451$	$+0.010, 0.852$	$+0.075, 0.2143$	$+0.296, < 10^{-8}$	—	$+0.360, < 10^{-8}$	$-0.042, 0.2169$
$T_{\text{break}2}$	$+0.088, 0.0744$	$+0.166, 6.91 \times 10^{-4}$	$+0.272, 272 \times 10^{-8}$	$+0.055, 0.2595$	$+0.526, < 10^{-8}$	$+0.531, < 10^{-8}$	—	$+0.126, 1.25 \times 10^{-3}$
15-150 keV fluence	$-0.1007, 0.0058$	$-0.055, 0.165$	$+0.261, < 10^{-8}$	$-0.019, 0.6741$	$+0.715, < 10^{-8}$	$-0.016, 0.7498$	$+0.235, 1.20 \times 10^{-6}$	—

¹Kendall's τ and Pearson correlation coefficients and probabilities are listed above and below the diagonal, respectively. The number of parameter pairs are given in Table 2.

TABLE 11

KENDALL'S τ AND PEARSON CORRELATION COEFFICIENTS AND PROBABILITIES OF GRBS WITH SPECTROSCOPIC REDSHIFTS^{1 1}

	Γ_{BAT}	β_{X}	$\alpha_{\text{X}2}$	$\alpha_{\text{X}3}$	$T_{90,z}$	$T_{\text{break}1,z}$	$T_{\text{break}2,z}$	$L_{15-150\text{keV}}$	E_{iso}
Γ_{BAT}	—	$0.140, 1.70 \times 10^{-3}$	$-0.186, 7.53 \times 10^{-5}$	$-0.189, 1.35 \times 10^{-4}$	$0.069, 0.117$	$0.072, 0.2054$	$0.107, 0.036$	$0.2675, < 10^{-8}$	$-0.266, < 10^{-8}$
β_{X}	$+0.228, 8.82 \times 10^{-4}$	—	$-0.122, 0.0093$	$-10.1809, 2.58 \times 10^{-4}$	$0.050, 0.257$	$0.074, 0.1915$	$0.182, 3.88 \times 10^{-4}$	$-0.090, 0.0443,$	$-0.060, 0.0604$
$\alpha_{\text{X}2}$	$-0.248, 2.99 \times 10^{-5}$	$-0.224, 0.0012$	—	$0.2189, 2.07 \times 10^{-5}$	$0.1235, 0.0084$	$-0.0456, 0.4311$	$0.0633, 0.2149,$	$0.0887, 0.0592$	$0.1627, 5.31 \times 10^{-4}$
$\alpha_{\text{X}3}$	$-0.157, 0.1556$	$-0.244, 7.34 \times 10^{-4}$	$+0.202, 0.0074$	—	$0.1272, 0.0098$	$-0.075, 0.2361$	$0.043, 0.4033$	$-0.1100, 0.0256$	$0.2057, 2.97 \times 10^{-5}$
$T_{90,z}$	$+0.143, 0.0298$	$+0.029, 0.6643$	$+0.198, 0.0041$	$+0.086, 0.2392$	—	$0.251, 8.46 \times 10^{-6}$	$0.305, < 10^{-8}$	$-0.206, 3.09 \times 10^{-6}$	$0.130, 3.30 \times 10^{-3}$
$T_{\text{break}1,z}$	$+0.050, 0.5524$	$+0.079, 0.3449$	$-0.023, 0.7824$	$-0.101, 0.2836$	$+0.362, 8.01 \times 10^{-6}$	—	$0.432, < 10^{-8}$	$-0.409, < 10^{-8}$	$-0.3317, < 10^{-8}$
$T_{\text{break}2,z}$	$+0.160, 0.03398$	$+0.335, 5.76 \times 10^{-6}$	$+0.103, 0.175$	$+0.070, 0.3535$	$+0.450, < 10^{-8}$	$+0.613, < 10^{-8}$	—	$-0.285, 2.05 \times 10^{-8}$	$-0.131, 0.0100$
$L_{15-150\text{keV}}$	$-0.343, 9.01 \times 10^{-8}$	$-0.129, 0.0512$	$+0.110, 0.1154$	$+0.058, 0.4289$	$-0.238, 2.65 \times 10^{-4}$	$-0.574, < 10^{-8}$	$-0.439, < 10^{-8}$	—	$0.664, < 10^{-8}$
E_{iso}	$-0.256, 8.34 \times 10^{-5}$	$-0.113, 0.0886$	$+0.222, 1.3 \times 10^{-3}$	$+0.110, 0.133$	$+0.323, 5.33 \times 10^{-7}$	$-0.415, 2.45 \times 10^{-7}$	$-0.207, 0.0060$	$+0.843, < 10^{-8}$	—
$E_{\text{peak},z}$	$-0.397, 3.06 \times 10^{-5}$	$-0.131, 0.1889$	$+0.273, 0.0065$	$-0.006, 0.959$	$-0.103, 0.2977$	$-0.122, 0.3312$	$-0.196, 0.077$	$+0.384, 6.36 \times 10^{-5}$	$+0.334, 4.81 \times 10^{-4}$

¹Kendall's τ and Pearson correlation coefficients and probabilities are listed above and below the diagonal, respectively. The number of parameter pairs are given in Table 3.

GRBs respectively). The solid line in these plots display the relations between E_{peak} and Γ that we found for our *Swift* GRB sample and the dotted line shows the relation found by Sakamoto et al. (2009).

The best-known relationships of the peak energy E_{peak} , are those between the isotropically radiated energy E_{iso} and the collimation-corrected energy E_{γ} , the Amati and Ghirlanda relations, respectively (Amati et al. 2002; Ghirlanda et al. 2004). Similar to these relations is the $E_{\text{peak}} - L_{\text{peak}}$ relation found by Yonetoku et al. (2004) from BATSE detected bursts. Previously Schaefer (2007) found this relation for pre-*Swift* bursts, however, it has also been found in *Swift*-detected bursts as reported by (Nava et al. 2012) who used 58 bursts with photon peak fluxes in the 15-150 BAT energy window with $P > 2.6$ photons $\text{cm}^{-2} \text{s}^{-1}$. We found a similar correlation between the rest-frame $E_{\text{peak},z}$ and the prompt emission luminosity and isotropic energy E_{iso} as displayed in Figure 38. These correlations (103 long GRBs) are quite tight with $r_s=0.426$, $T_s=4.735$ and $P = 7.0 \times 10^{-6}$ for the luminosity and $r_s=0.459$, $T_s=5.187$ with $P = 1.07 \times 10^{-6}$ for E_{iso} .

The question is: does $E_{\text{peak},z}$ also correlate with other burst properties? What we found was that among the long bursts there is a correlation between $E_{\text{peak},z}$ and the decay slope during the plateau phase α_{X2} , with $r_s=0.344$, $T_s=3.470$, and $P = 7.94 \times 10^{-4}$ (92 GRBs), as displayed in Figure 39. This again demonstrates a clear connection between prompt and afterglow emission properties: bursts with steeper decay slopes during the plateau phase show peak energies in the rest-frame $E_{\text{peak},z}$ at high energies than bursts with flatter decay slopes. All other properties, such as β_X , or α_{X3} do not show any significant correlation with $E_{\text{peak},z}$.

The relations of the K-corrected 15-150 keV luminosity and the spectral slope in the BAT band Γ_{BAT} and the X-ray spectral slope of the afterglow emission are displayed in Figure 40. While there is no correlation with β_X (right panel in Figure 40), there is a strong correlation with the BAT photon index Γ_{BAT} . Here we found an anti-correlation for the long bursts with $r_s = -0.457$, $T_s = -7.519$ and a probability $P < 10^{-8}$ (216 GRBs). In other words, bursts with steep BAT photon indices tend to be less luminous than bursts with flatter Γ_{BAT} . Note that short duration GRBs do not follow this anti-correlation. Table 3 lists the correlations of all bursts, including short bursts. The anti-correlation between Γ and $L_{15-150\text{keV}}$ becomes slightly weaker for all GRBs. Although this anti-correlation is a relation between a redshift dependent parameter (Γ) and a redshift independent parameter ($L_{15-150\text{keV}}$), GRBs still can not be used as standard candles. Not only is the scatter in the relation quite large, but $L_{15-150\text{keV}}$ is not independent of Γ because we used Γ as an input parameter in the k-correction. Now lets see how Γ and β_X depend on the 15-150 keV energy release. These relations are displayed in the lower panels in Figure 40 where Γ anti-correlates strongly with the isotropic energy in the 15-150 keV band $E_{15-150\text{keV}}$ ($r_s=-0.492$, $T_s=-8.268$, $P < 10^{-8}$ for the 216 long GRBs. Again, as listed in Table 2 the relation becomes weaker for all GRBs. As for the 0.3-10 keV spectral slope β_X , this is only a weak trend with $r_s=-0.177$, $T_s = -2.634$, and $P = 0.0090$ for the long GRBs (215).

Figure 41 displays the relation between the rest-frame $T_{90,z}$ and the luminosity in the 15-150 keV band. For the whole GRB sample we found a Spearman rank order correlation coefficient of $r_s=-0.290$ and a Student's T-test of $T_s=-4.580$ with a probability of $P = 8.41 \times 10^{-6}$ (231 GRBs) However, if we only look at the long GRBs in the sample with spectroscopic redshifts (216 GRBs), this correlation becomes even stronger with $r_s=-0.420$, $T_s=-6.777$, and $P < 10^{-8}$. This relation suggests a strong anti-correlation with high luminosity bursts having shorter T_{90} . However, keep in mind that the luminosity and T_{90} are not independent parameters. The luminosity was calculated by $L = E/T_{90}$ so bursts with longer T_{90} will have lower luminosities if we assume that their isotropic energies are somewhat similar. Although the T_{90} - luminosity relation looks like a significant correlation it may not be a physical relation. If more energetic bursts have really shorter T_{90} then we should expect such a relation between the isotropic energy in the 15-150 keV band and T_{90} . This is, however, a weak correlation with $r_s=+0.197$ and $T_s=3.044$ with $P = 2.60 \times 10^{-3}$ of a random distribution. This relation, however, is driven by the short bursts. When applying this relation to only long bursts, the correlation disappears completely.

E. Redshift estimate based in BAT parameters

In Section 3.6 we showed that it may be possible to determine the 15-150 keV E_{iso} based on the observed *Swift*-BAT parameter. The relations from the PCA as described in Section 3.6 are shown in the the eigenvector 1 - E_{iso} diagram, Figure 25. In order to place a new GRB onto this digram we give the equations of the normalized BAT parameters T_{90} , Γ , and fluence below:

$$\log T_{90,\text{norm}} = (\log T_{90} - 1.636871)/0.557497 \quad (\text{E1})$$

$$\Gamma_{\text{norm}} = (\Gamma - 1.643410)/0.4071438 \quad (\text{E2})$$

$$\log \text{Fluence}_{\text{norm}} = (\log \text{Fluence} + 5.650423)/0.5962325 \quad (\text{E3})$$

Now we can calculate eigenvector 1 based on the PCA performed on the long GRBs with spectroscopic redshift measurements:

$$\text{eigenvector1} = -0.558370 * T_{90,\text{norm}} + 0.455017 * \Gamma_{\text{norm}} - 0.693674 * \text{Fluence}_{\text{norm}} \quad (\text{E4})$$

F. Separating Short and Long Duration GRBs

In this section we give the relations that will allow the reader to place a new GRB in the eigenvector 1 - eigenvector 2 diagram, Figure 30 as described in Section ???. We first list the equation for the normalized T_{90} , Γ , and fluence:

$$\log T_{90,\text{norm}} = (\log T_{90} - 1.43508)/0.798325 \quad (\text{F1})$$

$$\Gamma_{\text{norm}} = (\Gamma - 1.614035)/0.4201068 \quad (\text{F2})$$

$$\log \text{Fluence}_{\text{norm}} = (\log \text{Fluence} + 5.919272)/0.6762907 \quad (\text{F3})$$

Now we can calculate the eigenvectors:

$$\text{eigenvector1} = 0.714278 * T_{90,\text{norm}} + 0.06593 * \Gamma_{\text{norm}} + 0.696829 * \text{Fluence}_{\text{norm}} \quad (\text{F4})$$

$$\text{eigenvector2} = 0.120528 * T_{90,\text{norm}} + 0.969348 * \Gamma_{\text{norm}} - 0.214095 \text{Fluence}_{\text{norm}} \quad (\text{F5})$$